UNIVERSITÀ DEGLI STUDI DI PADOVA

FACOLTA DI SCIENZE MM. FF. NN.

DIPARTIMENTO DI FISICA

SCUOLA DI DOTTORATO DI RICERCA IN FISICA

XX CICLO

Performances of the Ion Electron Emission Microscope at SIRAD

Direttore della Scuola: Prof. Attilio Stella

Supervisore: Prof. Dario Bisello

Dottorando: Serena Mattiazzo

31 gennaio 2008

Introduction

When an energetic ion strikes a microelectronic device it induces current transients that may lead to a variety of undesirable Single Event Effects (SEE). An important part of the activity of the SIRAD heavy ion facility at the 15 MV Tandem accelerator of the INFN Laboratories of Legnaro (Italy) concerns SEE studies of microelectronic devices destined for radiation hostile environments.

An Ion Electron Emission Microscope (IEEM) is working at the SIRAD facility. In the IEEM technique, a broad ion beam irradiates a device under test (DUT) and the secondary electrons emitted by the target surface by each ion impact are collected and focused by a commercial electron emission microscope onto a fast electron detector. The spatial (x and y coordinates) and the temporal information of the ion impacts are then correlated to the SEE induced in the device under test and a SEE sensitivity map is obtained. An IEEM can achieve resolutions better than 1μm, comparable to the ones achieved by nuclear microprobes techniques where the DUT is systematically scanned with micrometric precision with a microfocused beam. For a heavy ion microbeam to work one must meet severe requirements in terms of beam monochromaticity and stability. The IEEM poses no such requests.

In this thesis we describe in detail the IEEM apparatus working at SIRAD facility and the performed experiments, but first we discuss the physical aspects involved in radiation hardness testing. The *first chapter* introduces the subject of radiation effects on electronic devices and will focus on the physical processes involved. The *second chapter* discusses Single Event Effects and describes the various types of effects that can be induced by a single particle strike. The *third chapter* is mainly dedicated to the description of the space environment, a radiation hostile environment of great technological and scientific importance, where electronic systems expected to operate without failure. *Chapter four* deals with experimental techniques and procedures for SEE studies and device

characterization; experimental limits and testing constraints requested by the most recent electronic technologies are pointed out. A description of nuclear microprobes techniques is also given. In *chapter five* a general description of the IEEM technique is given, while the *chapter six* is fully dedicated to the detailed description of the IEEM apparatus working at SIRAD and to the original opto-electronic solutions we adopted. *Chapter seven* opens with the presentation of the first imaging results in the axial configuration; we then discuss the use of standard ultra-thin targets and the lateral resolution and energy degradation introduced by them; we then discuss the ion induced secondary electron emission yields from the standard targets and conclude with a discussion on the expected and measured ion detection efficiency of the IEEM. *Chapter eight*, the final one, is dedicated to a Single Event Upset measurement using a Synchronous-DRAM. A detailed description is given of the developed setup and the analysis of experimental results, with a particular emphasis on the estimated spatial resolution. The *conclusions* follow and close this work.

Introduzione

Quando uno ione energetico colpisce un dispositivo microelettronico induce un transitorio in corrente che può indurre una varietà di indesiderati Single Event Effects (SEE). Una parte importante dell'attività svolta presso la facility di irraggiamento con ioni pesanti SIRAD, collocata all'acceleratore tandem da 15 MV dei Laboratori Nazionali di Legnaro, riguarda studi di SEE in dispositivi microelettronici destinati all'uso in ambienti ostili dal punto di vista delle radiazioni.

Presso la facility SIRAD è in funzione un Ion Electron Emission Microscope (IEEM). Nella tecnica IEEM, un fascio di ioni ampio irraggia un dispositivo e gli elettroni secondari emessi dalla superficie del bersaglio sono estratti e messi a fuoco su un rivelatore di elettroni da un microscopio elettronico commerciale. Le coordinate spaziali e temporali dell'impatto rivelato sono messe in relazione con il SEE indotto sul bersaglio, fino a ottenere una mappa micrometrica della sua sensibilità. Uno IEEM può raggiungere risoluzioni migliori di 1 μm, confrontabili con quelle raggiunte con tecniche "*nuclear microprobe"*, dove un fascio micro focalizzato è inviato con precisione micrometrica sulla superficie del DUT. Il funzionamento di un sistema a microbeam con ioni pesanti pone dei severi requisiti sulla monocromaticità e sulla stabilità del fascio. Lo IEEM, invece, non ha queste richieste.

In questa tesi descriveremo in dettaglio lo IEEM in funzione presso la facility di irraggiamento SIRAD e gli esperimenti con esso realizzati, iniziando con la discussione degli aspetti fisici alla base dello studio del danno da radiazione. Il *primo capitolo* introduce il tema degli effetti delle radiazioni sui dispositivi elettronici, soffermandosi sui processi fisici coinvolti. Il *secondo capitolo* discute i Single Event Effects e descrive i vari tipi di errori che possono essere indotti dal passaggio di una singola particella attraverso un dispositivo. Il *terzo capitolo* è principalmente dedicato alla descrizione dell'ambiente spaziale, un ambiente ostile di grande importanza tecnologica e scientifica,

dove i sistemi elettronici devono poter garantire il loro corretto funzionamento senza danni. Il *capitolo quattro* affronta le tecniche sperimentali adottate per lo studio di SEE e per la caratterizzazione dei dispositivi; verranno anche sottolineati i loro limiti attuali e le richieste imposte dai test sulle nuove tecnologie. In particolare verranno descritte le tecniche che fanno uso di microbeam. Il *quinto capitolo* dà una descrizione generale della tecnica IEEM, mentre il *sesto capitolo* è interamente dedicato alla descrizione dello IEEM installato a SIRAD e alle originali soluzioni opto-elettroniche adottate. Il *capitolo sette* si apre con le prime immagini ottenute con lo IEEM assiale; discuteremo poi l'uso di bersagli standard ultra sottili e il degrado in risoluzione e in energia dovuti alla loro scelta; discutiamo poi la resa in elettroni secondari per impatto ionico su tali bersagli e concluderemo con una discussione sull'efficienza di rivelazione di ioni dello IEEM, confrontando le stime teoriche con i risultati delle misure. L'*ottavo* e ultimo *capitolo* è dedicato a una misura di Single Event Upset su una SDRAM con lo IEEM. Verranno forniti una dettagliata descrizione del setup sviluppato e l'analisi dei dati sperimentali, con una particolare enfasi sulla stima delle risoluzione spaziale del microscopio. Seguiranno le *conclusioni*, a chiudere questa tesi.

1. Radiation effects on electronic devices

1.1 Physical processes

1.1.1 Introduction

The effect of ionizing particles on electronic components results essentially from the track (electron-hole pair column) they form in matter by a Coulombian interaction with electrons.

When a single, highly energetic particle (protons or heavy ions) strikes a sensitive volume of a microelectronic circuit, i.e. a reversed-biased junction, the built-in electrical field allows charge collection at the output node of the circuit. This sudden perturbation leads to functional anomalies (Single-Event Effects, *SEE*) in most kind of devices. But also a homogeneous accumulation of ionizing dose deposition over a long time (due to a high particle flux) is at the origin of degradation of the electrical performances of the device (Total Dose Effects, *TDE*).

There are two primary methods by which ionizing radiation releases charge in a semiconductor device: direct ionization by the incident particle itself and ionization by secondary particles created by nuclear reactions between the incident particle and the struck device. Both mechanism can lead to circuit malfunction.

1.1.2 Direct charge deposition

When an energetic charged particle passes through a semiconductor material, it frees electron-hole pairs along its path as it loses energy. When all of its energy is lost, the particle comes to rest in the semiconductor, having traveled a total path length referred to as the particle's range. A frequently used quantity is the linear energy transfer, *LET*, i.e. the energy loss per unit path length of a particle as it passes through a material. LET has

units of MeV·cm^2/mg: the energy loss per unit path length is normalized by the density of the target material, so that LET can be roughly quoted independent of the target. We can easily relate the LET of a particle to its charge deposition per unit path length, because for a given material it takes a certain quantity of energy to release an electron-hole pair. For example, in silicon approximately 3.6eV energy deposition is needed to release one electron-hole pair, and silicon has a density of 2325mg/cm^3 [1]. Using these values it is easy to show that an LET of 97 MeV·cm^2/mg corresponds to a charge deposition of 1 pC/μm. This conversion factor of about 100 between LET and charge deposition in silicon is handy to keep in mind. Another useful rule of thumb is that the maximum LET of an ion (in MeV-cm2/mg), i.e. the LET at to the Bragg peak, is approximately equal to its atomic number Z [2].

A curve of particular interest for understanding the interaction of a given particle with matter is the LET of the particle as a function of the depth it travels through the target material.

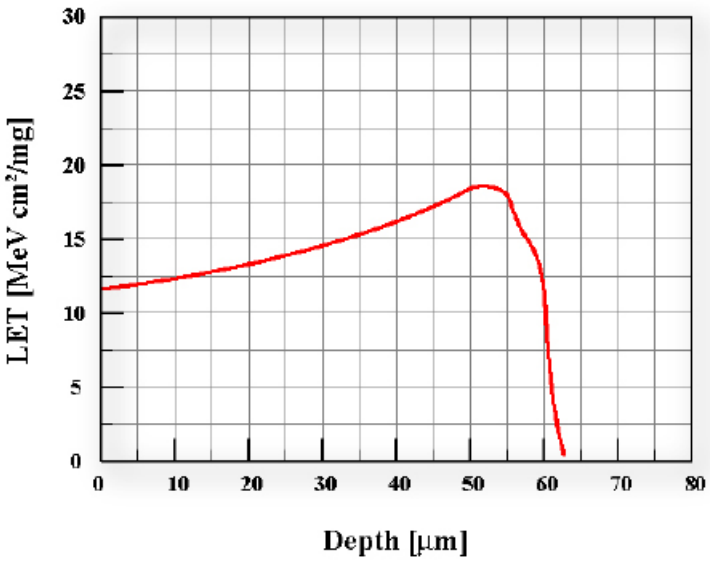

Fig. 1.1 LET vs depth curve for 210MeV chlorine ion in silicon

Figure 1.1 shows such a curve for a 210 MeV chlorine ion traveling through silicon. The peak in the charge deposition (referred to as Bragg peak) occurs as the particle nears its range and reaches, in general, an energy near 1 MeV/nucleon.

Whether or not the charge deposited through direct ionization is sufficient to cause an upset of course depends on the individual device and circuit that has been struck as well as the strike location and trajectory.

Direct ionization is the primary charge deposition mechanism for upsets caused by heavy ions (ions with atomic number $Z \geq 2$, i.e. He and above). Lighter particles, such as protons, do not usually produce enough charge by direct ionization to cause upset in memory circuits, but recent research (not experimentally confirmed to date) has suggested that single event effects due to direct ionization by protons may occur in new and more susceptible ICs [3], [4].

Single event effects resulting from proton direct ionization are capable of causing upsets in photodiodes used in optocoupler application, because they are by design very large and operate at very high data rate. Charge-coupled devices (CCDs) can also be sensitive to direct ionization by protons because their large collection depth [5].

1.1.3 Indirect charge deposition

Even though direct ionization by light particles usually does not produce a high enough charge density to cause upsets, protons and neutrons can both produce significant upset rates due to indirect mechanism.

As a high energy proton enters the semiconductor lattice, it may undergo an inelastic collision with a target nucleus. This may result in the emission of alpha (α) or gamma (γ) particles and the recoil of a daughter nucleus (e.g. Si emits α-particle and a recoiling Mg nucleus), or a spallation reaction, in which the target nucleus is broken into two fragments (e.g. Si breaks into C and O ions), each of which can recoil. Any of these reaction products can now deposit energy along their path by direct ionization and, as these particles are much heavier than the original proton or neutron, they can deposit higher charge densities as they travel and therefore may be capable of causing an SEU. This inelastic collision products typically have fairly low energies and do not travel far from the particle impact site. They also tend to be forwarded scattered in the diretion of

the original particle and this has consequences for the SEU sensitivity as a function of angle of incidence.

Recent experiments and simulations have demonstrated that elastic collisions may become important for very sensitive devices. In particular, low energy products (such as protons and neutons), generated within packages or shielding, may be an even more significant source of SEU in these sensitive devices [6].

1.2 Charge collection

1.2.1 Introduction

The basic properties of charge collection following a particle strike have been investigated using several theorethical and experimental methods.

Physics of charge collection have been studied through the use of two and three dimensional numerical simulations [7], [8] or through the measure of charge collection transient by ion microbeams and lasers. Ion microbeam and lasers have also been used to map integrated charge collection as a function of both time and position [9] in ICs.

1.2.2 Physics of charge transport

There are essentially three mechanism that act on the charge deposited by an energetic particle strike: 1) carriers can move by *drift* in response to applied or built-in fields in the device, 2) carriers can move by *diffusion* under the influence of carrier concentration gradients withn the device, or 3) carriers can be annihilated by *recombination* through direct or indirect processes. These three mechanism are the governing processes of chage transport in semiconductor under most opeting conditions, and they are not unique to the particle strike problem.

When an energetic particle hits a microelectronic device, the most sensitive regions are reversed biased p/n junctions. The high field present in a reversed-biased junction

depletion region can very efficiently collect the particle induced charge through drift processes, leading to a transient current at the junction contact.

When carriers are generated in the region of the device where an electric field is applied (such as a p/n junction), electrons and holes start drifting apart. According to Gunn's theorem, the drifting carriers induce a current on the electrode of the device. The induced current appears on all electodes simultaneously (and not when the carriers actually reach the electrodes) delayed only by the time necessary to the electrical field to to propagate at the speed of light the information about the new charge distribution. This means that the induced current will appear on the electrodes even if the carriers do not really reach them, what happens if they get trapped, or they recombined, etc.

The amount of induced current in the *i*th electrode is:

$$(1.1)\quad I_i = -q \cdot \vec{\upsilon} \frac{\partial \vec{E}}{\partial V_i},$$

where q is the amount of moving of moving charge, $\boldsymbol{\nu}$ is the drift velocity, $\boldsymbol{E}$ is the electrical field and V_i is the voltage of the *i*th electrode, the differential should being evalueted the potential constant on all other electrodes. The voltage swing induced by this unwanted current flow can change the logic state of the device, depending on amount of the induced charge and on the intrinsic properties of the circuit to which the device is connected.

If the carriers are produced outside the sensitive region, where the electrical field is not present, they either spontaneosly recombine (and they do not induce currents in the device electrodes) or start moving by diffusion. Strikes outside a depletion region can also result in a significant transient current as carriers diffuse into the vicinity of the depletion region field, where they can be efficiently collected. It is clear that generally there will be a fast (due to the prompt drif) and a slow (due to diffusion) component of the induced current. Note that even for direct hit (i.e. hits within the junction), diffusion plays a role as carriers generated beyond the depletion region can diffuse back toward the junction.

A transient disturbance in the junction electrostatic potential, which was termed the "field funnel," (fig. 1.2) can occur when charge generated along the particle track locally collapse the junction electric field due to the highly conductive nature of the charge track and separation of charge by the depletion region field. This funneling effect can increase charge collection at the struck node by extending the junction electric field away from the junction and deep into the substrate, such that charge deposited some distance from the junction can be collected through the efficient drift process.

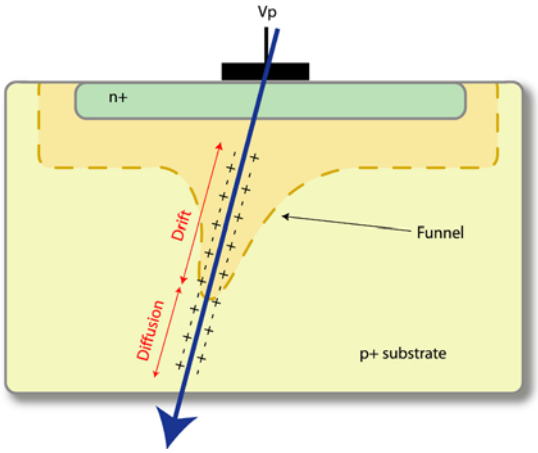

Fig. 1.2 Funneling of the junction field to the charge deposited by a ionizing particle

While in some cases the role of the funnel is important to charge collection in isolated p/n junctions with constant applied bias, it is less significant in the case of static circuits such as SRAMs, where reverse-biased transistor junctions are connected to active external circuitry. In this scenario, the applied voltage at the struck junction is not constant, and in fact very often the struck node may switch from being reverse-biased to zero-biased. This loss of bias at the struck node tends to lessen the importance of drift collection (and hence the funnel) as the single-event transient proceeds [10]. In such cases, funneling may play a role in the early-time response of the circuit by helping initially flip the node voltage, but it is late-time collection by diffusion that ensures the bit stays flipped.

1.3 Total dose effects

1.3.1 Introduction

Energetic particles incident on a solid lose their energy to ionizing (production of electron-hole pairs) and non ionizing (displaced atoms) processes as they travel through a given material.

As already mentioned above, the homogeneous accumulation of ionizing dose deposition over a long time on insulators is at the origin of the Total Ionizing Dose (TID) effect, mainly due to the most numerous particles (e-, p+) and lead to parametric degradation of the electrical performance of the devices. The accumulation of non-ionizing dose deposition, due to protons or high energy electrons, generate lattice defects leading to the Displacement Damage Effects (DD), with the consequent degradation of electrical parameters or increased background noise.

1.3.2 Displacement damage

The primary lattice defects initially created are vacancies and interstitials. A vacancy is the absence of an atom from its normal lattice position. If the displaced atom moves into a non-lattice position, the resulting defect is called an interstitial. The combination of a vacancy and an adjacent interstitial is known as a close pair or Frenkel pair.

Radiation-induced defects may be relatively far apart and are referred to as point defects or isolated defects. For example, incident electrons and photons with energy of the order of 1 MeV produce such defects. Defects may also be produced close together and form a local region of disorder (defect cluster or disordered region), such as those ones produced by incident neutrons with energy of the order of 1 MeV. The mechanism involved is the initial transfer of a significant amount of energy from the neutron to a single Si atom. The dislodged primary knock-on atom then displaces many other Si atoms locally, thereby creating a disordered region.

The primary effect of displacement damage that lead to the degradation of material and device proporties is the introduction of new energy levels in the band gap, associated

with defects (a new energy level arise from a disturbance of lattice periodicity). These defect states, or centers, have a major impact on the electrical and optical behavior of semiconductor material

Once defects are formed by incident radiation, those defects will reorder to form more stable configurations. Defect reordering is also temperature dependent (thermal annealing) and dependent on the excess carrier concentration present (injection annealing). Furthermore, the reordering of defects with time or increased temperature to more stable configurations can also result in more effective defects, where in this case the process is often referred in the literature as reverse annealing, in contrast to the more typical process of forward beneficial annealing. Defect reordering is usually called annealing and typically implies that he amount of damage and its effectiveness are reduced. Damage effectiveness depends on many factors, including particle type, particle energy, irradiation temperature, measurement temperature, time after irradiation, thermal history after irradiation, injection level, material type (n-or p-type) and impurity type and concentration.

Radiation-induced levels in the band-gap can give rise to several processes, including generation, recombination, trapping, compensation, tunneling, scattering, type conversion and field enhancement of carrier generation effectiveness. In principle any combination (or all) of these processes can occur; the role a particular level plays depends on variables such as carrier concentration, temperature, and the device region in which it resides. For instance, thermal generation of electron-hole pairs through radiation-induced defects centers near midgap is important in device depletion regions. Introduction of such centers increases the thermal generation rate, which is the mechanism for leakage current increases in silicon devices. Another type of effect is the recombination of electron-hole pairs, a process in which a free carrier one sign is first captured at the defect center, followed by capture of a carrier of the opposite sign. Recombination removes electron-holes pairs as opposed to the generation process. The mean time a minority carrier spends in its band before recombining is referred to as the recombination lifetime. Radiation-induced recombination centers cause the lifetime to decrease: this is the dominant mechanism for gain degradation due to displacement damage in bipolar transistors. A

third effect is the temporary trapping of carriers at a typically shallow level. In this process a carrier is captured at a defect center and is later emitted to its band, with no recombination event raking place. In general, trapping of both majority and minority carriers can occur (at separate levels). Radiation-induced traps are responsible for increasing the transfer inefficiency in charge-coupled devices.

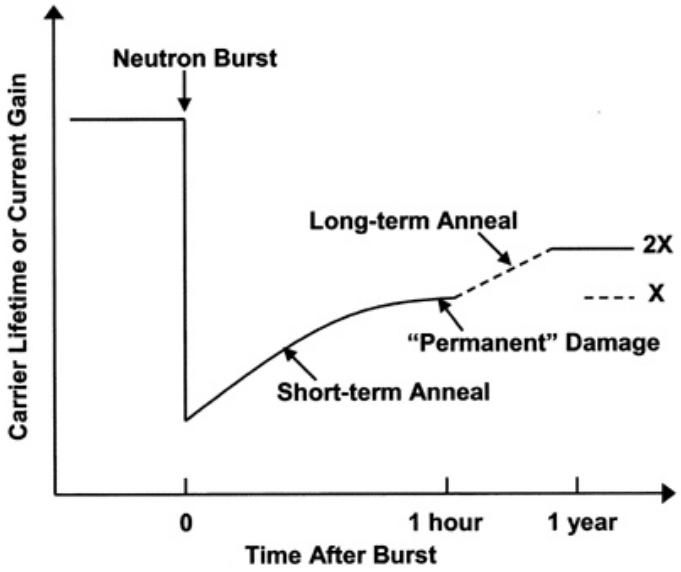

Fig. 1.3 Conceptual illustration of a short term and long term annealing at room temperature of displacement damage in bulk silicon and silicon devices [11]

1.3.3 Total dose effects

Even if incident radiation is not strong enough to produce lattice displacement damage or to trigger a SEE, it can still induce damage into a device when it releases energy by ionization into a sensitive area, like the conductor/semiconductor interfaces in MOS structures. When an MOS transistor is exposed to high-energy ionizing irradiation, electron-hole pairs are created uniformly throughout the oxide; in oxide, the electron-hole pair creation energy is ~17 eV. Electron-hole pair generation in the oxide leads to almost all total dose effects: the generated carriers induce the buildup of charge, which can lead to device degradation. The effect of the ionization on MOS devices depends upon the way that this charge is transported and trapped at the silicon-silicon dioxide interface.

The net effect of ionizing radiation on MOS device oxides depends upon the oxide thickness, the field applied to the oxide during and after exposure, as well as trapping and recombination within the oxide. The manufacturing processing techniques strongly affect the latter factor.

After pair creation, in general, some of electrons will recombine with holes (depending on the material, the kind of radiation and the applied field, which acts separating the pairs); the fraction of electron-hole pairs escaping recombination is called "yield". Immediately after electron-hole pairs are created, most of the electrons will drift in picoseconds toward the gate, where they are collected, while holes, which mobility in Si is far lower than those of electrons, remain where they have been generated. After this process, the holes undergo a hopping transport over the Si/SiO2 interface, through localized states in oxide. As the holes approaches the interface, some fraction of the holes will be trapped, forming a positive oxide trap charge. Hydrogen ions (protons) are likely released as holes "hop" through the oxide or as they are trapped near the Si/SiO_2 interface. The protons can drift to the Si/SiO_2 where they may react to form *interface traps*. In addition to oxide-trapped charge and interface-trap charge buildup in gate oxides, charge buildup will also occur in other oxides including field oxides and silicon-on-insulator (SOI) buried oxides.

Semi-permanent effects on MOS devices and circuits caused by the buildup of space charge in the SiO_2 layer fall into several categories, such as voltage offsets or shifts, induced parasitic leakage currents, speed (mobility) degradation.

In general, the effect of radiation-generated charge, $\Delta\rho$, on the threshold voltage shift, ΔV_{th}, of a transistor is given by

$$(1.2)\quad \Delta V_{th} = \left(-1/C_{ox}\right)\int_0^{t_{ox}} \Delta\rho(x)\left(x/t_{ox}\right)dx\,,$$

where t_{ox} is the oxide thickness, C_{ox} is the oxide capacitance and x is measured from the gate-SiO_2 interface. From equation (1.2) it can be seen that positive charge, i.e., trapped holes, will cause a negative shift in the threshold voltage of a device, while negative charge will cause a positive shift in the threshold voltage. In general, the initial

response of an MOS transistor to radiation is a negative shift in the threshold voltage, due to buildup of trapped holes. For sufficiently large amounts of trapped positive charge, the n-channel device may be turned on even for zero applied gate bias. In this case the device is said to have gone into “depletion mode”. When strongly into depletion, the n-channel device ceases to function because it cannot be switched from the “on” to the “off” state: it is always on!

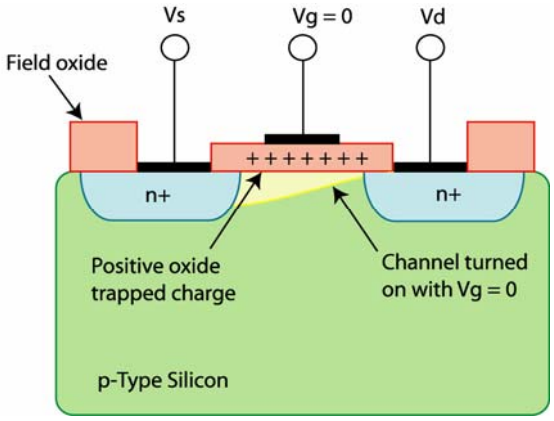

Fig. 1.4 Cross section of an MOS transistor illustrating charge buildup in the gate oxide

Figure 1.5 shows these effects for a typical commercial process: hardened devices will exhibit much lower threshold shifts primarily because of recombination in the oxide. Present commercial CMOS technologies will usually fail at levels between 10 and 50 krad(Si).

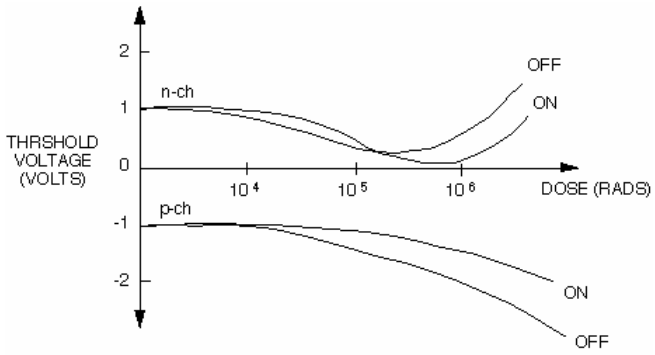

Fig. 1.5 Voltage shift due to irradiation

Charges gathered in the thick field oxide also turn on a parasitic leakage path at the edges of the gate metal, where current can flows from source to drain outside the channel

region. The irradiation induced shift of the gate-oxide curve is small due to the thin thickness of gate oxide layer; on the contrary, while the contribution of the field oxide leakage current is negligible before irradiation, after it becomes the major effect. This is due to the bigger thickness of the field oxide respect to the gate one, this resulting in a larger voltage shift per dose unit. The combination of two effects together leads the leakage current to raise of several order of magnitude after irradiation, which is often enough to cause functional failure of the devices.

2. Single Event Effects

Single events acquire that name because they depend on the interaction of a single particle with a semiconductor device. The effect of ionizing particles on electronic components results essentially from the track (electron-hole pair column) they form in matter by a Coloumbian interaction with electrons. Under the effect of internal or applied electric fields, the so created carriers may reach the electrodes generating currents in the external circuit. This uncontrolled charge injection resulting from direct ionization can produce an assortment of effects on the device operation. These effects are known as single event effects (SEEs). Depending on several factors, the particle strike may cause no observable effect, a temporary disruption of circuit operation, or even permanent damage to the device or integrated circuit.

SEE can be caused by the passage of a single heavy ion (a cosmic ray in space, for example) but also high energy protons can initiate single event effects. It is not the proton passage that produces the effect, as it produces only a very small amount of ionization and very few devices are sensitive enough to respond to the proton ionization. However, 1 proton in 10^5 will have a nuclear reaction in the silicon device. These reactions can produce heavy ions that in turn can deposit enough energy to cause upset.

2.1 Introduction

2.1.1 Brief history of SEEs

The first confirmed report of cosmic-ray-induced upsets in space was presented at the NSREC in 1975 by Binder *et al.* [12]. In this paper, four upsets in 17 years of satellite operation were observed in bipolar J–K flip–flops operating in a communications satellite. The authors used scanning electron microscope (SEM) exposures to determine

the sensitive transistors and, using a diffusion model, calculated a predicted upset rate within a factor of two of the observed rate. Due to this so small number of observed errors, the importance of SEU was not fully recognized until 1978–1979, when significant numbers of SEU-related papers were presented at the NSREC.

The occurrence of soft errors in terrestrial microelectronics manifested itself shortly after the first observations of SEU in space [13]. This watershed paper from authors at Intel found a significant error rate in DRAMs as integration density increased to 16 to 64K. The primary cause of soft errors at the ground level was quickly diagnosed as alpha particle contaminants in package materials. Radioactive contaminants in the water used by the factory were contaminating the ceramic packages of devices.

In the late 1970s, evidence continued to mount that cosmic-ray-induced upsets were indeed responsible for errors observed in satellite memory subsystems, and the first models for predicting system error rate were formulated [14]. By this time satellite memory systems had increased in size and on-orbit error rates of one per day could not be ignored.

Even though the first papers attributed memory upsets to direct ionization by heavy ions, by 1979 two groups reported at the NSREC on errors caused by proton and neutron indirect ionization effects [15] [16]. This was a highly important discovery, because of the much higher abundance of protons relative to heavy ions in the natural space environment. It also meant that not only would SEE be caused by galactic cosmic rays, but also by solar event protons and neutrons trapped in the Earth's radiation belts. The paper by Guenzer *et al.* [16] was the first to use the term "single-event upset", and this term was immediately adopted by the community to describe upsets caused by both direct and indirect ionization. The year 1979 also brought the first report of single-event latchup (SEL), an important discovery given the potentially destructive nature of the failure mode.

In the early 1980s, research on SEU continued to increase and methods for hardening ICs to SEU were widely developed and used throughout this decade [17], [18]. There were also few studies on another emerging and potentially troubling single-event issue: errors due to single events in combinational or imbedded logic.

The 1990s saw two major developments that continued to increase the importance of SEEs. One was the dramatic decrease in the number of manufacturers offering radiation-hardened digital ICs. This (among other factors, such as the increased functionality and performances they could provide) led to the increased usage of commercial electronics in spacecraft systems. However, their relative sensitivity to SEE presented significant challenges to maintaining system reliability. The second development was the continued advance in fabrication technologies toward smaller IC feature sizes and the higher speeds and more complex circuitry that scaling enables. These advances typically increase sensitivity to SEE, even to the point of terrestrials errors in a benign desktop environment, and may also lead to new failure mechanism. These two development led to an interesting convergence of mission from two historically disparate communities: space and military vendors driven toward commercial (non radiation hardened) circuits and commercial vendors driven toward a very real concern about SEE in the everyday consumer environment.

As we enter the 21st century, increasing sensitivity to SEU is expected to continue, both in memories and core logic. Upset in terrestrial electronics are serious reliability concern for commercial manufacturers. At the same time, feasibility of traditional SEU-hardening techniques is becoming questionable, especially because of fewer dedicated rad-hard foundries implementing them. Circuit design that are inherently radiation resistant (Hardening By Design, HBD) are receiving considerable attention [19], [20].

2.2 Single Event Effects mechanisms

2.2.1 Introduction

The following section will review the major types of single event phenomena, which can be classified into several categories (in order of permanency):

- Single event upset (soft error)
- Single event latchup (soft or hard errors)
- Single event burnout (hard failure)

- Single event gate rupture (hard failure)

2.2.2 Single Event Upset (SEU)

Single event upset, or SEU, is the most common type of single event effect. SEU is caused by the deposition of a charge in a device by a single particle, that is sufficient to change the logic state of a single bit (from one binary state to another). Single bit upsets are sometimes called soft errors because a reset or a rewriting of the device results in normal device behavior thereafter. An SEU may occur in analog, digital, or optical components, or may have effects in surrounding interface circuitry to which they are connected, but this strongly depends on the nature of the interconnections. Some memory devices are also susceptible to multiple bit upset, in which more than one bit is upset. This can be caused by a single ion traveling essentially parallel to the die surface, depositing energy in the sensitive volume of a consecutive line of memory cells, or striking the die close to normal, depositing enough energy in two or three adjacent cells to upset them. Multiple-bit SEU is a problem for single-bit *error detection and correction* (EDAC) where it is impossible to assign bits within a word to different chips (*e.g.*, a problem for DRAMs and certain SRAMs). A severe SEU is the single-event functional interrupt (SEFI) in which an SEU in the device's control circuitry places the device into a test mode, halt, or undefined state. The SEFI halts normal operations, and requires a power reset to recover.

Single event upset can also be caused by the generation of a transient which a device may interpret as a new bit of information. These transient are spurious signals that can propagate through the circuit path during one clock cycle. these signals can either propagate to a latch and become fixed, or be overwhelmed by the legitimate synchronous signals of the circuit in which case they are ignored.

2.2.3 Single Event Latchup (SEL)

Circuits are made by combining adjacent p-type and n-type into transistors. Paths other than those chosen to form the desired transistor can sometimes result in so-called

parasitic transistors, which, under normal conditions, cannot be activated. A latchup is the inadvertent creation of a low-impedance path between the power supply rails of an electronic component, triggering the above mentioned parasitic structure, which then acts as a short circuit, disrupting proper functioning of the part and possibly even leading to its destruction due to overcurrent. A power cycle is required to correct this situation.

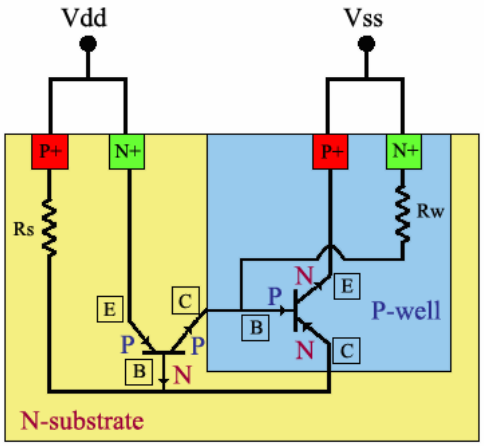

Fig. 2.1 Lateral section of a p/n/p/n structure with two parasitic BJTs

The parasitic structure is usually an equivalent of a thyristor (or Silicon Controlled Rectifier, SRC), a PNPN structure which acts as a PNP and an NPN transistor stacked next to each other. During a latchup, when one of the transistors is conducting, the other one begins conducting too. They both keep each other in saturation for as long as the structure is forward-biased and some current flows through it - which usually means until a power-down. The SCR parasitic structure is formed as a part of the totem-pole PMOS and NMOS transistor pair on the output drivers of the gates.

2.2.4 Single Event Gate Rupture (SEGR)

Dielectric breakdown can occur when the electric field across an insulating material exceeds some threshold value. When initiated by an energetic particle strike to the gate region of an MOSdevice, this phenomenon is referred to as a single-event gate rupture (SEGR).

Single-event gate rupture has been studied most extensively for power devices such as double-diffused power MOSFETs (DMOS), so we will use this device or describing the SEGR mechanism.

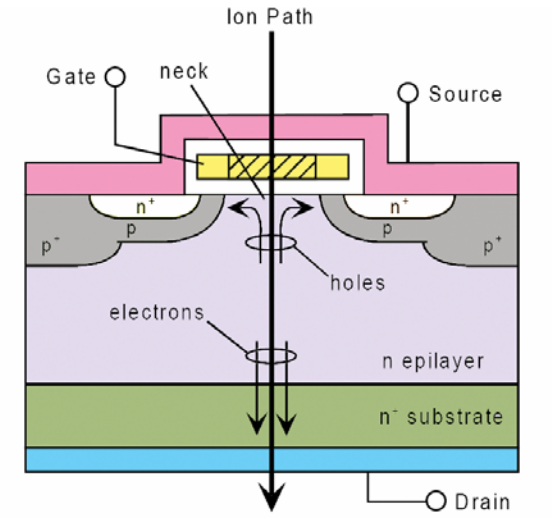

Fig. 2.2 **Structure of a vertical power MOSFET and current flow paths following a heavy ion strike**

As shown in fig. 2.2, current flow in the DMOS structure is vertical rather than lateral as in a standard MOSFET. Application of a positive bias to the gate in this nchannel DMOSFET inverts the p-body region to form a channel between the n-source at the top of the structure and the drain (substrate) contact at the bottom of the structure. To handle large currents, the full structure usually contains hundreds or thousands of these cells connected in parallel. The thick lightly-doped epitaxial region allows the power MOSFET to sustain high voltages without breakdown. When an ion strikes the neck region through the gate oxide, SEGR can occur as charge is transported near the Si/SiO_2 interface. As charge from the ion strike accumulates underneath the gate region (and depending on the gate bias), the electric field in the gate insulator can temporarily increase to above the critical field to breakdown, causing a localized dielectric failure (i.e., an SEGR). The SEGR response in vertical power MOSFETs has two components [22]. The “capacitor response” describes the interaction of the ion directly with the gate dielectric, inducing an oxide breakdown at a lower field than would occur in the absence of the ion strike. If a drain bias is applied when the ion strike occurs, part of the drain

voltage may be transferred through the epitaxial layer to the gate interface [23]. This part of the response is referred to as the "substrate response." Increasing the gate voltage increases susceptibility to SEGR through the capacitor response by increasing the pre-existing electric field in the oxide. Increasing the drain voltage also increases the susceptibility to SEGR because part of this voltage can be coupled to the interface through the substrate response.

SEGR effects have been studied for some time in power devices, but a topic that has recently received a considerable amount interest is SEGR in logic and memory ICs. As gate oxide thicknesses decrease, SEGR could become a problem in ICs because they will likely be operated at somewhat higher electric fields.

2.2.5 Single Event Burnout (SEB)

Single event burnout (SEB) due to heavy ions, neutrons and protons has been observed both in power MOSFET and in bipolar transistor. SEB is a destructive failure mechanism that comes about due to a parasitic bipolar transistor structure inherent to some devices. Looking at the power MOSFET structure in fig.2.2, a parasitic bipolar transistor is formed by the n-source (emitter), p-body (base) and n-epitaxial (collector) regions. Following an ion strike, currents flowing in the p-body can forward bias the emitter-base junction of the parasitic BJT due to the finite conductivity of the p-body region. The parasitic BJT is now operating in the forward active regime, and if the drain-to-source voltage is higher than the breakdown voltage (BV_{CEO}) of the parasitic BJT, avalanche multiplication of the BJT collector current can occur. If this positive feedback (regenerative) current is not limited, it can lead to junction heating and the eventual burnout of the device [21].

2.2.6 Single Event Snapback (SES)

Single Event Snapnack is a stable, regenerative condition similar to latchup caused by a drain-to-source breakdown in normal n-MOS transistors. Like latchup, the resulting condition is a high current state that can lead the device to failure (fig. 2.3)

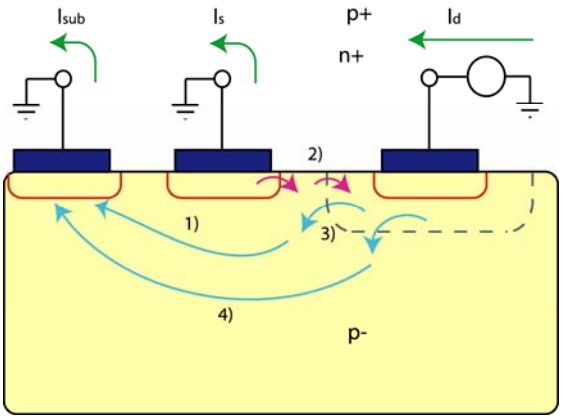

Fig. 2.3 Snap back mechanism in n-MOS structure

Unlike latchup, a p-n-p-n four layer structure is not necessary to have a snap back. Snap back is initiated by avalanche breakdown of the drain junction by current injection into the n-MOS transistor body, or by excess body current after an high dose rate radiation pulse or an heavy ion strike. After an ion hit, excess current near the drain junction results in avalanche multiplication and injection of holes that flow in the body region to the body contact (1) and cause the potential at the source-body junction to increase. If an avalanche condition is sustained long enough due to a sufficiently large current pulse, the source-substrate junction becomes forward biased turning on the parasitic npn bipolar transistor and injecting electrons into the substrate (2). As these feed into the drain, additional avalanche multiplication occurs (3), causing an increased substrate current and completing the regenerative feedback mechanism (4). Snap back cannot be triggered unless an external circuit provides sufficient current; for this reason, it is usual observed onto I/O stages of ICs equipped with large current drive pull up transistors. It is not observed in p-channel devices because the ionization rate for holes is much lower than for electrons, and regenerative feedback is consequently much lower.

2.3 Single Event Effects in devices

2.3.1 Introduction

We've seen how an ion strike releases charge along its path through a semiconductor and how this charge can be collected by p/n junctions, but what really matters is determining whether the event actually causes an error in circuit operation. In the following subsections we'll study how charge collection interacts with the circuit type and design to create a single-event upset. The focus will primarily be on memory circuits, as this will be the main field of application of the equipment described in this thesis.

2.3.2 Single-Event Upset Mechanisms in DRAMs

SEUs in terrestrial electronics were first observed in DRAMs [13], [24]. This kind of memories have historically been quite susceptible to soft errors because they rely on passive storage of charge (no active regeneration path) to represent information, allowing to any (no matter how small) disturbance of the stored information by a particle strike (by funnel-assisted drift or diffusion) to become persistent until corrected by external circuitry. There is no inherent refreshing of this charge packet (e.g., charge resupply through a load device) and no active regenerative feedback as one observes in latches and SRAM cells. What is so often referred to as a bit flip, the transition from one stable binary state to the other, is not required in DRAMs for an SEU to occur. A degradation of the stored signal to a level outside the noise margin of the supporting circuitry is sufficient to lead to erroneous interpretation and a resultant error. DRAMs have therefore received less use in space systems as engineers have preferred SRAM technologies. As the need for very large amounts of on-board memory is increasing, the use of DRAM technologies in space systems is becoming more common.

DRAMs are prone to SEU due to three primary mechanisms: storage cell errors, bit-line errors, and a combination of the two.

Figure 2.4 illustrates the mechanism for storage cell errors in a field plate capacitor DRAM [25]. In this kind of DRAM a stored "0" is represented by electrons occupying a

potential well under the field plate, while a stored “1” corresponds to electrons being depleted under the plate.

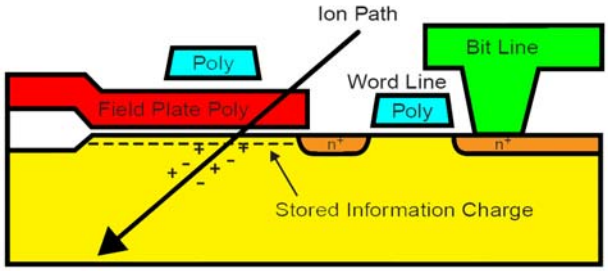

Fig. 2.4 **Illustration of storage cell SEU in a field-plate DRAM. Collections of electron at the reverse-biased field plate reinforces a stored “0”, but can lead to an upset of a stored “1”.**

Following a particle strike, electrons can be collected at the reverse-biased field plate. In the case of a stored “0”, this just reinforces the original state, but a stored “1” can look like a stored “0” after electron collection.

Bit-line errors can result if sufficient charge is collected during a read cycle to create a charge imbalance on the precharged bit lines. Because they can only occur during a read cycle, bit-line errors have a direct dependency on the read access frequency, with an increasing error rate as the access frequency increases. Bit-line errors can be caused by strikes to the access transistor drains along the floating bit-line or strikes to the sense amplifier circuitry itself. Because of their inverse dependency on cycle time, bit-line errors become a significant reliability concern as memory speeds increase.

A new failure mode for DRAMs was demonstrated almost twenty years ago when it was found that charge collection at both the storage cell and bit line that was insufficient to individually cause an upset could cause an error in combination [26]. This new failure mode, dubbed the combined cell-bit line (CCB) error, was shown to dominate the storage cell and bit-line error rates for very short cycle times. The three components of soft errors in a 512K DRAM are shown in fig. 2.5 as a function of the cycle time.

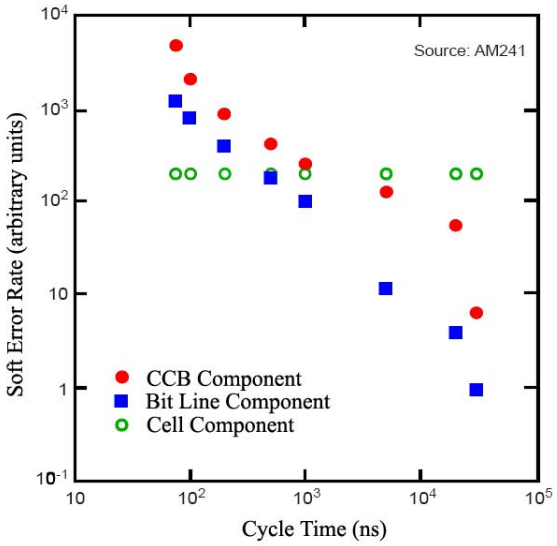

Fig. 2.5 Components of soft-error rate in DRAM [26]. The storage cell component is not dependent on the cycle time, while soft errors involving the bit lines increase dramatically as the cycle time decreases.

Note the independence of storage-cell errors on cycle time, and the domination of CCB errors for short cycle times.

2.3.3 Single event upset in SRAM

The upset process in SRAMs is quite different from DRAMs, due to the active feedback in the cross-coupled inverter pair that forms a typical SRAM memory cell, as illustrated in Figure 2.6. When an energetic particle hits a sensitive location in a SRAM (typically the reverse-biased drain junction of a transistor biased in the "off" state, T_1 in figure), charge collected by the junction induces a transient current in the struck transistor. As this current flows through the struck transistor, the restoring transistor ("on" p-channel transistor, T_2 in figure) sources current in an attempt to balance the particle-induced current. The current flowing through the restoring transistor, due to the finite transistor channel conductance, induces a voltage dropping at its drain (point *A* in fig. 2.6). T_2 drain is also connected to the gates of transistors T_3 and T_4. If the induced current is sufficient to lower the voltage of restoring transistor drain below a threshold voltage, the logical states of T_3 and T_4 will be inverted. This will consequently force the

voltage of point *B* to go to V_D (it was at zero before the hit), so switching T_1 and T_2 and changing the state of the cell as a result. The voltage transient that arises in response to the single-event current transient is actually the mechanism that can cause upset in SRAM cells. The voltage transient is essentially similar to a write pulse and can cause the wrong memory state to be locked into the memory cell. Competition between the feedback process and the recovery process governs the SEU response of SRAM cells. In fact, if the recovery current sourced by the restoring transistor is faster than the feedback one, the circuit will not flip, although the induced transient current is obviously still present.

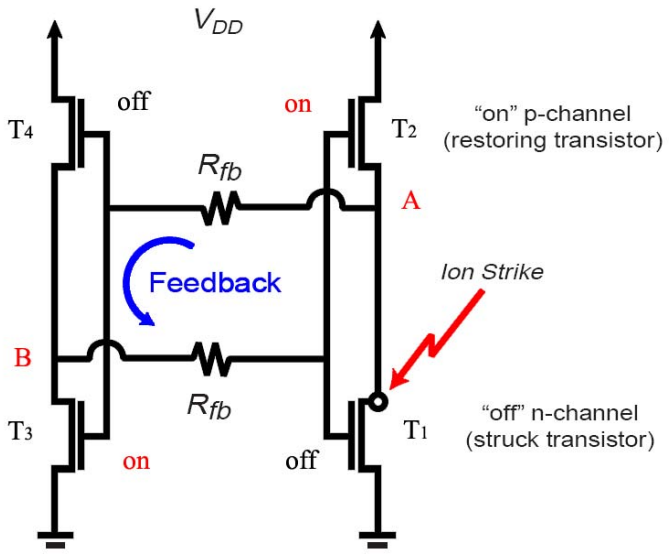

Fig. 2.6 Schematic layout of a CMOS SRAM cell.

Incident particles far below the upset threshold are often sufficiently ionizing to induce a momentary voltage "flip" at the struck node of an SRAM. Even particles with LET well below the upset threshold cause a significant voltage transient on single event transient at the struck drain. Whether an observable SEU occurs depends on what happens faster: the feedback of the voltage transient through the opposite inverter, or the recovery of the struck node voltage as the single-event current dies out. It must be noted that drift (including funneling effects) is responsible for the rapid initial flip of the cell, while long-term charge collection by diffusion prolongs the recovery process; both

mechanisms are critical to the upset process. The recovery time of an SRAM cell to a particle strike depends on many factors, such as the particle LET, the strike location, etc.

From a technology standpoint, the recovery time depends on the restoring transistor current drive and minority carrier lifetimes in the substrate [27], [28]. The cell feedback time is simply the time required for the disturbed node voltage to feed back through the cross-coupled inverters and latch the struck device in its disturbed state. This time is related to the cell write time and in its simplest form can be thought of as the RC delay in the inverter pair. This RC time constant is thus a critical parameter for determining SEU sensitivity in SRAMs: the smaller the RC delay, the faster the cell can respond to voltage transients (including write pulses) and the more susceptible the SRAM is to SEUs.

2.3.4 SEU in SOI devices

Due to their intrinsic structure, Silicon On Insulator (SOI) devices were regarded to be much less sensitive to upsets than conventional bulk silicon circuits. In a bulk Si transistor the charge generated by an ion strike is fully collected from the substrate region, regardless whether the gate or the drain has been hit. In a SOI transistor, instead, (see fig. 2.7) the volume area sensible to charge collection is made smaller by the buried oxide that prevents charge deployed into substrate to be efficiently collected. However, it has been shown how it is possible to have charge collection from below the buried oxide in SOI technologies that use a very thin buried (on the order of 200 nm) oxide layer [29].

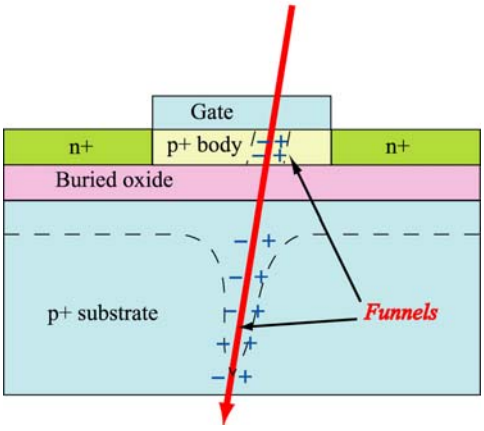

Fig. 2.7 Charge collection behavior in SOI transistor

For these technologies it has been measured that the saturated cross section (~8 μm2/bit) was closer to the sum of the active gate and drain areas (6.1 μm2/bit) rather than to the gate area alone (0.64 μm2/bit). This indicates that, contrary to the earlier beliefs, charge collection could also occur from the substrate below the buried oxide, at least in some SOI technologies. From past studies, it is known that charge collection occurs only when the substrate is biased in depletion or inversion mode, and the mechanism for charge collection at top electrode was assumed to be due to a capacitive discharge or to a displacement current. Recent studies and simulations [30] with dedicated microscopy experiments performed at microbeam facilities, led to a deeper understanding of this kind of phenomenon.

2.3.5 Single Event Upset in other circuits types

SEUs also occur in digital circuits other than memories, prime examples being microprocessors and digital signal processors. Errors in logic circuits are very sensitive to critical timing windows and logic paths, and may never propagate to the output pins. The erroneous information may be blocked by the superseding logic during the following clock cycles (i.e., the corrupted latch may become a “don’t care” member of a subsequent state of the logic). As circuit operating speeds continue to increase, the probability of a momentary glitch in a line voltage from a single-event transient (SET) propagating through a logic path to become an observable error rises. A SET is defined as a momentary voltage excursion (voltage spike) at a node in an integrated circuit. The voltage spike is originally formed by the electric-field separation of the charge generated by an ion passing through or near a circuit junction. Under certain conditions, the voltage spike can propagate away from where it was generated and eventually appear at the circuit’s output. It may also be captured either locally if it is generated within a latch, or non-locally if it first propagates through the circuit before being captured in a latch. Once the SET is captured it becomes an SEU, and it is impossible to distinguish SEUs that result from SETs that have propagated from other locations in the circuit from SEUs that have been generated within the latch itself.

In a logic circuit, charge collection due to a single-event strike on a particular node will generate a low-to-high or high-to-low voltage transition or a transient noise pulse. If this pulse is larger than the input noise margin of a subsequent gate, it will compete with the legitimate digital pulses propagating through the circuit. The possible propagation of this pulse to a latch (storage) element depends on several factors. First, the active combinational paths at that instant in time. The active combinational paths depend on the dynamic state of the logic as determined by the particular code vectors executed at that time (the present "state" of the logic). Second, assuming that an active path exists for the propagation of the noise pulse, the pulse will be shaped and phase delayed as it propagates through the intervening gates on its way to a latch. Third, the temporal characteristics of the noise pulse as it arrives at a latch are important. The pulse must arrive within the setup and hold (S/H) time of the latch element to be stored by the latch element. The clocking characteristics of the latch and the previous state of the latch contribute to this mechanism. If all three of the above conditions are properly met, then the SE-generated noise pulse will be captured by the latch as erroneous information. We define this as the generation of a soft fault (SF). SFs may also be generated by direct single-event strikes to the latch nodes, where the latch information is corrupted via a bit flip. In this case the effect is analogous to SEUs in memory circuits and can be modeled in a similar way. Once a SF has been identified, or a SF probability has been calculated, one knows the vulnerability of a circuit to single events and/or critical paths which may contribute a weak link for single-event tolerance. However, actual upset rates, which refer to the observable operation of a particular circuit located in a particular hostile radiation environment, cannot be immediately deduced from knowledge of SFs. Internal SFs may not be observable at the interface pins of a circuit (or the I/O ports of a subcircuit). For example, the particular latch effected by the soft fault may be part of a "don't care" state of the finite state machine; the change of state has no effect on subsequent operation of the circuit. Or, the erroneous latch data may be part of a data register that is scrubbed in a subsequent clock cycle. Thus, no observable error actually occurs. However, if the soft fault eventually propagates to one or more of the I/O ports of the circuit, then an externally observed error exists; we define this and only this event as an error event. It is

clear that one soft fault may cause erroneous information at many I/O ports and that this erroneous information may appear during many clock cycles.

3. Radiation environment

3.1 Introduction

3.1.1 Overview

As discussed in the previous chapter, Single Event Effects may occur when active electronic devices are exposed to radiation. To make reliable predictions about the behavior of devices and their reliability respect to SEEs, one know the radiation environment where the devices are expected to operate. Environments with high levels of radiation are called hostile. The most important hostile environments electronic devices have to deal with are:

- space environment;
- particle accelerator experimental halls;
- high altitude environments;
- nuclear plants;
- radiotherapy and nuclear medicine in general.

It is worth mentioning that no environment is free of radiation (cosmic rays at ground level, natural radioactivity of the Earth, of materials, etc.). On the other hand electronics and electronic systems are more and more present in everyday life and manage most safety critical applications. Hence concerns, regards the radiation sensitivity of any device that has to perform crucial or vital tasks, arise (e.g. CMOS electronics in commercial heart pace-makers; power electronics in trains;…). Considering the trends of electronics technology it will be vital to maintain high levels of confidence.

In this chapter we will describe in some detail the space radiation environment, and only briefly, for the reasons just mentioned, the atmospheric and ground level environments.

3.2 The space environment

3.2.1 Introduction

In the natural space environment radiation sources can be classified into two main categories: charged particles (electrons, protons, ions) trapped by the planetary magnetic field (trapped radiation) into belts surrounding the planet (called Van Allen belts for Earth), and transient particles coming from solar events (solar event particles, SEP) or from outside the solar system, called galactic events (galactic cosmic rays, GCR). Solar events, such as *coronal mass ejection* (CME) and *flares*, are unpredictable even if they correlate to the solar cycle. On the other hand, galactic events have a completely random distribution, giving unpredictable events of high energy, but are orders of magnitude less frequent than solar events.

Table 3.1 lists the maximum energy of space radiation particles. The table shows that much of the environment is high energy; therefore, shielding is not effective for many radiation source environments.

Particle	Maximum energy
Trapped electrons	10s of MeV
Trapped protons and heavy ions	100s of MeV
Solar protons	GeV
Solar heavy ions	GeV
Galactic cosmic rays	PeV-EeV

Tab. 3.1 Space environments particle maximum energies

3.2.2 Solar energetic particles

The activity level of the Sun follows a cyclical variation of active years followed by quiet years. The period of recent solar cycles has varied between 9 and 13 years, with an average of about 11 years. Solar cycle activity is frequently gauged by the observed number of sunspots, but many solar processes show the same variation. Importantly for the present case, this includes the incidence of energetic solar events, with maximum numbers of solar flares and coronal mass ejections (CMEs) occurring during active years. Solar events still occur during solar quiet times, but they occur less frequently.

Solar events can be broadly characterized as being either gradual or impulsive. The gradual events produce a raised particle flux that decays slowly over several hours or even days, and have been correlated to CMEs. These events are proton-rich and can produce high-energy (> 30 MeV) proton fluences higher than 10^9 protons/cm^2 accumulated over a few days. Gradual events are responsible for the majority of large proton fluence events, and occur at a frequency of about 10 per year during solar maximum conditions. Impulsive events may be associated with solar flare activity and are responsible for about 1000 small solar particle events per year at solar maximum [31], [32]. The flares can last for hours for large events down to only tens of seconds for impulsive events. A solar flare heats the solar gases to tens of millions of degrees Kelvin and accelerates protons and electrons that stream toward Earth. These *solar energetic particles* (SEP) streams are primarily composed of protons (90%), alpha particles (5-10%), and to a less extent heavy ions and electrons. Heavy ion fluences can be orders of magnitude above the galactic cosmic ray background and their energies range from tens of MeV/nucleon to hundreds of GeV/nucleon, but at the upper end of this range the flux falls below the galactic cosmic ray background. The duration of such bursts can last as long as several (Earth) days for longest flare events. The time particles need to reach Earth can vary from tens of minutes to several hours, depending on particles energy and point of origin in the sun, while the flux reaches its peak within two hours to one day. The decay time also varies from few days to one week. The most energetic protons arrive

to Earth in about 10-30 minutes. Figure 3.1 shows solar event proton fluences for the last three solar cycles, superimposed over a plot of the sunspot number [33].

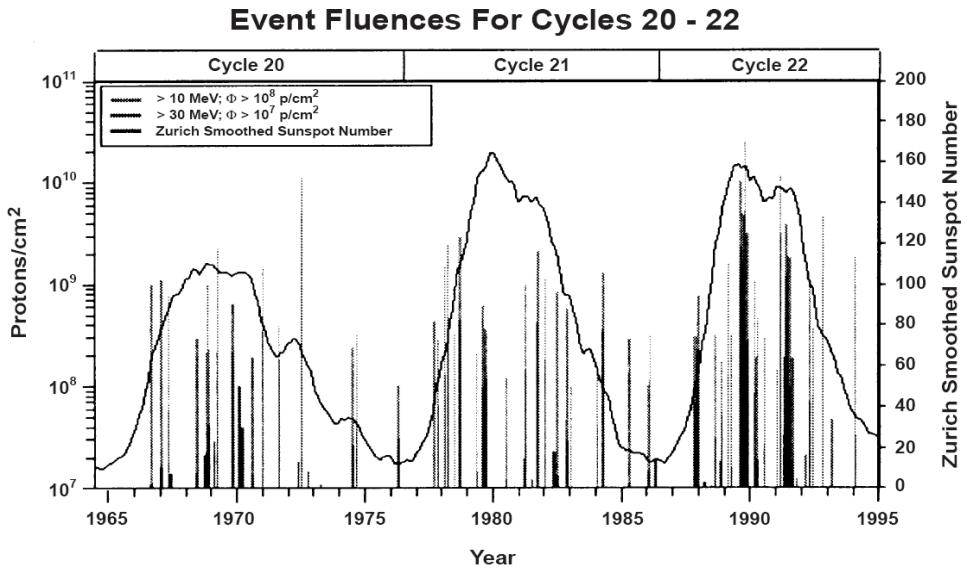

Fig. 3.1 Large solar proton events for the last three solar cycles. The number of sunpot is superimposed on the graph

The cyclical variation of the sunspot number is readily apparent, as is the fact that most (but not all) high-fluence proton events occur during solar active years. While solar particle events can be broadly classified as gradual or impulsive, individual events have their own very unique properties in terms of duration, particle fluence, energy spectrum, etc. Stassinopoulos *et al.* have presented a classification system where events are classified from small to extremely large, and solar cycles are classified from extremely mild to extremely severe [34]. It can be seen in Figure 3.1 that solar cycle 20 was in general extremely quiet with the exception of an extremely large solar event in August 1972; this solar cycle was classified as very mild. Solar cycle 21 was extremely mild, with no individual events of high-energy proton fluence > 10^9 protons/cm2. By contrast, solar cycle 22 had 8 events with high-energy proton fluence > 10^9 protons/cm2; this cycle is considered extremely severe. Some events (such as the August 1972 event) are actually a series of closely-spaced events, where proton fluxes have not yet decayed to their original level before the next event occurs. The importance of individual large solar

events cannot be overestimated – the August 1972 event by itself accounted for 84% of the total high-energy proton fluence received by spacecraft during the entire 20th solar cycle. Accurate models to predict worst-case particle fluence from solar events are crucial to appropriate parts selection and survivable spacecraft design.

3.2.3 Galactic Cosmic Rays (GCRs)

Solar event particles are true transient particles in the sense that elevated fluxes of particles are observed only for a short time following an event (although recall that following a large event increased levels of trapped particles are observed and in some cases can produce new trapped particle belts). In contrast, galactic cosmic rays (GCR) form a background component of radiation that shows a slow cyclical variation with solar activity. GCRs are composed of very highly energetic protons and heavy ions that come from outside the solar system. These particles must fight against the solar wind to enter the solar system and are therefore at their maximum intensity at solar minimum and drop off a factor of 2 to 10 at solar maximum. The cyclical variation of GCRs is shown in fig. 3.2, which is a plot of 25-95 MeV/nucleon He flux over a 20-year period as measured by the IMP-8 satellite [35].

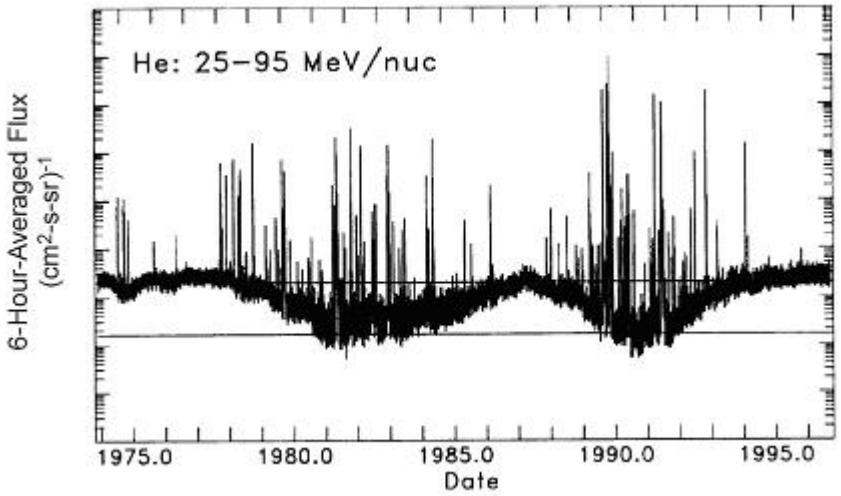

Fig. 3.2 Solar cycle variation of heavy ions (in this case He nuclei) as measured by the Cosmic Ray Telescope (CRT) aboard the IMP-8 satellite.

The spikes on this plot are due to increased heavy ion fluences from solar events. Note that these spikes are more likely to occur at solar maximum, when the baseline GCR heavy ion flux is lowest. The particle composition of GCRs is shown in fig. 3.3 [36].

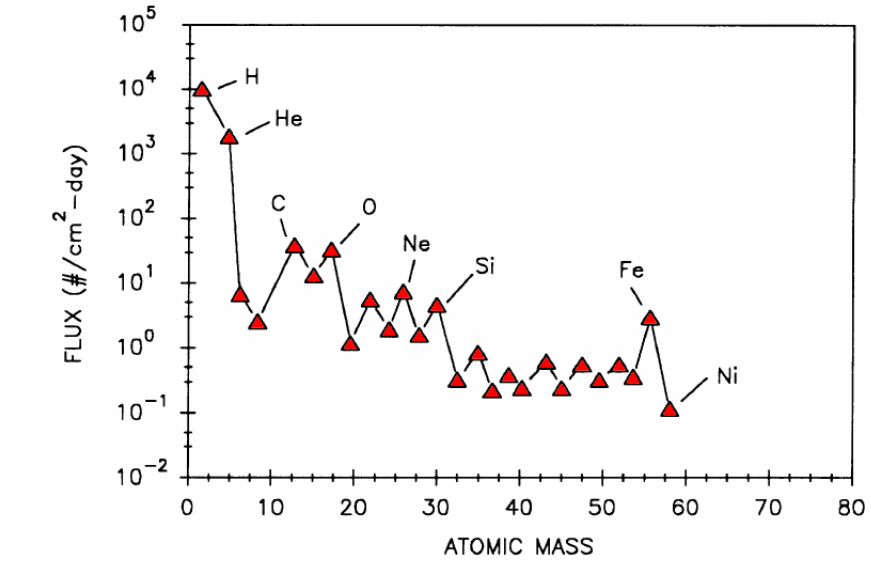

Fig. 3.3 Particle composition of galactic cosmic rays.

Protons comprise about 83% of the GCR flux, He nuclei (alpha particles) account for 13%, 3% are electrons, and the remaining 1% are heavier nuclei. Even though they are not very abundant, heavy ions are very important to SEE because they deposit the most energy per unit pathlength. Note that beyond Fe, the heavy ion flux drops dramatically. This turns out to be important, because the energy deposited by an ion per unit pathlength depends on its atomic number. Ions heavier than Fe are more ionizing, but are much less abundant. Therefore microelectronics that is radiation hard only up to Fe will experience low SEE rates. This is sometimes referred to as the "iron threshold." The energy spectra of Galactic Cosmic Rays ranges up to above 10 GeV/nucleon (fig. 3.4), plus an extremely low flux of GCR with energies that exceed 10^{12} eV/nucleon (TeV range).

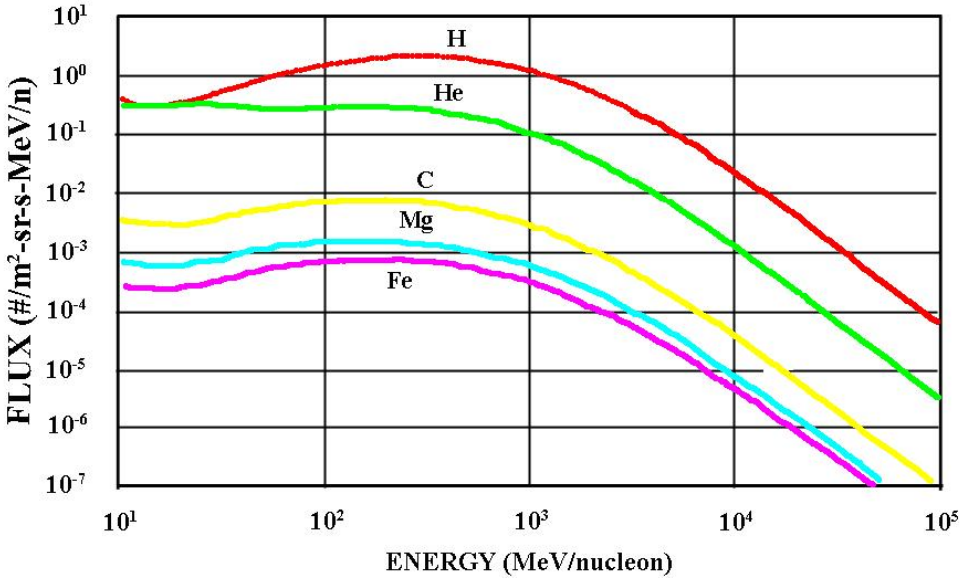

Fig. 3.4 Representative cosmic ray spectra

At these high energies, they do not become trapped and spacecraft shielding is ineffective in attenuating the particle flux. The differential energy spectra tends to peak around 1 GeV/nucleon near the Earth. GCRs with polar trajectories can penetrate to low altitudes because of the reduced geomagnetic rigidity in the polar regions. Spacecraft with high inclination angles are therefore at greatest risk of encountering SEE due to GCRs.

3.2.4 Trapped population

The Earth's magnetic field, generated by the convective motion in the molten nickel-iron core of the planet and by the residual magnetism in the planet crust, establishes a volume of space within which the field dominates charged particle motion. Close to the Earth the magnetic field is roughly a magnetic dipole that is tilted ~11.5° from the rotation axis and offset from the center of the Earth by about 500 km towards southern western side of the Atlantic Ocean. The dipole approximation is poor, and better models exist that account for the steady changes of the central field as well as the dynamic outer boundaries.

The magnetosphere is complex and dynamic because of its interaction with the variable solar wind and the transient phenomena from the Sun (fig. 3.5). On the sunward side, the magnetosphere extends ~10 Earth radii (R_e; $1R_e$=6370 km) from the Earth, and on the opposite side the magneto-tail extends beyond 200 R_e. The sunward dimension can change by more than a factor of 2 depending on the interplanetary medium upstream of the Earth.

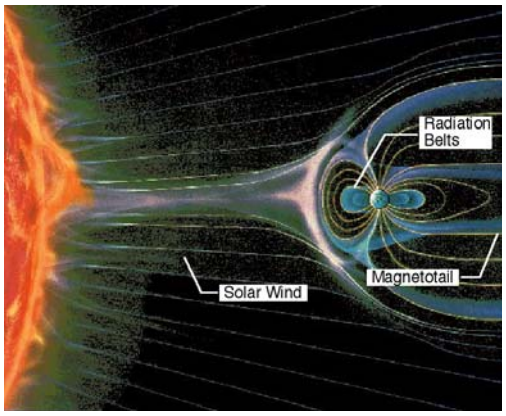

Fig. 3.5 Sketch of the Earth's magnetosphere and its interaction with the solar wind (not to scale).

Solar wind is a plasma of charged particles (protons, electrons, and heavy ions) generated by the expansion of solar corona. The solar wind is constantly streaming toward the Earth but its speed is always changing: the average speed is 400 km/s, while high velocity solar wind originates from coronal holes found at the poles of the sun. Solar wind affects Earth's magnetosphere compressing it on the sun side and expanding it on the tail side.

To basically define domains inside particle trapping regions, it is useful to refer to the dipole shell parameter L, defined as:

$$(3.1)\quad L = \frac{R}{\cos^2 \Lambda}$$

where R is the radial distance in Earth's radii ($R_\cdot$) and Λ is defined as the invariant latitude. There are combinations of particle charge, energy, and L-shell that lead to stable trapping in spatial "zones", called Van Allen radiation belts for Earth (fig. 3.6).

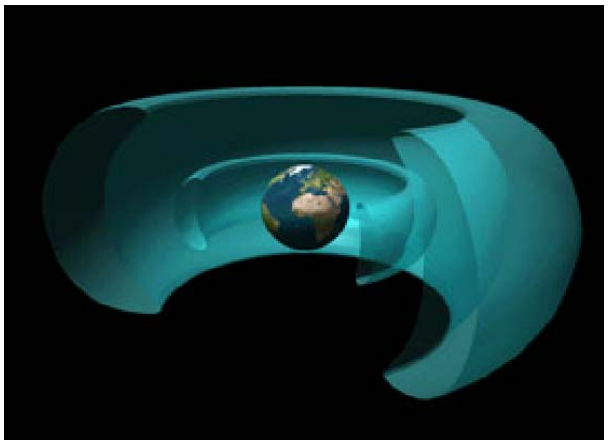

Fig. 3.6 Diagram of the Earth's Van Allen radiation belts

One should note that this representation, based upon the dipole approximation, is realistic up to *R* values equal to four Earth radii; the solar wind influence is not negligible for higher altitudes. In a naive picture of the main components of trapped radiation, one may to distinguish between an internal and an external region with respect to trapped electrons. The inner zone extends at the equator up to 2.4 R· and is defined by an *L* <= 2.8, while the outer zone ranges from L = 2.8 to *L* = 12, being this upper limit only an indication of the maximum outward extent of the stable trapping area. The region between *L* = 2 and *L* = 2.8 is called the "slot". The inner zone is often called the proton belt and the outer zone the electron belt. There are really electrons throughout the magnetosphere, including in the inner zone, as well as protons in the outer magnetosphere. In practice, the division into two zones is reasonable because these are the regions within which the radiation dose from trapped particles is typically most significant. The particles that contribute most to the dose in the inner zone are protons, and those contributing most in the outer zone are electrons. Fig. 3.7 plots the actual dose rate measured in the magnetosphere on board the CRRES satellite behind ~80 mils of Al, showing that indeed the belts have the structure in the cartoon of fig. 3.6 [37]

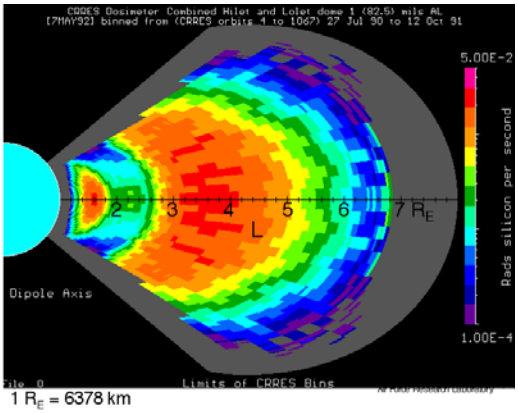

Fig. 3.7 Measured dose rate versus L shell and latitude on the CRRES satellite.

As already stated above, the Earth's magnetic dipole is offset from the geometric center of the planet. The offset causes a weaker field region over the South Atlantic Ocean and an opposing region of stronger field over northern Asia. As the trapped inner zone particles execute their bounce motion along field lines, they mirror at lower altitude in the "South Atlantic anomaly" or SAA. There, the Van Allen belts reach lower altitudes, extending downwards into the atmosphere. On the opposite side, the Southeast Asian Anomaly shows correspondingly higher magnetic field values and higher ceiling particle belts (fig. 3.8).

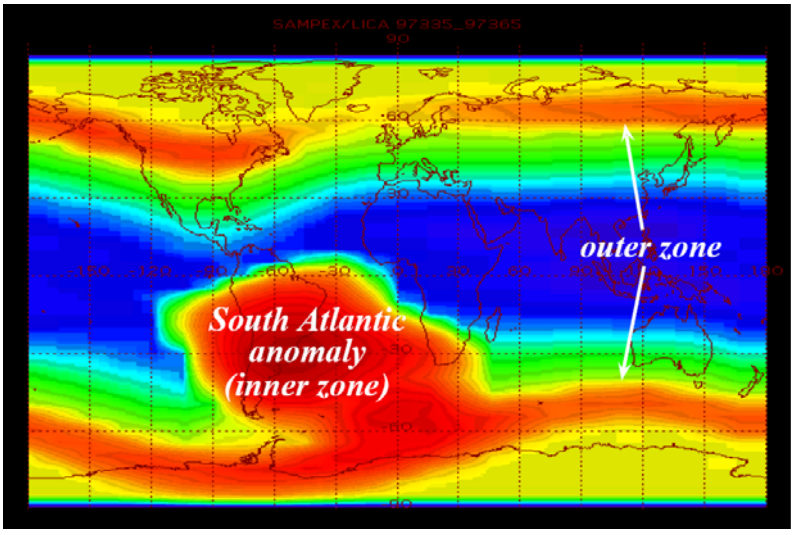

Fig. 3.8 Count rate (arbitrary units) of > 0.7 MeV protons and > 0.5 MeV electrons in Low Earth Orbit (LEO) measured on the NASA/SAMPEX satellite.

3.2.5 Magnetic rigidity and geomagnetic attenuation

Depending on the orbit of a spacecraft, the Earth's magnetosphere provides varying degrees of protection from transient particles of solar and galactic origin by attenuating the particle fluences. Charged particles that have a low momentum per unit charge are deflected at a certain depth in the magnetosphere and are cut off. When dealing with charged particles, rigidity is usually expressed in mega and giga volts [MV], [GV], where the rigidity expresses the particle energy divided by its charge. The magnetic rigidity is also related to the particle's energy E in MeV by:

$$(3.2)\quad r = \frac{A}{z}\sqrt{E^2 + 2M_0E}$$

where r is the magnetic rigidity in GV, A is the particle's mass in amu, z is the particle's charge and M_0 is equal to 931MeV. The subsequent relation gives the boundary dipole parameter L that a charged particle of magnetic rigidity R (in GV) can reach:

$$(3.3)\quad L = \sqrt{\frac{14.9}{R}}\,.$$

The rigidity is strongest at the magnetic equator where a particle must have a rigidity of -15 GV to penetrate and weakest at the poles where particles need a rigidity of <1 GV to penetrate.

The relation between L parameter and the energy and mass values a particle needs to have in order to penetrate Earth magnetic field to a depth L results (see fig. 3.9):

$$(3.4)\quad E = \sqrt{\left(m_0c^2\right)^2 + \left(\frac{Z}{A}R\right)^2} - m_0c^2 \quad [MeV]$$

As an example, for geostationary orbits (36000 km) magnetic shielding is relatively effective, as for such orbits the cut-off energy results above ~60 MeV for hydrogen and above 15 MeV/n for heavier ions.

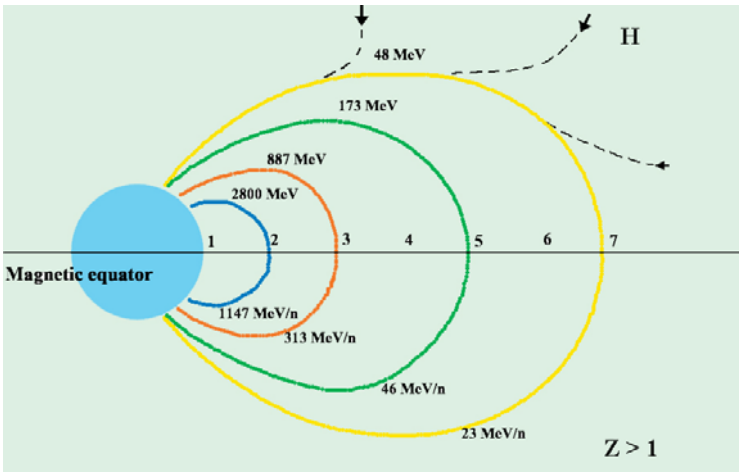

Fig. 3.9 Particle energy-rigidity-L relationship.

3.3 Atmospheric and ground environment

3.3.1 Atmospheric environments

A radiation environment also exists in the Earth's atmosphere and, although less harsh than the space environment, it can also give rise to SEE.

As cosmic ray and solar particles enter the top of the Earth's atmosphere they interact with air nuclei (mainly nitrogen and oxygen) and generate a "shower" (Fig. 3.10) of secondary particles and interactions. Products of the cosmic ray showers are protons, electrons, neutrons, heavy ions, muons, and pions.

In terms of SEE in the atmosphere, the most important product of the cosmic ray showers is the neutrons. They are measurable at 330 km altitude, and their density increases with decreasing altitude until they reach a peak at about 20 km. At altitudes less than 20 km, the levels decrease to where, at the ground, the neutron density is 1/500 of the peak flux. Our knowledge of neutron levels comes from balloon, aircraft, and ground based measurements. The energies of neutrons in the atmosphere reach energy levels of hundreds of MeV. The high-energy neutron fluxes that may induce SEE range between 10 particles/cm^2/h at sea level and 10^3 particles/cm^2/h at typical airplane flight altitudes of 30,000 feet, with modulation due to Sola Flares.

Studies published in the 1984 demonstrated that electronics in aircraft systems, which are subject to increasing levels of cosmic radiation as altitude increases, are also sensitive to single event effects. It has been demonstrated [38] that, below altitudes of about 60,000 feet, secondary neutrons from cosmic ray heavy ion fragmentation are the most important contributor to SEUs. Siberberg et al. [39] give a method for calculating the neutron SEU rate. They also predict that SEU rates increase with enhanced solar particle backgrounds. Since that time, several flight experiments have demostrated that energetic particles can cause single events effects in electronics at avionics altitudes. In a study completed in 1992 [40], SEU rates measured in flight were shown to correspond with atmospheric neutron flux levels, and rates calculated using laboratory SEU data agreed with the measurements.

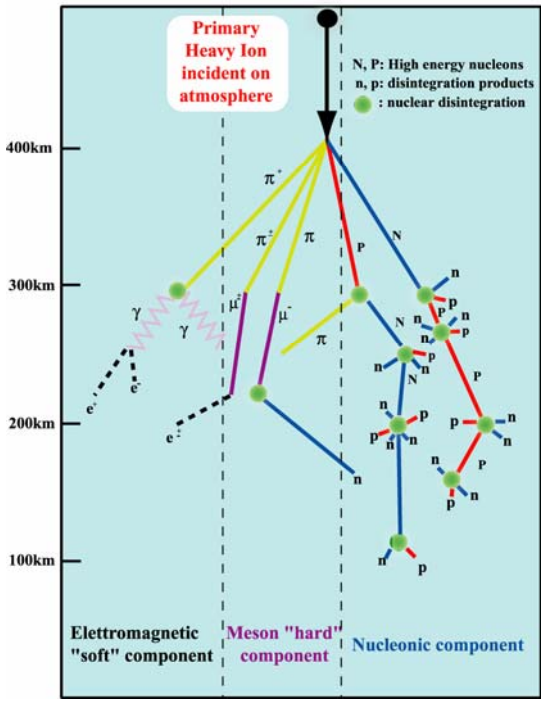

Fig. 3.10 Products of GCRs interaction with atmosphere

Because galactic cosmic rays are the primary particles that produce the secondary neutrons and protons in the atmosphere, it is the variations in the GCRS intensities that cause most of the variations observed in the secondary neutron and proton levels. For

example, neutron levels rise and fall in the same 11-year solar cycle that modulates the GCRS. Also, the ability of a heavy ion to penetrate the magnetosphere is determined by its magnetic rigidity which, in turn, is dependent on geomagnetic latitude. Magnetic disturbances occur more frequently during the active phase of the solar cycle increasing the ability of GCRS to penetrate the magnetosphere. Atmospheric conditions, especially barometric pressure, also affect the neutron levels.

3.3.2 Radiation on earth

Both natural and man-made radiation are present on the Earth. Table 3.2 lists these sources with their annual dose equivalents in units of milliSievert. The sources that are most important in producing effects in microelectronics on the ground are terrestrial and cosmic rays, which induce single event effects.

Source	Type	Annual Dose
Terrestrial	Natural	0.26
Inhaled radionuclides	Natural	1.0
Internal radionuclides	Natural	0.26
Cosmic radiation	Natural	0.28
Cosmogenic radionuclides	Natural	0.01
Medical diagnostc	Man-made	0.92
Atmospheric weapons testing	Man-made	0.05
Airline travel	Natural	1.6 (crew) 0.03 (passenger)
Consumer products	Man-made	0.04
Nuclear power	Man-made	<< 0.01

Tab. 3.2 Annual dose from ground radiation in mSv [41].

Cosmic radiation on the ground is from the products of sixth and seventh generation interactions of GCR and solar particles in the atmosphere. The population has a high vertical directionality. Variations in the primary population intensities cause most of the variations observed in the secondary neutron and proton levels. Levels rise and fall in the same 11-year solar cycle that modulates the GCRs. Sea-level cosmic rays are reduced by 30% during solar active periods. However, during large solar particle events, ground level enhancements (GLEs) of the terrestrial cosmic rays can increase the levels by as much as 5000% depending on location and the size of the event. Studies have shown that the variation in the neutron flux level is measurable when the altitude ranges from sea level to mountainous regions.

The first evidence of sea-level soft fails (single event upsets) on 16 Kb DRAMs was given by May and Woods [13]. The source of the radiation was traced to alpha particle emission from contaminates in ceramic packing produced in a factory on the Green River, Colorado, which was downstream from an old uranium mine. In 1978 Zeigler realized that, if alpha particles from materials could induce soft fails, it is possible that ground cosmic rays could do the same thing. Several experiments followed, demonstrating a distinct increase in soft fail rates with increasing altitude above sea level.

There are many products from the cosmic radiation showers so it was important to determine which were dominant in causing the soft fails. At the 1983 NSREC, Dicello [42] concluded that all types of particle radiation could cause soft fails at the ground level with some probabilities. Ziegler and colleagues began an effort to define the cosmic ray terrestrial environment based on the work of many researchers who began studying cosmic radiation after Hess' balloon experiments [43]. The focus of the work was on defining neutron spectra as a function of altitude as shown in fig. 3.11. In the figure, the altitude dependence is expressed as atmospheric depth: the lowest curve at 1030 g/cm^2 is at sea level and the curve marked 700 g/cm^2 is at an altitude of 2 miles.

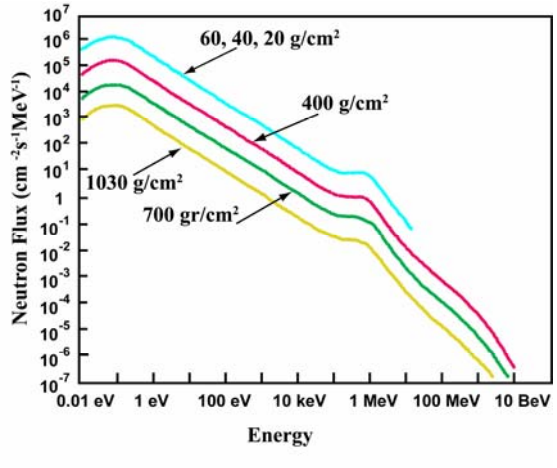

Fig. 3.11 Measured energy spectra of neutrons at various altitudes up to outer space.

4. SEE studies

4.1 SEEs modeling

4.1.1 Introduction

Modeling Single Event Effect rates in a microelectronic device involves a combination of assumptions about the physics of the device, detailed knowledge of the radiation environment and experimental data. The device physics that underlies SEE involves charge generation along the path of a primary or secondary ionizing particle, charge collection on circuit nodes and the response of the circuit to the charge transient. Both the total collected charge and the rate of charge collection can be important to triggering a single event effect. Models that predict SEE rates typically use ground test data to extract information about the device sensitivity, measured in terms of cross section σ and critical charge (Q_C), as a function of LET and/or proton energy. The experimentally measured cross section for a device can be expressed as the ratio between the number of SEE counted and the particle fluence for a given LET:

$$\sigma = \frac{counts}{fluence}\left[cm^2\right] \quad (4.1)$$

Once the cross section versus LET (or the cross section versus proton energy) has been measured, there are established techniques for using the data to predict SEE rates in a given radiation environment. The rate prediction methods do a fairly good job of predicting what is actually observed in a radiation hostile environment, such as onboard a spacecraft.

As a first approximation the occurrence of SEEs is driven by the quantity of deposited energy. This allows one to reduce all ion types and energy distributions present in the

radiation environment to their LET and to calculate the deposited energy by integrating the LET along the ion trajectory throughout the sensitive volume. With this simplification, the problem is to define the size of the sensitive volume, calculate the rate of ion hits and the consequent energy depositions, and determine the fraction of total ion hits that cause SEEs. The SEE rate is the product of the sensitive area on the chip by the flux of ions in the environment that can cause the considered event. The problem is complicated by the angular dependence since the amount of energy deposited in the sensitive volume depends on chord length, which in turn depends on angle of incidence of the striking ion.

4.1.2 The chord length model for heavy ion SEE prediction

This model was first proposed by Pickel and Blandford in 1978 [44] and was later implemented in several simulation codes. This method models the sensitive volume as a right rectangular parallelepiped (RRP) with lateral dimensions x and y and thickness z (fig. 4.1). The ion path through the RRP is s and is determined by thickness, z, and the angle of incidence, θ, between the xy plane. Charge is also allowed to be collected along a funneling distance, s_f, that adds to s for the charge calculation.

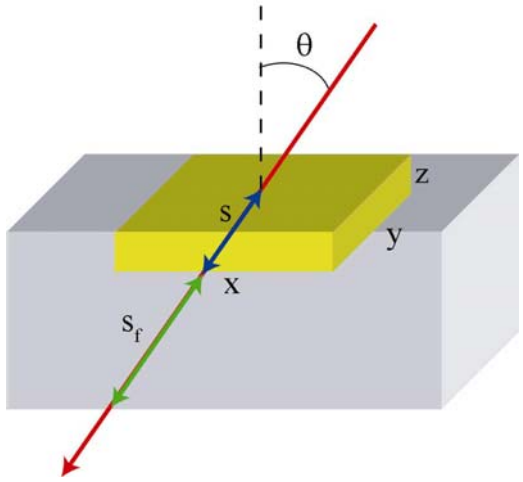

Fig. 4.1 Schematic of the RPP model parameters

The energy deposited in the sensitive volume from an ion interaction with LET, L, is

$$(4.2)\quad E \approx \left(s + s_f\right)L\,.$$

This energy is converted to ionization charge and it is assumed that all the charge generated within the charge collection length $s+s_f$ is collected by the sensitive volume circuit node. This model is also based on the following assumptions: ion plasma track structure can be ignored, ion LET is constant along a chord s through the sensitive volume, charge collection by diffusion from ion strikes external to the RRP can be ignored and there is a sharp threshold for upset, i.e. ions with a LET below threshold will not cause SEEs, ions with a LET above the threshold will always give SEEs.

To get a SEE rate $R(E_C)$ prediction, the model integrates the LET distribution and the expected ion flux over the chord-length modulated by an analytic differential distribution $f(S)$ function relation:

$$(4.3)\quad R\left(E_c\right) = A_p \int_0^{\left(x^2+y^2+z^2\right)^{1/2}} \Phi\left[L_t\left(s, E_c\right) f\left(s\right)\right] ds$$

where the integration goes from zero to the maximum path-length through the RPP, A_p is the average projected area of the RPP, $\Phi(L)$ is the integral flux, E_c is the threshold energy for generating Q_c and $L_t(s, E_c)$ is the minimum average LET depending on chord length through

$$(4.4)\quad L_t\left(s, E_c\right) = \frac{E_c}{s + s_f}\,.$$

As already mentioned above, the RPP model assumes a step function for cross section versus LET value. However, most devices show a gradual rise from threshold to saturation, rather than a step function. This behavior is due to the superposition of composite response of multiple types of sensitive volumes, with different thresholds and with distribution of their parameters. To solve this issue, it has been proposed [45] to divide the cross-section curve into several steps in order to more accurately represent it.

The generally accepted approach is to integrally weight *R(E)* with the normalized experimental cross-section data

$$(4.5)\quad R = \int_{E_c}^{E_{sat}} R(E) f(E) dE$$

where the integration range is from the measured threshold, E_c, to the measured value at saturation, E_{sat}, and *f(E)* is the cross-section versus LET curve converted to a probability density, described by the four parameter Weibull distribution:

$$(4.6)\quad f(E) = 1 - \exp\left[-\left(\frac{E - E_c}{W} \right)^S \right],$$

where E_C is the threshold energy, while W and S two shape parameters used to fit the curve to the experimental data. The *f(E)* function represents the rate at which an energy of E is deposited in the sensitive volume. It can be regarded as the probability density for an event caused by deposition of an energy quantity equal or greater than E. This approach is commonly called the integral RPP (IRPP).

4.1.3 Prediction for proton-induced SEU

Only the most sensitive devices (such as high density DRAMs and CCDs) are sensitive to SEU from proton direct ionization because proton LET is too low. However, protons can cause SEU through nuclear reactions, which result in recoils that can deposit enough energy in the sensitive volume to cause upsets even in less sensitive devices such as SRAMs.

To get reliable proton induced SEE predictions the key step is to determine the energy spectra of recoils as a function of the material and the incoming proton energy; the knowledge of the energy distribution of the recoil products will then allow to estimate SEE rates following the heavy ion model. The model shown here [46] has been derived by observing how protons SEU cross-section data (as a function of proton energy) follow

a relationship resembling the proton nuclear cross section in silicon. The Bendel parameter, A, was introduced on a semi-empirical basis; the original formulation had both a threshold and a limiting cross section but observed that the single parameter *A* was adequate to describe the data available at the time. As more data became available, it became clear that the response of some modern smaller feature size devices was better modeled with the use of both parameters. An improved two-parameter Bendel model was suggested by two groups at about the same time, and this is the form that currently has the widest acceptance [47], [48]. The two-parameter model is expressed as

$$(4.7)\quad \sigma_p = \left(\frac{B}{A}\right)^{14}\left[1-\exp\left(-0.18Y^{0.5}\right)\right]^4$$

where σ_p is a cross section in units of 10^{12} upsets per proton/cm^2 per bit, *A* and *B* are empirically determined constants unique to a device and

$$(4.8)\quad Y = \sqrt{\frac{18}{A}}\left(E-A\right)$$

with E as proton energy in units of MeV.

The parameter A is related to the apparent upset energy threshold, while the ratio $(B/A)^{14}$ is associated with the saturation cross section observed at high energies. The one-parameter model has *B* fixed at a value of 24. The advantage of the two-parameter model is that it allows better fitting of the experimental data in the high energy regions, particularly for small geometry devices, while preserving the apparent low energy proton upset threshold. Also for protons, a closer fit matching can be obtained by the superimposition of Weibull's distribution curves with different fixed parameters. The important thing to notice here is that, in contrast with heavy ions case, the proton upset rate depends on the probability of a nuclear interaction to happen within the whole device size, and not only during the path of the proton in the device active volume.

4.2 Test with accelerators

4.2.1 Introduction

The final goal of this thesis is to describe a new tool to measure the SEE sensitivity of electronic devices to ionizing radiation. In this chapter we will give a review of the traditional methods employed to perform this kind of measurement, underlining the strong and the weak aspects of currently adopted techniques.

4.2.2 Laboratory accelerator based measurements

The essential part of any SEE qualification process is actually performing test measurements: electronic devices undergo radiation tests to check their behavior under controlled conditions that well reproduce the environment where they are expected to work in. Simulation tools derived from first principles are certainly useful in providing some indication of SEE device sensitivity of a particular type of device, but reliable predictions of actual performances may not be made without real data, possibly collected with the very same type of device.

As seen in the previous chapter, the radiation environment in space is widely varied in composition, energy, orbital position, time, and it is largely omnidirectional. To validate a component or device for use in the space environment, irradiation facilities at particle accelerators are routinely used to test the SEE sensitivity of electronic components in controlled and repeatable conditions. A broad variety of ion species, with adequate energies, are required to perform reliable tests.

The energy of a certain type of particle delivered by an accelerator sets the LET (*Linear Energy Transfer*) and the range; i.e. the depth the particle will travel inside the target. Of course the LET of a particle varies with energy and hence it changes along the particle trajectory as the particle slows. As already mentioned, the LET is the main reference parameter in SEE testing and one assumes that different particles with the same LET will affect the circuit the same way. The range is clearly important because the impinging particle must be able to reach the active volume of the device and therein

deposit an adequate amount of energy. By knowing the range (initial energy) of the particle one can evaluate the LET at the depth of the active volume. Using ions with different ranges allow one to get information about the circuit active depth; i.e. the depth beyond which further energy deposition does not affect more the device behavior.

Clearly range and surface LET are critical parameters for competitive SEE testing. An ideal SEE facility should provide a wide range of energetic ion species. In practice a facility will be limited if heavy ions, the most useful in establishing the plateau (saturation) SEE cross-section, do not have enough energy to penetrate to the electronically active layers.

Tandem accelerators are used for SEE testing because they offer a wide selection of heavy ion species, they are robust and easy to use. The energy resolution, after momentum analysis, is very good ($\Delta E/E$ better than 10^{-4}). In Table 4.1 are listed some of typical ions species available at the 15 MV Tandem of the Legnaro Laboratories. The LET values reported are the surface LET value at the beam energy; i.e. the values as the ion enters a piece of silicon before losing energy.

Ion	Energy (MeV)	LET (MeV × cm^2/mg)	Range (μm)
$^{1}H^{1+}$	28	0.02	4390
$^{7}Li^{3+}$	56	0.37	378
$^{11}Be^{5+}$	80	1.01	195
$^{12}C^{6+}$	94	1.49	171
$^{16}O^{7+}$	108	2.84	109
$^{19}F^{8+}$	122	3.87	99.3
$^{28}Si^{11+}$	157	8.59	61.5
$^{35}Cl^{12+}$	171	12.5	49.1
$^{48}Ti^{14+}$	196	19.8	39.3
$^{58}Ni^{16+}$	220	28.4	33.7
$^{63}Cu^{16+}$	220	30.5	33.0
$^{79}Br^{18+}$	241	38.6	31.3
$^{107}Ag^{20+}$	266	54.7	27.6
$^{127}I^{21+}$	276	61.8	27.9
$^{197}Au^{26+}$	275	81.7	23.4

Tab. 4.1 Ion surface LET and range in silicon for typical ion species available at the Legnaro Tandem accelerator.

Tandems are however somewhat limited in energy. Indeed the active volumes of the latest generation microelectronic devices are buried below several metallization layers and to test them requires ions with greater ranges (fig. 4.2).

SEE tests are of course performed with more energetic types of accelerators (cyclotrons, linacs, booster systems). These are less mono-chromatic, but as ion LET and range depend weakly on energy this is not a problem. However the issue of high quality energy resolution beams is of capital importance if there is the need for micro-focusing the beam down to micron size, a well-established technique to perform microscopic SEE testing.

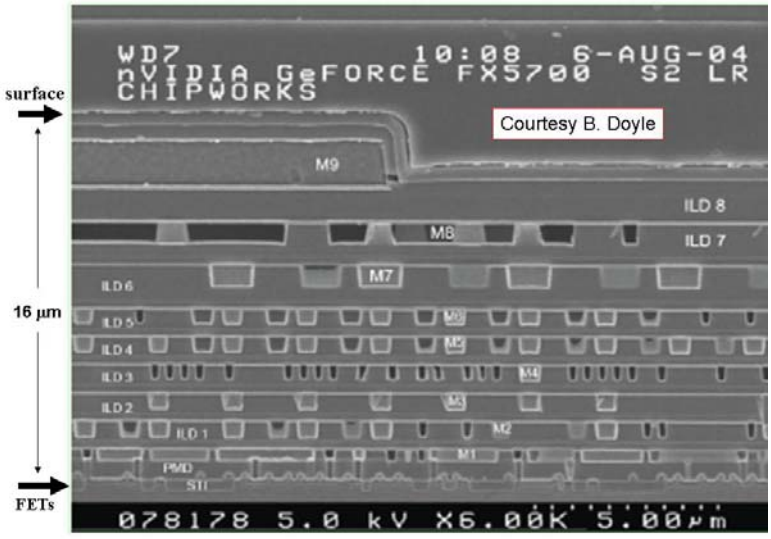

Fig. 4.2 **A cross-section of a modern device showing the thick metallization layers (courtesy B. Doyle). The active volumes (FETs) are 16µm below the surface.**

4.2.3 Cross-section measurement

The occurrence of SEE in a device depends on the total amount of charge collected by an active volume and this depends on the total ion path length in the active part of the device. The SEE sensitivity is assumed to be completely described by the geometry of the sensitive volume and the critical charge Q_c associated with the particular type of single event effect. The critical charge is the amount of charge that must be collected in an

active volume of the device to cause an event and depends primarily on the circuit characteristics.

In SEE testing one wants to determine the device sensitivity as a function of the amount of charge deposited. The path length and hence the charge deposited in a thin layer depends on the angle of incidence of the particle and hence it is possible to measure the SEE sensitivity over a range of charge deposition by simply varying the angle of the beam. However, the results need to be normalized to the effects of the beam at normal incidence. This idea leads to the concept of effective LET:

$$(4.9)\quad LET(eff) = \frac{LET(0^\circ)}{\cos(\vartheta)}.$$

Device sensitivity measurements are then expressed as a function of effective LET. This technique works if the particle reaches depth of the active volume; i.e. range > depth/cos(ϑ).

The goal of a sensitivity test is to measure the SEE cross section as a function of the effective LET. The experimental SEE cross section is given by:

$$(4.10)\quad \sigma_{SEE}(effective\ \mathrm{LET}) = \frac{SEE\ count}{effective\ fluence}\left[cm^2\right] = \frac{SEE\ count}{fluence \times \cos\vartheta}\left[cm^2\right]$$

where the *effective fluence* is the particle fluence of the beam (respect to a unit surface normal to the beam) multiplied by the cosine of the incidence angle of the beam on the tilted taget.

The results of a SEE measurement usually takes the form of a saturation-like curve with an onset at some threshold LET which then goes to an asymptotic value at higher LET values. The threshold LET determines the critical charge, the asymptotic cross section gives the area of the sensitive volume. This information, combined with the thickness of the sensitive volume, is sufficient to calculate the SEE rates of many types of devices in any given radiation environment.

A typical test consists of a series of exposures with well-defined beams (energy and fluence) over a range of LETs (or effective LETs) to allow a determination of the cross-section curve. During each exposure, the device is placed under bias, either active or passive. The SEE of interest are recognized and counted by the control electronics driving the device during irradiation, while the particle fluence is obtained from beam dosimetry.

For phenomena regarding memory elements, like SEU, the cross section can also be given per bit by simply dividing the global SEU cross section by the number of irradiated bits per unit area:

$$\sigma_{SEE}\left(effective\,\mathrm{LET}\right)=\frac{\sigma_{SEE}\left(effective\,\mathrm{LET}\right)}{bit\ \mathrm{into}\ device}\left[\frac{cm^2}{bit}\right]. \tag{4.11}$$

SEUs in static RAMs best exemplify many aspects of SEU testing. Each RAM cell is, to first order, identical, and from an SEE perspective, the device is easily seen to be an array of sensitive volumes. Tests are usually performed by loading a pattern in the memory array, exposing the device to a known fluence of charged particles at a particular LET. The exposure is stopped and then the array is interrogated to count the number of flipped bits, and the cross section is calculated. Since each sensitive volume is identical, the per-bit cross section is simply the measured cross section normalized to the number of bits in the memory array. A complete experiment uses many LET values to obtain a full cross section curve of the SEE of interest.

The SEE cross section often depends on other factors, such as electrical bias or temperature, and deviates from a strict dependence on effective LET. In reality, the cross section is not a step function, but a Weibull curve (fig. 4.2) that increases with a finite slope in the threshold region, followed by a knee region, and a gradual approach to the asymptotic cross section. These deviations can be due to statistical variations in the sensitive volume geometry or in the critical charge for a volume and are significant for calculating event rates. Another source of deviation in the shape of the cross section occurs when the unit cell has more than one sensitive volume, or when several different

types of cells are present, each with their own characteristic sensitive volume. In such a case one may observe a stair-shape curve which is the superposition of a many Weibull curves each with different threshold and plateau LET values (fig. 4.3).

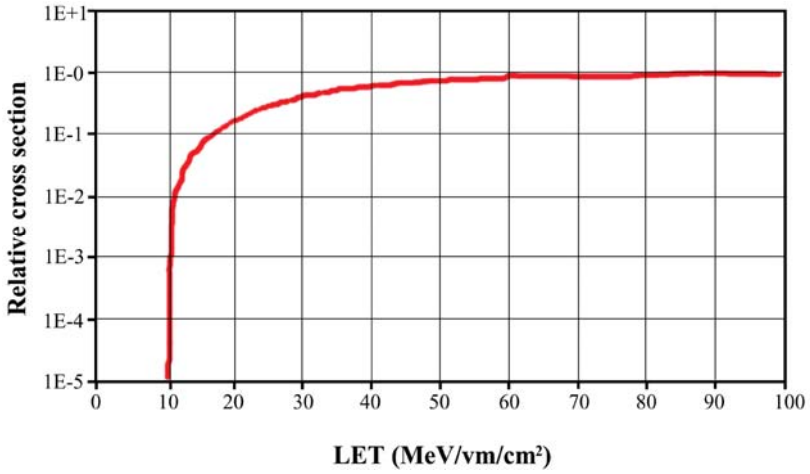

Fig. 4.3 Representative heavy ion cross section curve with cross section expressed as a function of effective LET. This curve has Weibull parameters: L_0= 10MeV/mg/cm^2,W=30 MeV/mg/cm^2, shape parameter = 1.6.

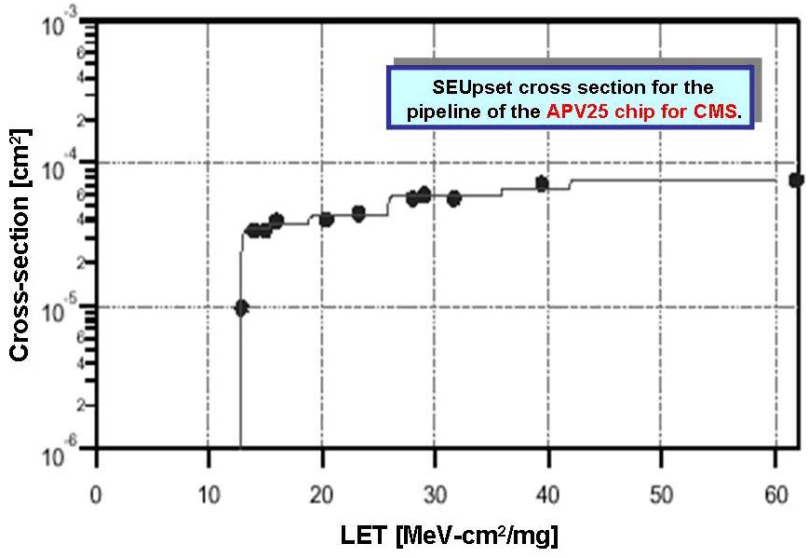

Fig. 4.4 The SEU cross-section experimental data and multiple-Weibull fit of the pipeline of the APV25 frontend chip for the CMS detector at LHC. [49]

4.2.4 Proton SEE testing

Energetic protons generally do not deposit enough energy in a sensitive volume to directly cause SEEs. However, approximately one in 10^4 to 10^6 protons undergo reactions with nuclei of the Si atoms in the device and produce energetic residual range nuclei (recoils or fragments). If produced in or near a sensitive volume, the residual nuclei can deposit enough energy to cause an SEE. The residuals are short-range ions that will deposit most or all their energy within the sensitive volume.

Proton testing proceeds much like heavy ion testing in that the sample is exercised while exposed to a beam for a given fluence. Events are counted in each exposure, and the event cross section is calculated by dividing the number of events by the fluence for the exposure (recall that the effective fluence is used for heavy ion testing). This procedure is repeated over a range of proton energies to fully characterize the cross section as a function of energy. Three issues, however, make proton testing significantly different from heavy ion testing. First, and foremost, samples experience significant total ionizing dose damage when exposed to proton beams (to obtain useful statistics in proton testing one must compensate the very small probability of indirectly causing a SEE by irradiating up to relatively high proton fluences, several orders of magnitude higher than those used with heavy ion testing), and the event cross section can be different as damage accumulates. Care must be taken to plan experiments so that the device characteristics are not unduly altered during the measurements. Second, since the nuclear interaction probability does not depend on the beam incident angle and the reaction products deposit nearly all their energy in the sensitive volume, the cross section is assumed to only depends on the proton energy. As a result, for proton testing, there is no equivalent concept to the effective LET used in heavy ion testing. Finally, the physical layout of proton exposure facilities and safety concerns for human experimenters adds considerable complication to experiment and equipment design.

4.3 Radiation Effect Microscopy (REM)

4.3.1 Introduction

In previous paragraphs, an overview of device characterization with respect to SEE sensitivity was given, and the concept of global cross section was introduced. This type of tests provides fundamental data regarding the reliability of electronic circuits in radiation environments: the knowledge of the cross section curve versus LET allows one to predict how a device will be affected from a random exposure to ionizing radiation. As the whole device, or a macroscopic portion of it, is exposed to a broad beam, this method cannot indicate the specific reason for radiation sensitivity. To do so would require knowing the location of the ion impacts. Device simulations can be used very effectively to pin point the sensitive parts of a device; e.g. determine which parts of a device are sensitive to SEE (e.g. which transistor in a latch; which logic element in an IC; etc. etc.). But experimental data is ultimately desirable, if only because data is necessary to validate any simulation.

Radiation Effects Microscopy (REM) provides a way to correlate device response (occurrence of an SEE; anomalous *ion beam induced charge collection* (IBICC)) to the impact points of incoming particles. REM experiments are usually performed with a microprobe system that systematically scans the device under test with a low-intensity highly focused ion microbeam.

4.3.2 A REM example

A famous example of REM has been performed by SANDIA laboratories [50], where predictions resulting from simulations with DA VINCI code and experimental results were compared.

Two CMOS6r SRAM ICs were studied in this work, a 16 K SRAM test chip known as the TA788, and a 256 K SRAM standard evaluation circuit (SEC) known as the SA3953 (fig. 4.3).

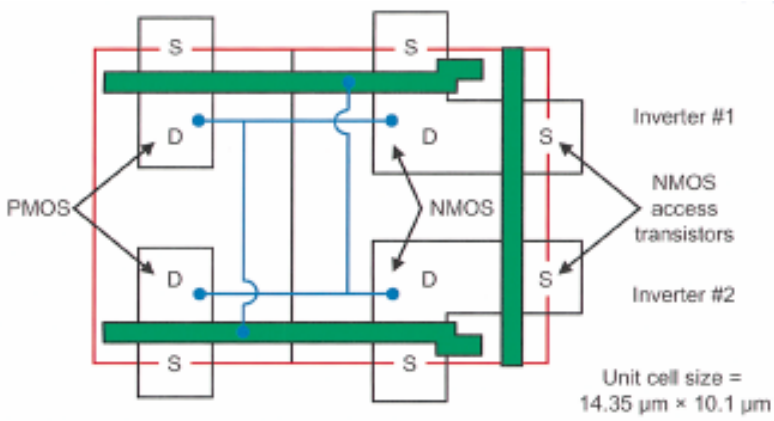

Fig. 4.5 Layout of 256 K 6-transistor SRAM unit cell (D = drain and S = source). The red box indicates the boundaries of the unit cell, the green regions are the gate polysilicon lines, and the blue lines show the interconnections within the unit cell.

The simulations were performed for energetic ion strikes incident every 0.5µm throughout the unit cell to give a map of the SEU-sensitive area of the SRAM unit cell. By repeating these simulations for several ion/energy combinations, the evolution of the sensitive area as a function of ion LET has been generated, as shown in fig. 4.4.

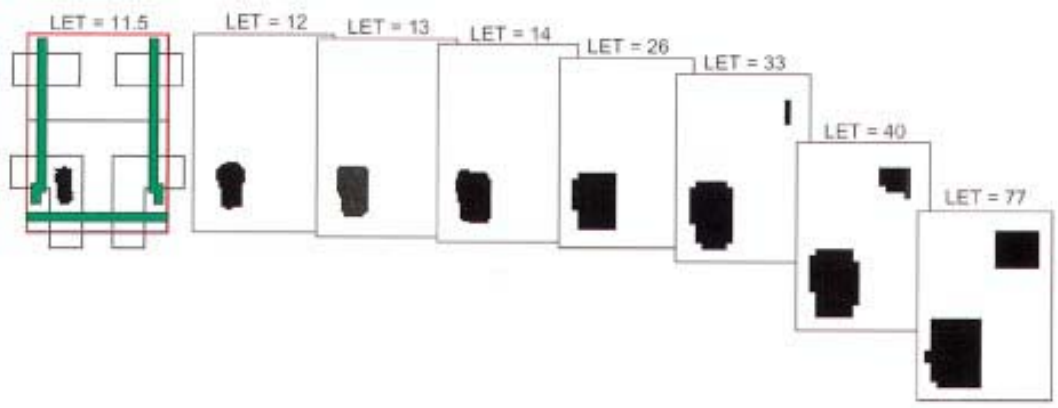

Fig. 4.6 Evolution of the soft-error sensitive area (black regions) of a 256 K SRAM unit cell as a function of increasing ion LET

As one can see from the picture, different parts of the circuit start begin to be sensitive at higher LET values, and only a few components are the cause of the radiation sensitivity of the cell. In a global irradiation experiment such a behavior would give rise to a double step Weibull cross-section curve.

The simulation results are impressive. However they require enormous computing time, even on a parallel supercomputer, and cannot represent a definitive verdict about the radiation hardness of a circuit, as they rely on the many assumptions necessary to implement a computable physical model.

To perform a direct validation of a such a rich simulation it is necessary to use an experimental system that is capable of registering both the effect and the position of impinging ions with a spatial resolution compatible with the feature size of the device under test. To provide validation of the Da Vinci simulations at the level of individual memory cells (fig. 4.5), REM experiments were performed at the heavy ion microprobe facility on the EN tandem Van de Graaff at Sandia.

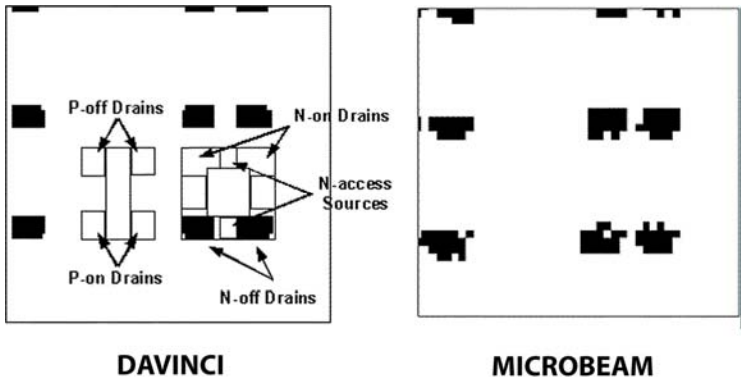

Fig. 4.7 SEU image of several unit cells in a TA788 16 K SRAM obtained with 35 MeV chlorine ions using a heavy ion microprobe and equivalent simulated SEU map for 35MeV chlorine ions.

In addition to the soft-error sensitive region for a given ion/energy combination, the simulations gives the transient currents in the SRAM cell as a function of ion strike location. By integrating the current over time it is possible to compute the total charge collection as a function of ion strike location in an externally accessible contact. Comparing the simulated charge–collection images to experimentally measured calibrated IBICC images obtained from the heavy ion microprobe, is helpful to further validate the accuracy of the simulations. Fig. 4.6 shows a 20-MeV carbon–ion calibrated IBICC image of several unit cells of the TA788 16 K SRAM, along with the simulated charge collection. 20-MeV carbon ions have an LET of 6 MeV-cm /mg, below the upset threshold.

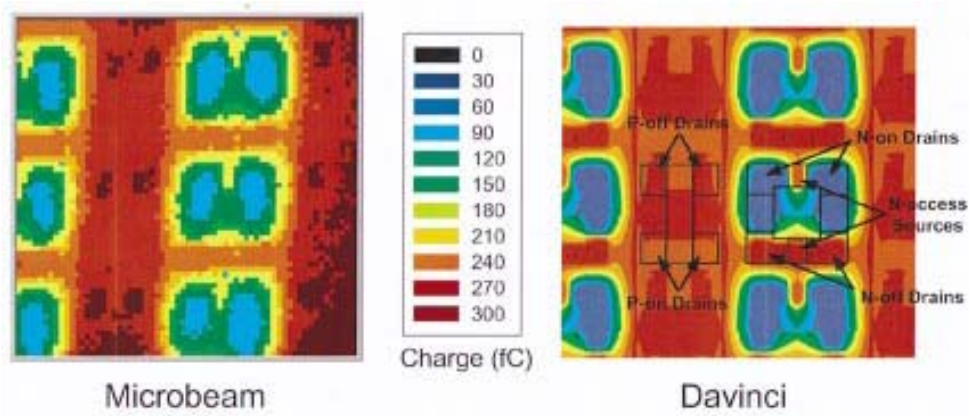

Fig. 4.8 Left: calibrated IBICC image of several unit cells in a TA788 16 K bulk SRAM obtained with 20 MeV carbon ions using a focused ion microbeam. Right: equivalent simulated charge–collection map for 20-MeV carbon ions. The color scales for both maps are the same and indicate total charge collection measured at the power supply.

The simulated and measured IBICC images generally agree to within about 20–30%. The validation experiments shown here indicate that mixed-level device/circuit simulation tools such as Da Vinci are well suited to SEU modeling of bulk CMOS SRAMs.

4.4 Microbeam techniques

4.4.1 Introduction

A microbeam allows one to precisely probe SEE sensitive areas of a device. In addition the amount of ion beam induced charge collected at specific locations on the integrated circuit can be measured and the depth of charge collection of the device can be calculated. These microprobe techniques, when coupled together, give a detailed picture of the mechanisms responsible for SEE that is impossible to obtain by other means. Microbeam techniques are also essential for transient charge collection measurements to ensure that signal arises from only the region of interest. When coupled with modem simulation tools, a complete picture of SEE emerges.

In the following paragraph we will discuss the main ways to implement microbeam techniques.

4.4.2 Microbeam apparatus

Two techniques are used to obtain heavy-ion microbeams.

The first approach consists in a placing a diaphragm with a pin-hole aperture between the sample and a heavy-ion source (such as an accelerator) and collimating the ion beam to a diameter of a few micrometers. The test sample, and in some cases the aperture, is positioned on an *x-y* stage to move the microbeam to a specific region of the device. Aperture sizes that can be used range from tens of μm down to about 2.5 μm. Micro-collimator systems based on glass tube micro-capillaries have also been used with radioactive alpha sources, such as a polonium tipped wire.

A significant fraction of beam particles interact with the edge material of the aperture and produce a wide spatial and energy distribution of background particles (beam halo) that will affect the analysis. This limits the achievable spot size of micro-collimator systems to about 2 μm (as distance of the aperture and the sample is on the order of 0.5 cm). The beam halo increases with increasing atomic number and energy. Secondly a micro-collimator system cannot be scanned rapidly. In addition the beam current falls rapidly with diameter. This is problem if high statistics experiments are to be performed on low sensitivity devices. All these limit the effectiveness of the micro-collimator technique for studying feature sizes smaller than a micron.

The second technique performs magnetic micro-focusing of the beam, and the scanning of the regions of interest on the device is achieved either by a electrostatic or magnetic means. A schematic of a magnetically focused system is shown in fig. 4.7. The beam optics is represented by a *lens*. In practice a microbeam facility will include: pre-slits, a magnetic beam switch, microslits, antiscattering slits, a beam scanning (rastering) system, a magnetic beam deflector, a lens diaphragm, the lens (a system of magnetic quadrupoles, usually a triplet), an optical microscope, and finally the sample stage. The optical microscope helps to aim the beam onto the target. In addition one might include

an ion impact detection system to certify the arrival of an ion on the targeted position. This can be done by detecting the secondary electrons emitted from the target surface when impacted by the ion. Finally the vibrations must be reduced to acceptable levels. Vibrating pumps (turbo and cryopumps) are coupled to the microscope chamber via soft bellows and vibration free pumps (ion pumps) are used along the beamline between the microslits and the lens. In some facilities the microprobe is isolated from vibrations from the floor by air springs.

To date, various microbeam facilities exist with different performances (e.g. beam spot sizes, ions species and energies). For SEE studies the most important facilities are:

- the heavy ion microbeam of GSI (Darmstadt, Germany). The linear accelerator UNILAC delivers ions from C to Ur with energies between 1.4 MeV/nucleon to 11.4 MeV/nucleon. It has been operational since 1987 and beam spot sizes of 0.5 μm are routinely achieved [51];
- the more recent microbeam at the SNAKE facility (Munich, Germany). The accelerator is a 14 MV tandem and delivers ions, from 20 MeV protons to 200 MeV Au. Beam spots of 0.5 μm have been achieved [52];
- The microbeam at TIARA (Takasaki, Japan). The accelerator is the JAERI AVF cyclotron accelerates heavy ions (up to Ur) with energies up to 27.5 MeV/nucleon. The energy spread of the accelerator has been greatly reduced recently allowing the microbeam to achieve spot sizes better than 1μm [53].

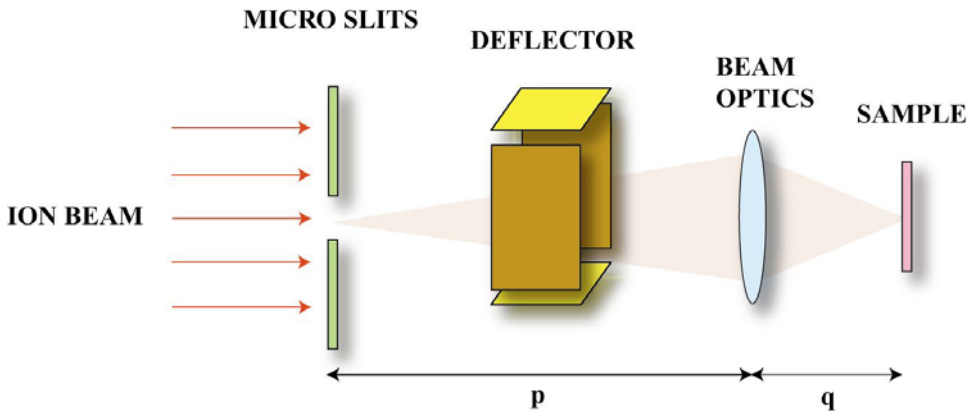

Fig. 4.9 **A schematic of a magnetically focused scanned microbeam system.**

As shown in fig. 4.7, the beam spot on the target plane is the transmitted image of the aperture slit. The electrostatic/magnetic lenses of the beam-optics produces a demagnified image of the slit on the focal plane. For a simple lens, the magnification ratio is given, to first order, by the ratio *q/p*. The demagnification of the beam size performed by the lens allows one to work with a large slit aperture, giving a higher beam current and a sharper energy distribution of the focused particles. By means of electrostatic deflection, it is easy to rapidly scan the focused beam across the sample.

Charged particles are accelerated, steered and focused using a combination of electrostatic and magnetic fields. The deflection of a beam passing through a uniform magnetic field *B* of length *l* (*Bl* in Tesla metres) is

$$\sin\theta = \frac{3.48Bl}{\sqrt{\left(EA/Q^2\right)}} \qquad (4.12)$$

while the deflection of a beam passing through a uniform electrostatic field *V/d* (Vm^{-1}) of length *l* metres is

$$\tan\theta = \frac{5\cdot 10^{-7} VQl}{d\cdot E} \qquad (4.13)$$

where A is the particle mass, Q is its charge and energy E is expressed in MeV. The much higher effectiveness of magnetic bending in curving high energetic particles makes it the most used way to bend ion beams.

The usual way to focus MeV ions is through quadrupole lenses (fig. 4.8).

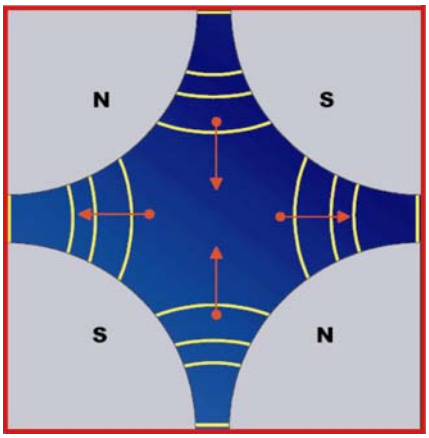

Fig. 4.10 Quadrupole lens schematic. Beam direction is toward the page.

A magnetic quadruple consists in four poles arranged symmetrically about the beam axis generating a hyperbolic field profile normal to particle motion axis. In the illustrated configuration the field is normal respect to the beam axis, so ensuring strong force applied toward the axis, a fundamental condition to allow beam focusing. Note that this kind of lens focuses the beam along one axis while it defocuses the beam along the orthogonal one: this means that to focus the beam in both axis at least two carefully matched quadrupoles are needed (doublet configuration). To get submicron beam focusing (high demagnification ratio), at present both triplet (“Oxford”) and quadruplet (“Russian”) multi lens system are used (fig. 4.9).

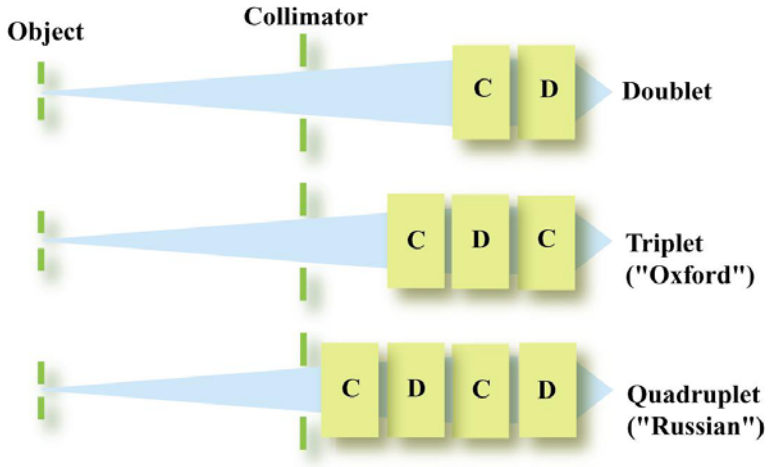

Fig. 4.11 Common microbeam lenses configurations.

At present the best performances for a microbeam (in term of resolution) belongs to the group of F. Watt at the University of Singapore [54]: using an Oxford OM-2000 triplet, a 3 MeV proton beam is focused down to a spot of 300 nm by 400 nm in size. This is truly an impressive result, but it is practically of no interest in the field of Radiation Effects Microscopy as it is difficult to maintain similar levels of performance with high mass high energy ions. No significant improvements in spatial resolution have been reported in over 5 years. To understand the reason of this stagnation, we need to consider the main causes that set a limit to the practical resolution obtainable with a microbeam.

Several factors limit the final resolution in a microbeam system, i.e. the beam spot size on the target. Some of them are engineering issues and presumably it would be possible to solve them. They span from mechanical stability (vibrations, long term drift due to thermal changes, for instance) to stray magnetic fields. Also scattering from residual gas in vacuum can contribute to worsen the resolution.

On the other hand two main issues are directly related to microbeam systems. First, a microbeam works by projecting a demagnified image of an object, the slit aperture. When the beam passes through the slit, particles that interact with the edge are scattered and arrive to the optical system with different energies and direction with respect to an ideal, parallel and monochromatic beam (fig. 4.10).

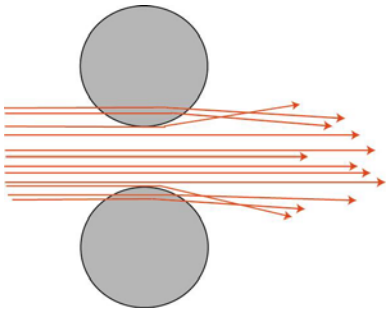

Fig. 4.12 Ions scattering due to interaction with slits

Lenses can correctly focus only particles with energy and direction inside a narrow spread around specific values, so scattered particles are poorly focused by the optics and form a halo around the ideally focused beam spot, decreasing the final resolution. In tab.

4.2 we report the ratio of scattered ions versus direct ions for different ranges and slit apertures.

	Slit aperture (μm)	
Range (μm)	20	1
60	0.060	1.2
10	0.002	0.033

Tab. 4.2 Ratio of scattered beam versus direct beam

As one can see from the table, for ions with a range of 60 μm in the slit metal, the ratio of scattered ions versus direct ions goes from 0.06 for a 20 μm aperture to 1.2 for a 1μm aperture. This means that there is a lower limit on the minimum usable aperture size set by the increasing aberration due to scattering phenomena, and this limit sets the smallest available beam size on target, as the demagnification is a fixed parameter of the design.

To improve resolution, the common approach is to adopt high demagnification systems, usually employing more sophisticated optics or multi stage systems (fig. 4.13).

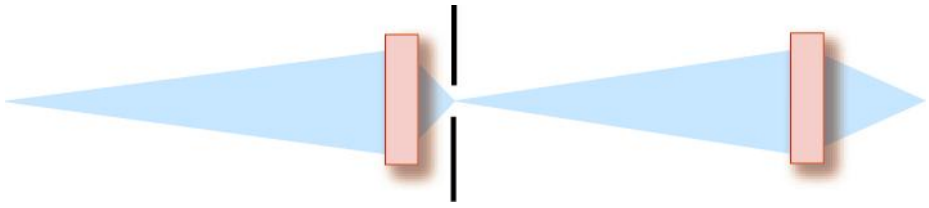

Fig. 4.13 Schematic of a multi-stage system

This configuration provides for an aperture at the intermediate image plane which removes the halo from the slit scatter. The high overall demagnification allows a large object aperture and, as the final stage can have long working distance, it helps design of target chamber.

It is important to note that, in principle, higher demagnifications should allow one to use larger object slits, but in practice they are not because it usually means higher aberrations.

The second major issue is that microbeams, like all optical systems, suffer from aberrations due to the lenses themselves. These aberrations may be divided into two main categories: geometrical and chromatic. Aberrations blur and deform the ideal focused spot so degrading the overall system resolution.

Geometrical aberrations are generated by imperfections of the optical system: e.g. the field shape is not exactly hyperbolic; the yokes are not perfectly aligned with the beam; the power supply exhibits ripples that affect the uniformity of fields in time, and so on. An improved engineering and/or more sophisticated optical design can greatly reduce the effects of this kind of aberration. Instead, differently from geometrical aberrations, chromatic aberration is an intrinsic behavior of any lens, and cannot be corrected by improving lens manufacturing. The only way to significantly reduce chromatic aberration is to implement a multi-lens design where the net chromatic aberration is removed by mutual cancellations between lenses. While such an approach is common in conventional optical system, at present ion beam optics technology cannot provide an equivalent solution. Hence, the only practical way to keep chromatic aberration under control is to have an extremely monochromatic beam: the particle beam energy spread must be as small as possible and the mean beam energy value must remains constant over time. As high-energy accelerators of heavy ions with monochromatic beams are hard to obtain, this is by far the most important intrinsic limitation in using a microbeam to perform Radiation Effects Microscopy. The production of the microbeam with a spot size as small as 1μm by quadrupole lenses requires the energy spread of the beam $\Delta E/E < 0.02\%$. Even in the case of an ideally monochromatic beam, strong magnetic lenses are required to bend heavy and energetic ions necessary for SEE testing.

At present, the best results in focusing down to micron size heavy energetic ions were obtained by the microbeam at the SNAKE tandem ($\Delta E/E < 0.01\%$) that uses superconducting focusing quadrupoles. They have focused 100 MeV ^{16}O down to a spot diameter of 500 nm [55] and lateral resolutions as low as Δx=600 nm and Δy=150 nm have been reported.

Recent important progress has been made at the AVF cyclotron of TIARA. The energy spread in the cyclotron beam depends on a waveform of the acceleration voltage

and beam phase acceptance of the cyclotron. The typical energy spread of the cyclotron beam is around 0.1% in the ordinary acceleration mode using a sinusoidal voltage waveform. Recently the energy spread was successfully reduced to allow for submicron beam spots by superimposing a fifth-harmonic voltage waveform on the fundamental one to generate a flat-top waveform for uniform energy gain.

4.4.3 REM limits

The main limitation of microbeam is the difficulty to work with energetic heavy ions necessary for SEE sensitivity measurements. In addition, as new circuits grow in complexity, the direct irradiation of the front surface of a device becomes more difficult to do because of the presence of structures and several micron thick layers of metallization for surface electrical contacts (fig. 4.12 a) that can affect the beam before it reaches the sensible nodes of the circuit.

In the case of ASICs or R&D test structures, it is generally possible to obtain tailor-made samples especially conceived for REM investigations. But for the growing majority of standard production devices (COTS) a similar procedure is clearly not possible.[1] The dense layers and superstructure will clearly degrade the energy of the impacting heavy ion. This is an important problem when one considers that not all SEE depend only on the charge induced in the thin (~1 μm) active layer of the device. For instance a SEL involves the collection of charge from depths extending for several micrometers and it is generally considered appropriate to test for SEL using ions for which the range in silicon is at least about twice the epitaxial layer thickness. Nonetheless, space agencies (NASA, ESA) require dedicated validation measurements with greater range ions to remove all doubts about SEL rate test. These considerations exemplify the importance of developing irradiation facilities at ion accelerators at even higher energies.

A feasible approach for SEE irradiation at higher energy ion accelerators consists in irradiating the sample from the backside thereby avoiding all the surface structures on the top side. This technique requires a back-thinning procedure to reduce as much as possible

[1] In any case the plastic case should be removed.

the thickness of the silicon substrate (fig. 4.12 b). Anyway it requires that the ions travel through the substrate for several tens of microns (~50 μm, in the example) before reaching the sensible structures on the front surface of the device.

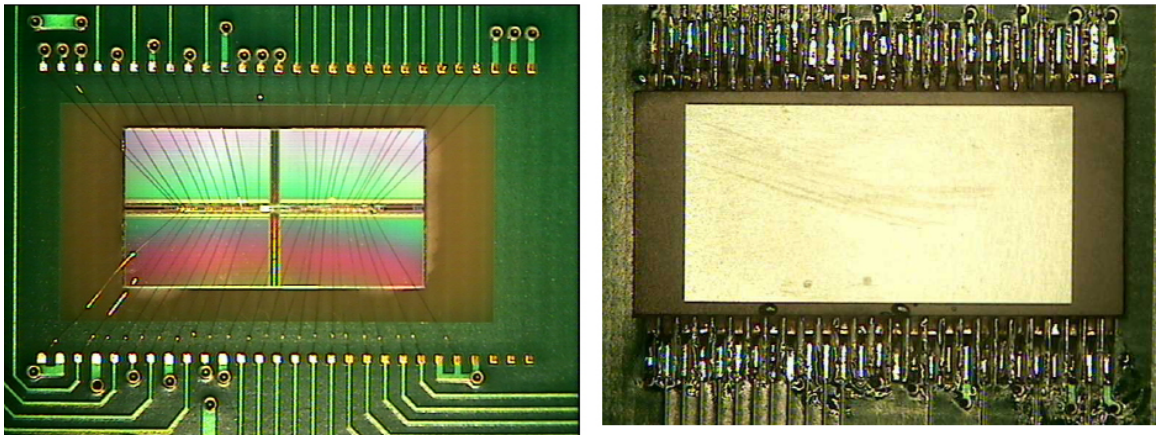

Fig. 4.14 Hyunday 256-Mbit SDRAM, front side (a) and back-thinned sample (b) (Courtesy of ESA)

This trend, requiring high range, hence high energy heavy ions, is difficult with microbeams for two reasons. First, as already stated, it is difficult to focus heavy energetic ions. Second, to accelerate ions to even higher energies requires accelerating machines different from electrostatic accelerators such as Tandems that are the most suitable for microbeams. Microbeams are used in combination with electrostatic accelerators because they provide the highly monochromatic and stable beam necessary for the microbeam optics to achieve micron resolutions. In table 4.1 we list the typical ion species and energies deliverable by a big electrostatic accelerator (15 MV Tandem of the INFN Legnaro National Laboratory). The values listed well represent the practical upper limit to the energies obtainable by such kind of machines. Note that for LET values higher than 20 MeV×cm^2/mg (^{48}Ti at 196 MeV) the ion range in silicon falls under 40 μm, a value that is considered a lower limit to allow performing backside device irradiation.

To obtain higher range heavy ions for future state-of-the-art SEE testing requires using a different type of accelerator system, such as using RFQ boosters at the exit of an electrostatic accelerator, cyclotrons or even more complex accelerator systems. Cyclotron accelerators and boosting systems, while able to deliver heavy ions with higher energies,

even higher than 1 GeV, do not ensure the beam monochromaticity and stability necessary for microbeam systems.

For SEE testing there is at present the need to ensure good resolutions for very energetic (high range) ions over a very wide range of heavy ion species (high Z for high LET). It is important to note that the feature size of state-of-the-art electronics is less than 100nm, more than a factor three smaller than the very best microbeams. It unlikely that microbeam resolutions will improve much. On the other hand electronic technology continues to evolve and feature sizes continue to shrink.[2] No foreseeable microbeam design will ever reach comparable resolutions.

We conclude that present REM techniques are severely limited when evaluated in terms of present and certainly future requirements for SEE testing with heavy ions with high LET and large range values. This is the reason for the necessity to investigate a new approach to Radiation Effect Microscopy, that we are going to describe in the following chapter.

[2] The feature size of present technology is already comparable to the lateral spread of the ions due to multiple scattering in the metallization layers ~10μm.

5. Ion Electron Emission Microscopy

5.1 A novel approach

5.1.1 Introduction

A possible alternative to the traditional microbeam technique is Ion Electron Emission Microscopy. It was first proposed in 1999 and developed by the group of B. L. Doyle at SANDIA National Laboratory [56].

This approach discards the need for precisely focused and scanned ion beams and uses instead a broad (non-focused) beam (fig. 5.1).

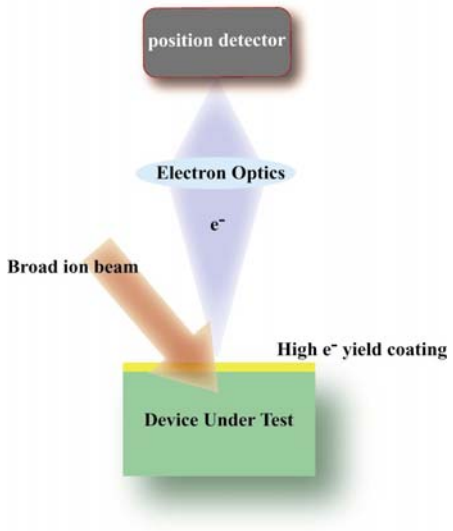

Fig. 5.1 Schematic of IEEM technique

Instead of relying upon the scanning system to know where the ion beam spot is at the time a radiation effect is detected, the IEEM technique precisely images the position of the secondary electrons emitted from the surface of the target as a result of single ion impacts. The secondary electrons are collected by a series of electrostatic lenses and the

magnified secondary electron image of the target surface is projected onto a focal plane. To reconstruct the impact points of the impinging ions the electron emission image points of the hit surface are imaged by coupling the electron emission microscope to a fast two-dimensional position detector that gives the spatial coordinates of the impacting ion with micrometric resolution. The detector time-resolves individual ion hits in the field of view of the microscope up to impact rates of several kHz. The timing of the emissions of secondary electrons at the mapped positions on the sample surface is correlated with the ion-induced signals from the device or material sample under test to match a particular ion interaction to a particular place on the sample.

5.1.2 Sandia IEEM system

The very first IEEM system was installed on a nuclear microprobe line of a 6 MV Tandem accelerator located at Sandia National Laboratories in Albuquerque, N.Mex. The accelerator coupled to RFQ linac booster delivers energetic heavy ion beams, such as 53 MeV ^{28}Si, 241 MeV ^{127}I and 374 MeV ^{197}Au. In the first configuration, the Sandia IEEM was in non axial configuration. The present configuration is axial: the ions pass down through the IEEM to impact the target surface normally. For this purpose the fast high resolution position detector is annular. The electron emission microscope is a commercial Photon Electron Emission Microscope (PEEM) [57]; the annular detector is also commercial but was developed for IEEM applications.

5.1.3 Secondary electron emission – generalities

The physical mechanism at the basis of Ion Electron Emission Microscopy is the emission of secondary electrons from the target surface as a consequence of an ion strike. The average number of secondary electrons emitted for each impact depends on the interaction of that particular ion with the target surface and is an important parameter for an IEEM since it sets the efficiency of this technology [56].

According to the theory of Sternglass, the physics of secondary electron production involves three stages:

1. *formation of secondary electrons*: the energy lost by fast ions is given up in two types of collision processes: elastic collisions where low energy (1÷20 eV) secondary electrons are produced; inelastic collisions that give rise to energetic knock-on electrons (δ rays) which, in turn, produce secondaries that may then produce tertiaries, and so on, in higher order collisions. Although the number of δ rays is very small, the total energy going into their formation approximately equals that going into the direct formation of slow secondaries at high ion velocities;
2. *secondaries diffusion*: low energy secondaries move by diffusion through the medium. Elastic collisions involve small amount of energy transfer to the thermal vibrational modes of the lattice and it takes on the average only a few collisions (2÷5) to reduce the energy of a secondary below the minimum value necessary to overcome the surface barrier potential. Considering that the mean free path between collisions in metal is approximately of the order of a nanometer, escaping secondary electrons are only those produced at shallow depths in the target, about 1÷5 nm below the surface;
3. *emission* into vacuum by overcoming the surface barrier, which is the surface dipole potential, originated by the asymmetry in the electron charge cloud of the surface atoms projecting outward beyond the positive charges of the ion core.

According to Sternglass theory [58], the electron yield Y (i.e. the average number of secondary electrons able to escape from the surface for ion impact) is:

$$Y = P\frac{\lambda}{\cos\theta}\frac{LET_0}{W} \tag{5.1}$$

where λ is the Mean Free Path (MFP) for electron scattering, θ is the beam's angle of incidence, W is the ion energy required to ionize an electron in the medium, P is the probability for an electron to escape the surface potential barrier and LET_0 is the value of the LET of the ion at the surface of the target. The emission depth is thought to be very

shallow (1÷5 nm) for metals but much larger for insulators [59] and has a cosine angular distribution [60] (fig. 5.2): the maximum number of secondary electrons is emitted along the surface normal (Φ = 0°).

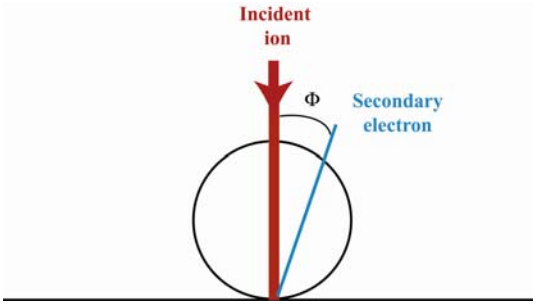

Fig. 5.2 Angular distribution of secondary electrons emitted by the target surface for normal impact.

The energy distribution of the secondary electrons is peaked at a few eV, and the shape of this distribution is independent of ion species and energy. The LET parameter is here assumed to be constant (equal to LET_0) due to the fact that the very few nanometers under the surface, where secondary electrons are produced, is a small depth compared to the range of energetic incident ions. As a result, to a very good approximation, one may consider the emitted secondary electrons to have originated in at a depth in which the incident ions still possess their original energy. The amount of energy lost per unit path length which is available for secondary electron formation may accordingly be taken as constant throughout this region.

Equation (5.1) can be contracted in the following form by grouping all medium-dependent parameters:

$$Y = \Lambda \frac{LET_0}{\cos\theta} \tag{5.2}$$

The Λ parameter represents the medium respect to ion induced secondary electron emission and ranges, for smooth metal surfaces. The value is reported to range between 0.07 and 0.13 Å /eV (in the nergy range from 80 keV to 1 MeV [61]. This value can be significantly reduced by surface structures/defects that perturb the electric field uniformity.

The most important approximation made in (5.2) was to assume the extraction work to be independent from the ionization track generated by the ions: while this is a good approximation for lighter ions (protons), ionization becomes relevant for heavy ions. As a consequence of the strong ionization of heavy ions, the secondary electron yield is significantly diminished and the Λ parameter is not a constant but it depends on the ion species and energy [59].

While the above picture is a good approximation for metals, matters are quite different in the case of insulators where slow electrons cannot lose their energy by elastic collisions with conduction electrons and this results in an increased free mean path. The increased path length and the inelastic collisions that characterize the transport of electrons in semiconductor/insulator make the path of the secondaries much more complicated than that described in conductors. Moreover in semiconductors and insulators the medium ionization is a threshold process, where the ion energy loss per interaction is higher that the small amount we found in conductors. In addition charge-accumulation effects increase the surface potential barrier. For these reasons the emission yield for semiconductors and insulators is greatly reduced, if not absent at all. This is of great importance as many semiconductors devices present protective passivated layers (SiO_2) on their surface, making them potentially unsuitable for the IEEM technique unless their surfaces are first suitably treated.

Measurements performed by the Doyle group observed no emission from the passivated surface of a PIN diode [56]. This indicates the need to perform some kind of surface preparation in the case of a non-emitting sample. This preparation should provide a sufficiently high secondary electron yield to allow the IEEM to detect ion impacts with reasonable efficiency.

We note that the low mean energy of emitted electrons and energy spread are important factors for electron emission microscopy as they affect the final resolution.

5.2 Electrons imaging

5.2.1 Imaging electrons

The field of electron emission microscopy is approximately 40 years old and has been reviewed by several authors, most recently by Griffith and Engel [62]. Emission microscopy in general is a direct imaging technique. In other words, the image is not formed by scanning a beam or sequential composition, but by collecting all the information from the electrons over the whole field of view and in real time, two features that are shared by IEEM.

Electron emission from surface can be induced in various ways: thermally, via excitation by photon irradiation or electron/ion bombardment or by field emission. Among the wide range of possibilities offered by the electron microscopy, Photon Electron Emission Microscopy (PEEM), which uses electrons extracted from UV photons to image the sample surface, is suitable to be used as off-the-shelf technology to implement Ion Electron Emission Microscopy. Therefore the imaging core of an IEEM is a commercial PEEM microscope (fig.5.3).

A variety of contrast generating mechanisms contribute to distinguish surface features on a submicron scale. The small energy of the electrons used to form the image (~ 1eV) accounts for the surface sensitivity of the PEEM: contrasting techniques are used to study slight variations of electron energy due to surface features. Contrast techniques are not applicable for IEEM: the secondary electrons emitted by ion impact are more energetic electrons (~ 5eV) and less sensitive to surface imperfections. Indeed the different purpose of IEEM is to provide a measurement of the impact position of an ion and to this end the SE average yield is the main consideration. In an IEEM experiment the ideal situation is obtained when the yield is high and constant across the sample for uniform ion detection.

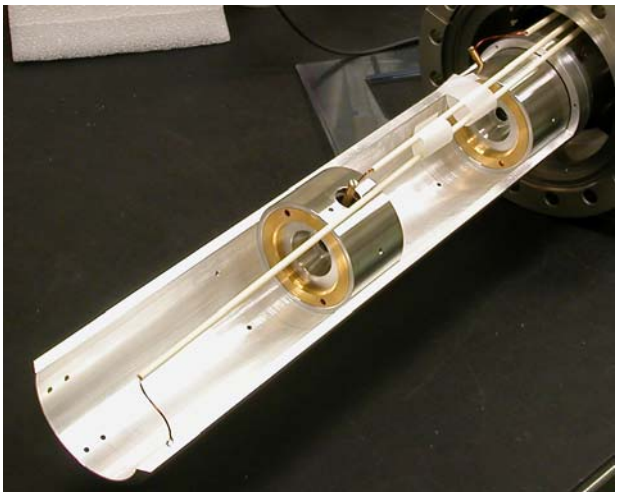

Fig. 5.3 PEEM column with lenses.

The electron optical column of the microscope is formed by several electrostatic elements shown in fig. 5.4: the objective lens, the zoom lens, two projective lenses and finally the X Y position sensitive detector (PSD).

The magnification ranges from 160× to 1600× (when projector A is not used, the magnification increases to 8000×) which corresponds to a field of view between 250 and 25 µm. The magnification is set by adjustments to the zoom lens, focusing is performed with the objective lens, and projector B is adjusted so that the field of view fills the PSD.

The sample surface itself is part of the objective lens. This lens is basically an immersion lens formed by four electrodes (a tetrode lens): the sample surface and a three electrode lens (fig. 5.5).

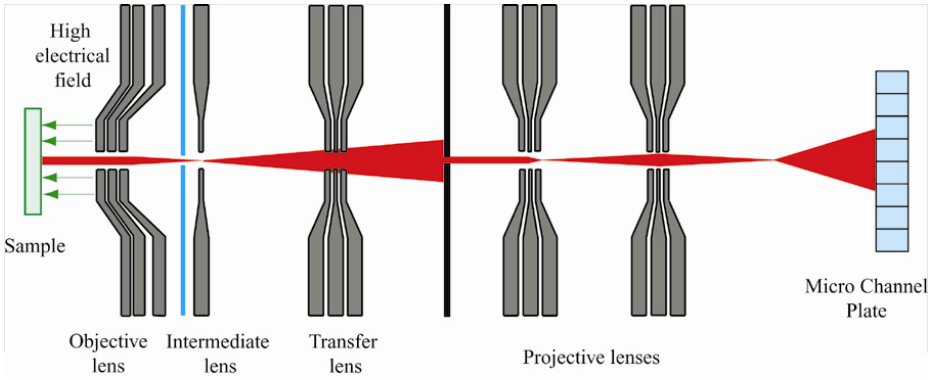

Fig. 5.4 Schematic diagram of the PEEM lenses system.

An accelerating field of the order of several kilovolts per millimeter is applied between the sample and the first element of the lens (transfer voltage). The field strength and its uniformity are a key figure to determine the best lateral resolution. Keeping the sample at ground or at least near ground potential simplifies handling and current measurements; however, it also requires that the whole column is at the transfer potential (up to 15 kV in our case) with the sample positioned at a distance of a few (3÷5) millimeters from the first lens element, allowing a maximum field strength of ~5 kV/mm.

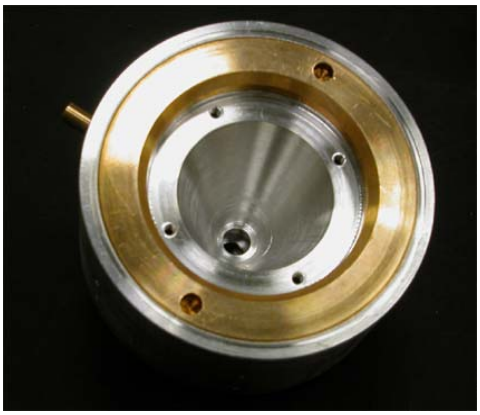

Fig. 5.5 Objective immersion lens.

The homogeneous electric field between the sample and the first lens electrode accelerates the electrons and forms a virtual image below the sample surface. The three electrode lens forms a magnified real image behind the objective lens.

The zoom and two projector lenses account for the final magnification on the image detector. An aperture in the source plane of the projector B limits the field of view. This aperture is useful to limit the area of the sample where SEs are produced and also to protect other areas from ion induced damage (particularly important for testing semiconductor electronic circuits) but is not needed in many cases. The zoom lens is used to set the total magnification. Two imaging modes are accessible; a low magnification mode and a high magnification mode. High magnification mode means a high field strength in the zoom lens. In this mode, the objective lens forms a real magnified image in front of the zoom lens, which is further magnified onto the aperture of projector lens B.

Low magnification mode means a low field strength in the zoom lens. In this case, there is no real but only a virtual intermediate image formed. Switching between the imaging modes accounts for a flip in the observed image.

A further lens (decelerating lens) with a separate power supply placed after the last projective lens can decelerate electrons down to ~1 keV to optimize the performances of the electron amplifier (usually a Micro-Channel Plate, MCP) placed on the microscope focal plane. This lens can be excluded if required.

5.2.2 Resolution

Like any other "optical" instruments, the PEEM microscope presents problems of distortion and aberration. Distortion causes an information modification (geometrical distortion), but not its complete and definitive loss or degradation: as information is only changed, a subsequent image analysis can restore it to its original appearance. On the contrary, aberrations lower the resolving power of the instrument and lead to an unrecoverable loss of spatial information.

A secondary electron will be extracted and it will enter the PEEM column with a starting angle to be transported to the focal plane. The spread in energy and emission angle of the secondary electrons will introduce aberrations; i.e. electrons following non-ideal trajectories will not be focused and the image will blur. Spherical aberrations will not occur along the optical axis of the system, while they increase when the starting angle of the electrons diverges respect to the optical axis. By using a high electric field strength at the surface most electrons will be transferred into the PEEM column, even those electrons emitted up to nearly 90°. On the other hand the energy spread of the secondary electrons leads to energy-dependent trajectories (chromatic aberration). The easiest way to limit both spherical and chromatic aberrations is to put a diaphragm with an aperture that cuts electrons with improper trajectories. A small aperture will select small starting angles and small energies, but the transmission efficiency (the fraction of secondary electrons accepted by the PEEM) is reduced. A good lateral resolution can only be achieved with a small contrast aperture and a high extraction voltage.

The PEEM was designed and tested to work with electrons generated by UV photons, that exhibit a low energy mean value (1 eV) and a narrow energy distribution (1 eV FWHM); using a PEEM to image more energetic and less monochromatic electrons generated by ion impacts will affect the resolving power.

In order to get a quantitative estimation of the PEEM resolution when used as an IEEM, the Sandia team, in collaboration with the PEEM manufacturer, performed a ray-tracing calculation of the theoretical resolution (for chromatic aberrations only) and transmission efficiency versus aperture size [56].

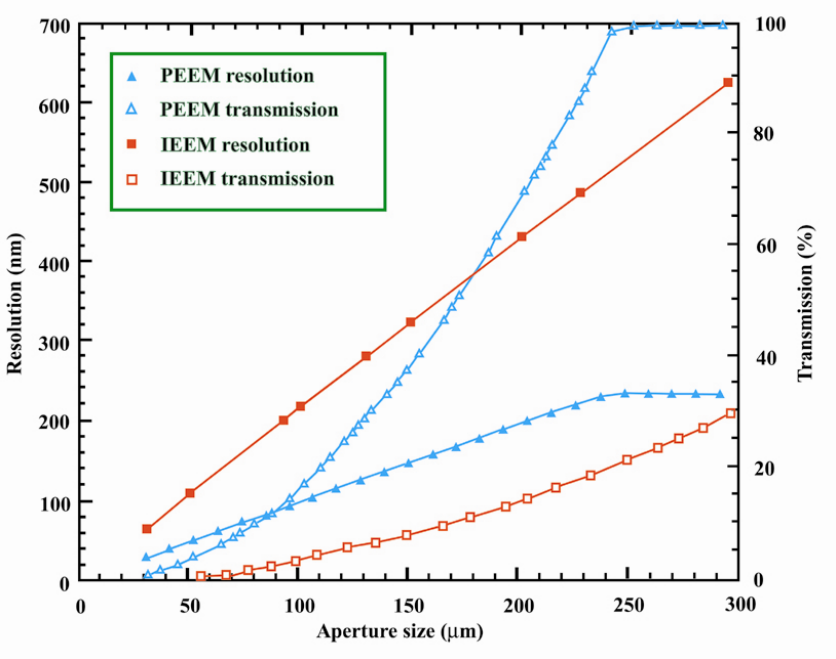

Fig. 5.6 Efficiency and resolution as a function of the diameter of the aperture of the contrast diaphragm of the PEEM for both photon induced secondary electrons and high energy ion induced secondary electrons, assuming electron mean energies of 1eV and 5eV respectively.

For these calculations the energy distribution of secondary electrons at the sample was assumed to be peaked at 5eV with a 5eV FWHM and to be emitted with a cosine angular distribution. With these assumptions the intrinsic resolution of the IEEM is ~500 linear resolved points (lrp); i.e. it is possible to distinguish 500 equally spaced points lined up along the diameter of the field of view (FOV). Using the largest 300μm aperture, to maximize electron transmission and hence ion detection, the IEEM resolution is ~0.6 μm

and the transmission efficiency is ~30% (fig. 5.6). With the 300μm aperture the PEEM is 100% efficiency with a resolution of ~0.2 μm (the intrinsic resolution of the PEEM is ~1500 lrp). For the IEEM to achieve a 0.2 μm resolution would require a ~100 μm aperture but the transmission efficiency would be only ~2÷3%.

5.2.3 Electron detector

For each ion impact, a number of electrons are emitted but only a fraction of them get transmitted by the microscope column. An electron multiplier is placed on the focal plane of the microscope to make a robust electronic signal. This detector must not degrade the intrinsic spatial resolution of PEEM and must have a refresh rate fast enough to sustain a useful rate of ion impacts in the microscope field of view.

The commonly chosen detector for this kind of application is a multi stack Microchannel plate (MCP). A microchannel plate is an array of miniature electron multiplier oriented parallel to one another. Typical channel diameter are in the range of 5-100μm and have length to diameter ratios (α) between 40 and 100. Channels are typically normal to, or biased at a small angle (~8°) to the MCP input surface. The channel matrix is usually fabricated from a lead glass, treated in such a way as to optimize the secondary emission characteristics of each channel and to render the channel walls semiconducting so as to allow charge replenishment from an external voltage source (fig. 5.7). Each microchannel is a continuous-dynode electron multiplier, in which the multiplication takes place under the presence of a strong electric field. A particle or photon that enters one of the channels through a small orifice is guaranteed to hit the wall of the channel due to the angle of impact. The impact starts a cascade of electrons that propagates through the channel, which amplifies the original signal by several orders of magnitude (10^4-10^7) depending on the electric field strength and the geometry of the micro-channel plate. After the cascade, the microchannel takes time to recover (or recharge) before it can detect another signal. MCPs show excellent time resolution (< 100ps) and a spatial resolution limited only by the channel dimensions and spacing. Detection efficiency of a microchannel plate depends upon the type, energy and angle of incidence of the primary

radiation and the first strike conversion of the microchannel plate. Under common operating conditions, the detection efficiency is limited by the open area ratio (channel area/ total plat area), since events striking the inter-channel area are not typically collected. The open area ratio for standard MCPs ranges between 55-85%.

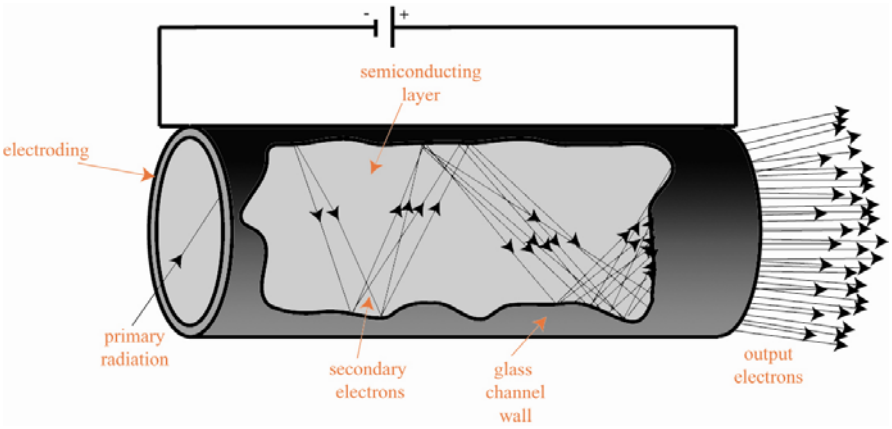

Fig. 5.7 A channel electron multiplier.

The typical working voltage is ~1kV, corresponding to a gain of about 10^4. Higher gains (up to 10^9) can be achieved by coupling two or more into stacks. In imaging applications it is usual to express the spatial (lateral) resolution of an instrument in line pairs per millimeters (lp/mm). For a single high resolution MCP the limiting resolution is 40 lp/mm; for a two stack (chevron) it is better than 25 lp/mm; for a three stack (Z-Stack) high gain assembly it drops to 16 lp/mm. Still higher gain solutions (5 plates stack) further drop the resolution performance. MCP sizes (the diameter of the circular active area) are standard, and the most common are 18 mm, 25 mm and 40 mm and the choice of the proper sensor size depends on the resolution requested by the specific application.

In paragraph 5.2.2 we expressed the resolving power of the IEEM in terms of lrp (the maximum number of distinguishable points lined up along the diameter of the field of view). When resolution is stated in lp/mm, the width of the line, i.e. the size of smallest resolvable feature, is equal to 2 × resolution expressed in lp/mm. As an example we consider a large diameter three stack MCP assembly. The resolution of a such a detector is better than 16 line pairs (lp)/mm. For a detector with a diameter of 40mm, this corresponds to a resolution better than (2 × 16 lp/mm) × 40 mm = 1280 lrp across the

diameter. Such a detector will not degrade the IEEM intrinsic resolving power (~500 lrp). It must be noticed that this is also true for a smaller MCP diameter of 25 mm which will have a resolution better than 800 lrp. However in UV-mode the intrinsic resolution of the PEEM is three times better than when used as an IEEM (see fig. 5.6) and the 25 mm diameter MCP assembly would be inadequate for PEEM applications.

For IEEM applications, an MCP is used in high gain (saturation) mode, i.e. the output signal strength is only weakly dependent on the number of incoming electrons. This feature is useful to discriminate real events against dark counts from thermally generated electrons (typically of the order of ~ 0.5cts/s/cm^2 and increasing with the gain factor). In fact, electrons thermally generated in the second stack will have an output signal significantly weaker than real events. Of course, if electrons are thermally generated in the first stack, the discrimination will be nearly impossible, as their output signal will be comparable with the one from a real ion impact.

JEFF: In fact, electrons thermally generated inside the chevron MCP have an output signal significantly weaker than real events. Of course, for electrons thermally generated near the input of the first stack, the discrimination will be nearly impossible, as their output signal will be comparable with the one from a real ion impact.

Saturation is also a desirable condition because it ensures a stable output, which does not depend too much on the statistic of secondary electron emission, their transport through PEEM column and the MCP amplification factor. This stable output makes easier the coupling with a Position Sensitive Detector (PSD) device.

The time resolution of an MCP is related to the avalanche evolution time, and is of the order of few ns for a multi-plate stack. The avalanche electronic signal, thanks to its prompt response to events, should be hence the ideal candidate to provide (unless noise-pickup problems) a fast trigger signals.

5.2.4 Position sensitive detector and readout

Besides secondary electrons detection (task performed by the microchannel plate), also position recording (2-D imaging capability) and time resolution for the coincidence function and time-of-flight based measurement are critical for the IEEM technique.

In Sandia IEEM, the X Y position detector consists of a charge-division position encoder (resistive anode encoder, RAE) directly coupled to the microchannel plate. This position sensitive detector (PSD) was manufactured by Quantar Technologies [63] and a schematic of this detector is shown in fig. 5.8.

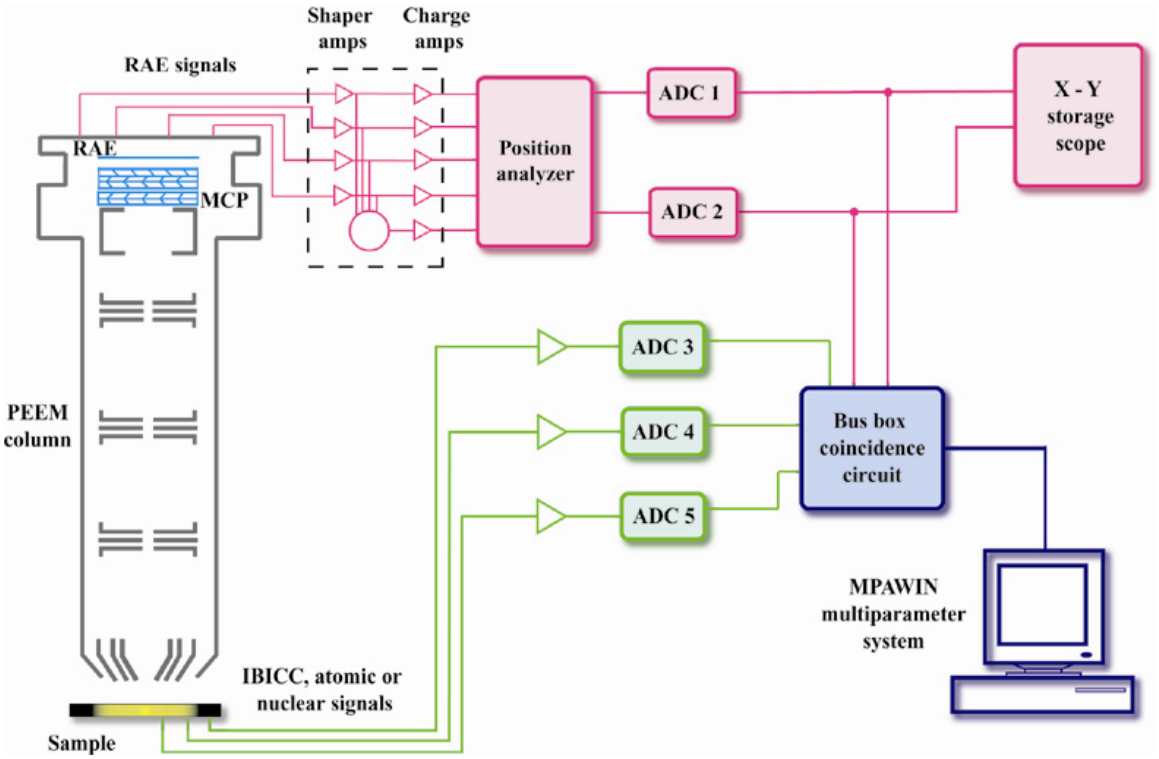

Fig. 5.8 Schematic drawing of the various elements of Sandia IEEM.

The MCP configuration used ensured the high electron gain (~ 2×10^7) required for high position resolution (400 line pairs) while maintaining a tight gain pulse-height distribution for single electron initiated events. With the highest PEEM gain (1600×) the field of view is 25 µm and resolution the PSD can ensure a resolution at the sample of 25µm/400 = 0.06 µm.

In operations, electrons impact the MCP surface located at the final image plate of the PEEM. This results in an electron cascade that is multiplied by the MCP to a measurable level and the resulting electron cloud is electrostatically focused onto the surface of the RAE encoder. The charge diffusing in the RAE is divided among four collection terminals in a ratio proportional to position in the X and Y axes. The output is fed to a four channel charge sensitive amplifier/shaper module. From the ratio of the preamplifier output signals, the readout electronics (the Position Analyzer in fig. 5.7) computes the X and Y positions of each event (the Position Analyzer returns analog pulses the amplitude of which are proportional to the positions). In addition, the position analyzer contains discriminators and pulse-pile-up circuits to veto events that are too low or high in gain, or arrive too close together, to be properly imaged. The X Y analog outputs are then connected to the external ADCs used in a multiparameter data acquisition system and to a conventional analog variable persistence X-Y oscilloscope to display real time secondary electrons images. The system has a relatively high instantaneous dynamic counting range extending from the low counts rate of the MCP background (10 cps) up to 2.5×10^5 detected events/sec, corresponding to 4 μs dead time per event. This recovery time, set by the RC constant of the sensor itself and by the shaping time of readout electronic, puts a limit on IEEM capability of distinguishing ion impacts: only events separated by an temporal interval larger than the recovery time can be distinguished. Keeping in mind that ion strikes follow a Poisson statistic, the maximum sustainable ion rate is 2.5×10^4 impacts/sec in the FOV of the microscope. For a FOV of 250 μm this maximum rate corresponds to a particle flux of 5×10^7 ions/cm^2·s. Such a value is orders of magnitude faster than typical ion rates employed in SEE experiments. An example could be helpful in clarifying this statement. Let us assume to irradiate an area of a device corresponding to the IEEM physical aperture. For a FOV with a 250 μm diameter, the exposed area is ~ 5×10^{-4} cm^2. The number of SEEs for second is given by the ion impact rate times the fraction of the FOV area that is SEE sensitive. Assuming that the number of memory cells in the FOV is 10^4 and a SEE cross section of 10^{-9} cm^2 /bit, the average SEE rate of a SEE event every 50 ion impacts in the FOV. At the the maximum RAE particle rate of 2.5×10^4 ions/s in the IEEM FOV, and would correspond to ~500 SEE per second, a rate

which is typically too high for testing complex memory arrays. In addition, devices exposed to ion impacts suffer from Total Ionizing Dose (TID) effects and one must limit the accumulated ion fluence to prevent excessive radiation damage.

The 100ps FWHM time resolution for the PSD is obtained by an auxiliary pickoff circuit which senses the time-of-passage of the single event through the MCP.

The detector X and Y outputs are digitized and fed to two inputs of an 8 parameters MPA/PC multiparameter system, which captures the digital data for X, those for Y and the energy parameters obtained from the separate detectors. In addition, the data system offers full time-coincidence capability between parameters, so events are accepted only if they fall into defined time ranges on each parameter. The data collected are only those whose PEEM and ion-beam induce charge collection (IBICC) detector are in coincidence.

6. IEEM at SIRAD

6.1 The SIRAD irradiation facility

6.1.1 Introduction

An original IEEM system was proposed by our group [64] and is now working at the SIRAD irradiation facility located at the Tandem accelerator of Laboratori Nazionali di Legnaro, Padova. In this chapter, after giving a detailed description of SIRAD facility, I will examine closely our implementation of ion electron emission microscopy.

6.1.2 The Tandem XTU accelerator

The Tandem-XTU accelerator at the INFN National Laboratory of Legnaro is an electrostatic Van de Graaff type (fig. 6.1): two stripper stations are used in order to achieve high ion energies.

Fig. 6.1 The 15MV Tandem XTU at the INFN Legnaro National Laboratories.

Table 6.1 reports typical ion species and energies available at SIRAD. Normally, the extracted beam is continuous but pulsed beams are also possible. The maximum operating voltage is 15 MV and available ions range from ^{1}H (30 MeV) to ^{197}Au (1.4 MeV/a.m.u.). The energy, expressed in MeV, of the ions at the exit of the Tandem with two strippers is:

$$(6.1) \quad E = E_{inj} + V_0 \cdot (1 + q_1 \cdot f + q_2 \cdot (1 - f)) \tag{6.1}$$

where E_{Inj} = 0.18 MeV is the energy of the negative charged ion injected from the source into the Tandem, V_0 = 11÷15 MV is the Tandem operating voltage, f = 0.25, and q_1 is the positive charge of the ion expressed in units of the electron charge after the first stripper foil located at the terminal. The charge $q_2 > q_1$ is the ion charge after the second stripper foil located downstream of the first one. The second stripper foil can be excluded, in which case the energy of the ions is

$$(6.2) \quad E = E_{inj} + V_0 \cdot (1 + q_1). \tag{6.2}$$

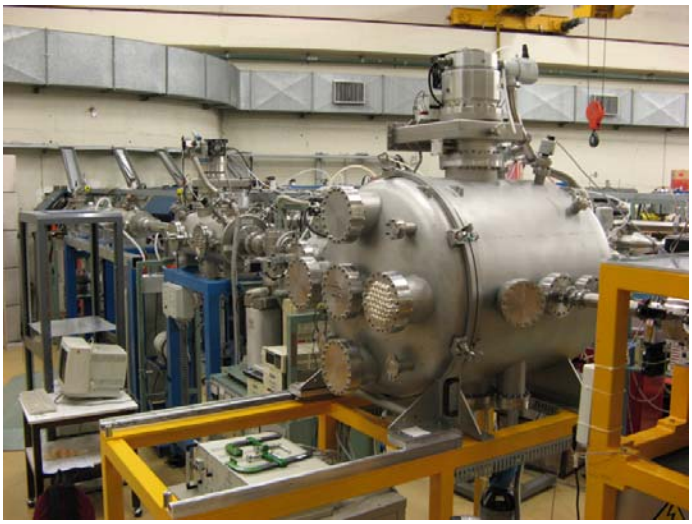

Fig. 6.2 Picture of the SIRAD irradiation facility at INFN Laboratori Nazionali di Legnaro.

The beam at the Tandem output is not monochromatic due to the realization of different q_1 and q_2 ion charge states. Magnetic momentum analysis selects ions of only

energy and the switching magnet then sends the monochromatic beam into the various experimental beam lines. The Tandem-XTU accelerator services 3 experimental halls and 10 beam lines: the SIRAD beam line is the +70° in the heavily shielded hall 1, as shown in fig. 6.2.

6.1.3 The SIRAD irradiation facility

Bulk damage and SEE studies are routinely addressed at the SIRAD irradiation facility of the INFN National Laboratory of Legnaro (Padova, Italy) by Universities and Industrial groups, involved in the study of the radiation hardness of semiconductor devices and electronic systems for high energy physics and space applications [65].

The characteristics of the typical ion beams available at the SIRAD irradiation facility are reported in Table 6.1: the energy values refer to the most probable q_1 and q_2 charge state, obtained with two stripper stations and with the Tandem operating at 14 MV, the surface ion LET and range in silicon (calculated by SRIM). At present when using ^{197}Au beams in SIRAD the operating voltage is typically lowered to 11.6 MV due to a temporary limitation in the maximum current in the power supply of the switching magnet that deviates the beam into the line at 70°.[1] The ion species reported in Table 6.1 have been selected in order to minimize the time required for the ion source change during SEE tests. When possible two multi-sources (the first including O, Si, Ni and Ag; the second including F, Cl, Br, and I) are used to decrease the time for beam setting.

[1] We plan to remove all limitations of this type by stripping further electrons from the ions just before the analyzing magnet.

Ion	Energy (MeV)	q_1	q_2	LET (MeV × $cm^2/\mu g$)	Range (μm)
^{1}H	28	1	1	0.02	4390
^{7}Li	56	3	3	0.37	378
^{11}B	80	4	5	1.01	195
^{12}C	94	5	6	1.49	171
^{16}O	108	6	7	2.84	109
^{19}F	122	7	8	3.87	99.3
^{28}Si	157	8	11	8.59	61.5
^{32}S	171	9	12	10.1	54.4
^{35}Cl	171	9	12	12.5	49.1
^{48}Ti	196	10	14	19.8	39.3
^{51}V	196	10	14	21.4	37.1
^{58}Ni	220	11	16	28.4	33.7
^{63}Cu	220	11	16	30.5	33.0
^{74}Ge	231	11	17	35.1	31.8
^{79}Br	241	11	18	38.6	31.3
^{107}Ag	266	12	20	54.7	27.6
^{127}I	276	12	21	61.8	27.9
$^{197}Au^{2}$	275	13	26	81.7	23.4

Tab. 6.1 Characteristics of the typical ion beams available at the SIRAD irradiation facility with the Tandem operating at 14 MV.

The essential elements of the SIRAD line, shown in fig. 6.3, are:

- a system of adjustable horizontal and vertical slits;
- a quadrupole doublet for focusing the beam down to millimetric spots;
- an electric rastering system for irradiating extended targets;
- an irradiation chamber with a vertical sample-holder, available both for diagnostic and irradiation purpose;
- a chamber with an extractable Faraday cup (FC70);
- an irradiation chamber including a battery of small Faraday cups and a battery of silicon diodes with pulse counting electronics.

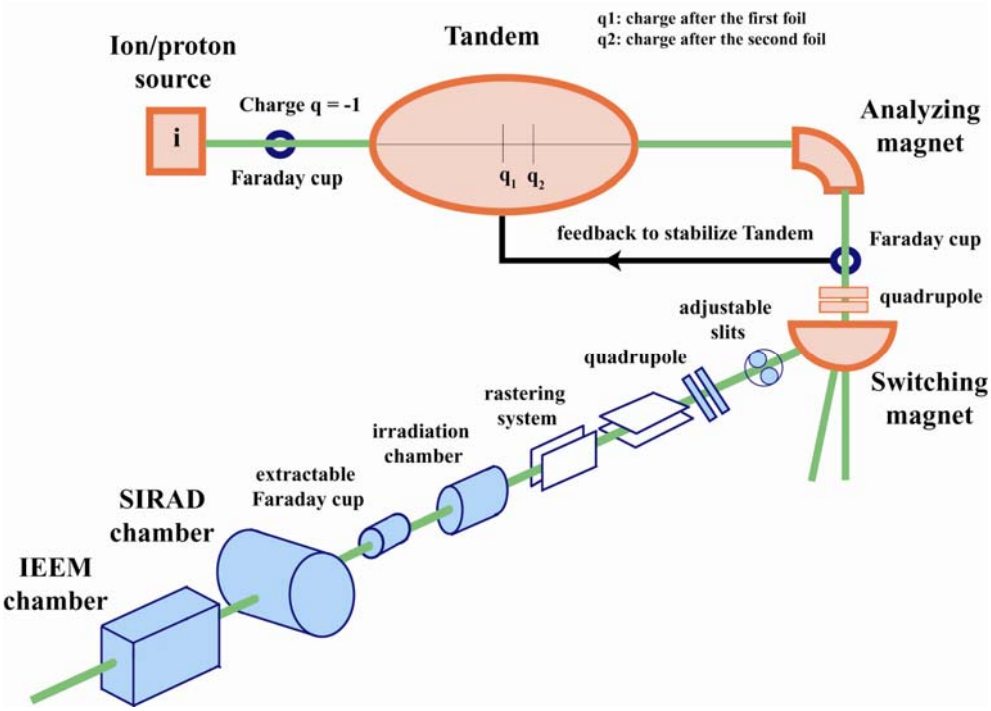

Fig. 6.3 Schematic drawing of the SIRAD irradiation facility.

The typical spot size diameter of a focused beam is 3-4 mm and beam diagnostics is performed by an extractable Faraday Cup positioned in a diagnostic chamber located ~ 1 m upstream of the target plane. Visual inspection of the beam profile may be performed on a quartz window positioned at the end of the irradiation chamber.

In order to irradiate a large target with a focused proton or ion beam, a rastering system is used. The system, produced by IBA (Louvain-la-Neuve, Belgium), is made of vertical and horizontal deflection plates 1 m long, with 5 cm gaps, and with linearly ramped voltages (V_{max} = ±15 kV) at slightly different frequencies (ν_x = 625 Hz, ν_y = 612 Hz). The rastering system permits a uniform irradiation (better than 5%) over a fiducial area of 5×5 cm^2 on the target plane. On-line monitoring of the beam current and uniformity on the target is provided by a square battery of 3×3 small Faraday cups, located behind the target plane (sample holder). This configuration is suitable for radiation tests at beam currents higher than 100 pA/cm^2 and is currently used for proton induced bulk damage studies in silicon.

The low ion fluxes (10^2-10^5 ions/(cm^2·s)) necessary for SEE studies in electronic devices and systems are obtained by closing machine collimators to achieve low beam currents (< 1 nA) and by defocusing the beam on the target plane by adjusting the SIRAD quadrupole doublet (see fig. 6.1). The quadrupole doublet is positioned before the rastering system, which normally is not used in defocused beam irradiations. The ion fluxes for SEE tests are below the sensitivity of the Faraday cups and are consequently monitored by a different system, consisting of a battery of silicon diodes, used as particles counters, in the target plane.

6.2 Ion Electron Emission Microscope at SIRAD

6.2.1 General description

The Ion Electron Emission Microscope installed at SIRAD irradiation facility shares a several characteristics with the one at SANDIA, to benefit of the R&D activity already performed. First of all, we use the same commercial PEEM for imaging electrons. However, ours has a fixed smaller contrast diaphragm of 200 μm diameter, which lowers the transmission efficiency, but the achievable resolution is better, with an improvement of almost a factor 2 (0.4 nm, see fig. 5.5).[2]

The efficiency of an IEEM relies on a high electron yield per ion impact of the surface under study and an adequate secondary electron emission should be hence ensured. Normally the surface of a semiconductor device under test (DUT) is a poor electron emitter. In addition the efficiency of electron collection and transport through the microscope can be altered by any target surface roughness. A straightforward approach we use is to place an ultra-thin free-standing gold flat membrane on top of the DUT. This

[2] It is worth mentioning that the more expensive commercial PEEMs by Omicron (www.omicron.de) allow one to select contrast diaphragm of different apertures allowing one to tailor optimize the resolution according to the ion species: heavier ions with many secondary electrons could afford smaller higher resolution apertures.

approach ensures adequate secondary electron emission and near independence from the DUT and will be discussed in great detail in the next chapter.

We too started in an off-axis configuration, where the ion beam hit the target with an inclination of 75° respect to the normal. First tests were performed and the first images of ion-induced secondary electrons were recorded. We then moved to the axial configuration where the ion beam passes down through the MCP and along the microscope lenses and strikes the sample orthogonally (fig. 6.4). This configuration is the optimal one for Ion Electron Emission Microscopy because both it solves the parallax problem due to the lateral displacement from the impact position along the ion path inside the target and because it takes advantage of the full ion range in the sample. On the other hand, the axial configuration requires annular detectors and a fine beam alignment, because ions have to pass through the small contrast diaphragm.

Differently from SANDIA, the position detector of the SIRAD IEEM doesn't directly detect the electron avalanches at the output of the MCP output (which acts as an electron multiplier), but it detects flashes of light from a phosphor screen coupled directly to the output of the MCP. The avalanche electrons from the MCP, initiated by the secondary electrons from a single ion, impact excite a phosphor screen that emits a burst of photons [66]. These are reflected by a 45° mirror and extracted from the vacuum chamber a quartz window and focused onto an external image intensifier. The regenerated light signal is finally focused onto a custom-made, digital, high rate and high resolution position sensitive detector, which detects the photons and returns the x and y coordinate of the original ion impact. The device is connected to the control PC via an USB connection and has no need of any further external hardware.

A remote controlled sample holder, with five degrees of freedom (three linear motorized stages (2.5 mm travel range) and an additional angular module with a tip-tilt stage (9° of maximum inclination) to align the target surface and the PEEM focal plane, allows target positioning with a resolution of 0.01μm with a repositioning error better than 0.1μm [67] and is suited for high vacuum (down to 1×10^{-7} mbar).

The same computer controls the proprietary data acquisition system, the DC motor stage, the dosimetry software and the vacuum logger, without the need of other external electronic module.

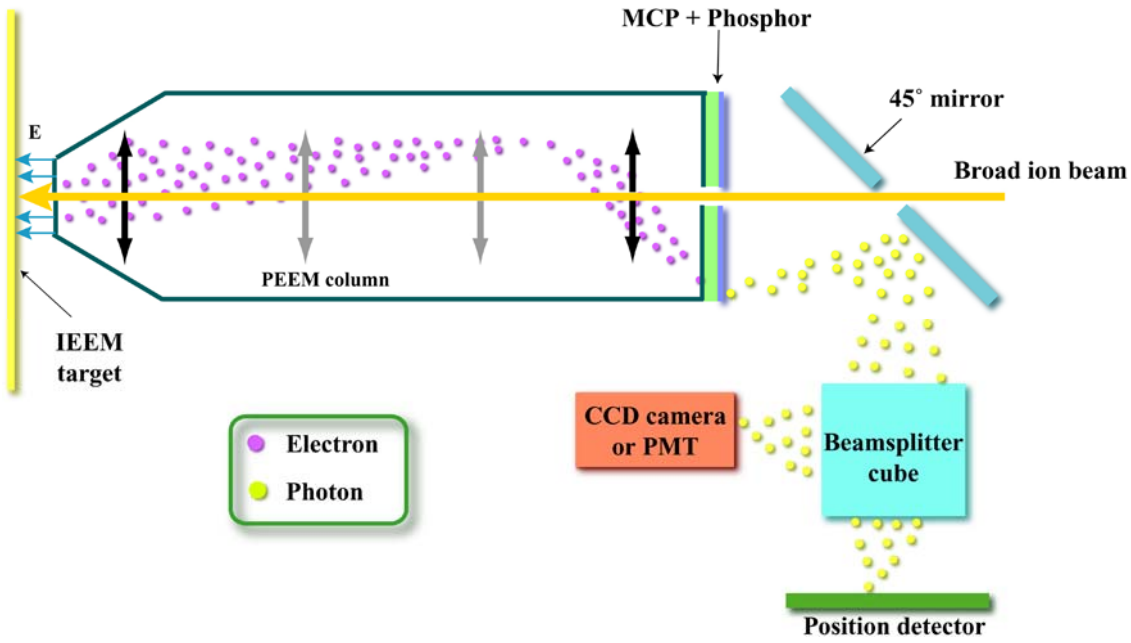

Fig. 6.4 Schematic drawing of SIRAD IEEM setup.

6.2.2 The irradiation chamber

The change to the axial setup required a new and tailor-made irradiation chamber (fig. 6.5). The design is based on the previously gained experience in the off-axis configuration. The chamber has a box-liked shape and a whole side opens like a large drawer allowing easy access to the target, to the 5 axis sample holder and to ancillary electronics (if any). The entire sample holder and every item inside the chamber are mounted on the sliding floor of the drawer. Thus, by opening the chamber everything inside slides out completely from the chamber providing tabletop-like working conditions.

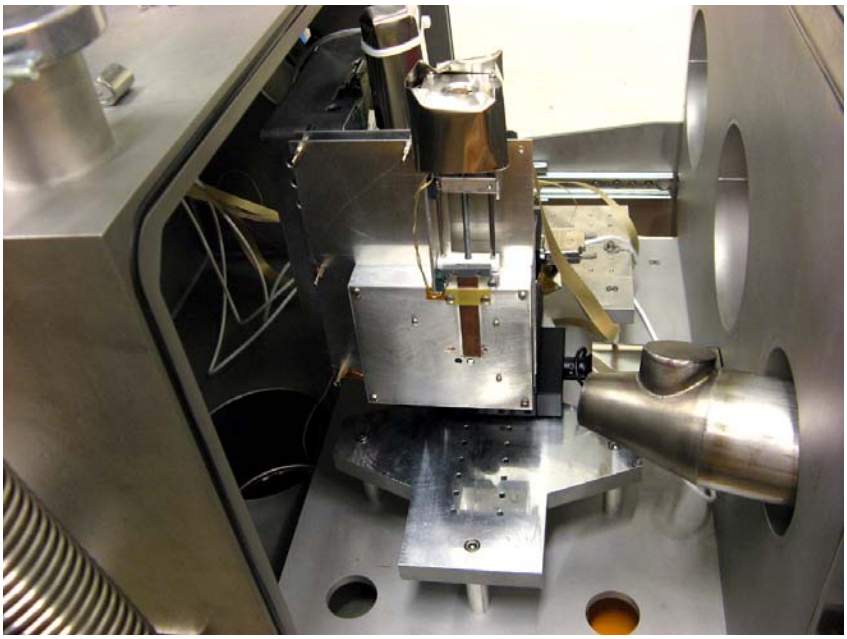

Fig. 6.5 **View of a target mounted on the sample holder with linear DC motor stages inside the extracted drawer of SIRAD IEEM irradiation chamber.**

The relatively small volume of the chamber (70 × 40 × 50 cm of dimensions) allows reaching the operational vacuum level (~1 × 10^{-6} mbar) in a reasonable amount of time. The chamber provides enough space to host ancillary electronics that might have to be kept ad close as possible to the target DUT.

Two DN160CF flanges with D-style multi-pin connectors (one with 8 × 15 sub-D type feedthrough and one 2 × 50 sub-D type feedthrough) allows a wide possibility of connections between the vacuum chamber and any external setup (DC motor controllers, beam diagnostic, sample DAQ, etc.) In case of need, it is possible to add flanges with special connections without changing anything in the setup by means of the user serviceable flanges.

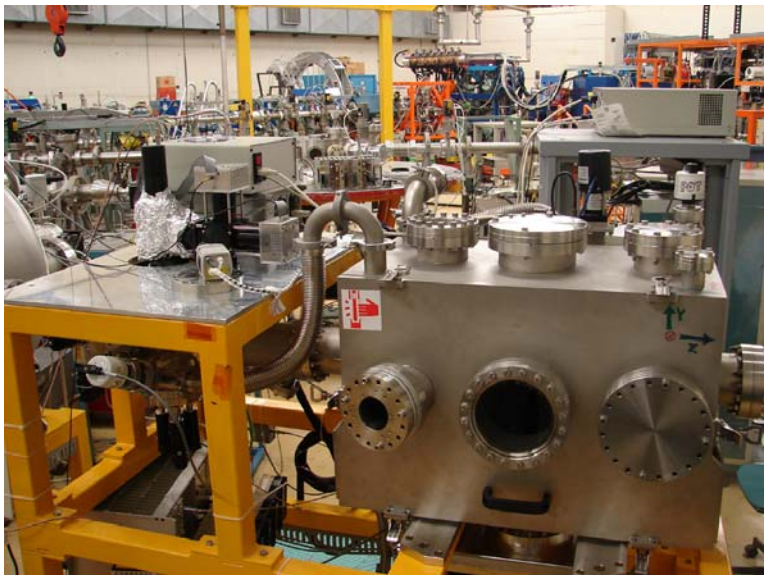

Fig. 6.6 View of axial SIRAD IEEM chamber and setup.

Two flanges are oriented 75° respect to the PEEM axis and aim at the target plane. One of these hosts a quartz viewport for a UV lamp. Before the experiment, preliminary calibrations and tests are in fact performed using UV photons, to help alignment and fine focusing of the PEEM.

The other 75° flange hosts an optical microscope system (fig. 6.7), a module that was intended to allow sample inspection and alignment. The 7× zoom provides a FOV ranging from 5.6 mm to 0.8 mm with a working distance of 90 mm. The big working distance allows keeping free the area around the sample, providing space for a quite big electronic board to be directly mounted on the sample holder. Lower magnification is used to broadly align the target, higher zoom ratio to perform a fine alignment procedure with the aid of a laser.

At present, the chamber is rigidly mounted on a fixed stand and the first tests and measurements shown in this thesis are performed with this setup (fig. 6.6). In addition, presently, the turbo pump is not decoupled from the chamber. One of the scheduled future upgrades will involve decoupling the IEEM from the SIRAD beam line and the floor of the experimental hall. Vibration stability is a point which should be under careful consideration as the vibration amplitude perpendicular to the optical axis of the microscope must be well below the desired resolution limit.

Fig. 6.7 Optical microscope assembly for target inspection and alignment.

6.2.3 Target alignment

A challenge for IEEM is the ability to correlate IEEM reconstructed ion events with the position of the target. For this reason, several robust and reliable target alignment procedures have been considered.

The first idea was to apply a recognizable mark on a surface on the sample holder inside the area approachable by the microscope (2.5 × 2.5 mm^2, through sample holder repositioning). The reference marker on the surface can be placed by direct metal deposition or masked sputtering, depending on the target surface, down to feature sizes of some microns. The relative position between the marker and the test target is optically measured with great accuracy before assembling the sample holder inside the IEEM chamber. When the reference mark has been centered into the IEEM FOV (either using UV photons or ions), the relation between the target position and IEEM reconstructed impact coordinates is found. The repeatability of submicron positioning, provided by the motorized stages, allows one to move the sample holder without losing this relationship. The exact area framed by the PEEM is found injecting a laser beam through the microscope by means of a small mirror which slides to close the central hole of the main 45° mirror.

Fig. 6.8 The standard DN100CF 6-way cross housing the annular MCP and the 45° mirror. On the bottom flange the manual micrometric actuators are shown, used for a correct positioning of the main holed mirror and for the insertion of the small one for alignment procedure.

The path through the microscope ensures the laser alignment with the microscope axis, and the 200 μm aperture cuts the laser beam to a diameter equal to the maximum FOV size.

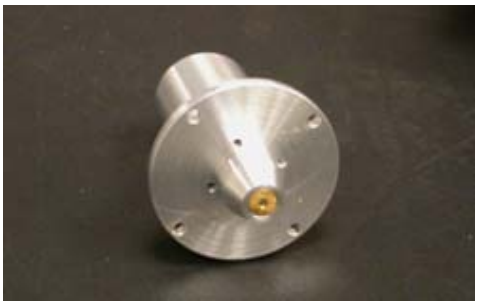

Fig. 6.9 Contrast diaphragm (200 μm diameter).

This arrangement allows one to watch the laser spot on the target by using the lateral optical microscope. The use of the laser bright spot as a marker for the IEEM FOV position eliminates the parallax error due to the lateral large angle of view of the optical microscope (75° respect to the microscope axis).

This solution, apparently simple, has several important drawbacks. As the viewing direction is very slanted respect to the normal of the sample surface, even this optical microscope, specially designed to provide a great depth of field (DOF), is not able to guarantee an in-focus view of the interested sample area. Besides, the laser injection from

outside the chamber through the 200 μm diaphragm is a hard task (for mechanical reasons) and the resulting spot is too faint for a robust measurement.

The simplest way to remove the problem is to move the optical microscope to a more suitable position with the optical column positioned parallel to the PEEM, so that it aims normally at the target. This would solve both the lack of depth of field and the parallax problem. The position of the target in front of the PEEM is found once the relative position between the marker and the target is known with precision. This solution offers the possibility to avoid the use of the laser and frees a viewport which could be used for other purposes. On the other hand, this approach implies modifying the chamber. As the present chamber was conceived to be kept as small as possible (to reduce pump-down time), at present there is no room in the chamber wall for the optical microscope.

6.3 Photons production and detection

6.3.1 Introduction

Differently from the solution adopted by the SANDIA group, we obtain the positions of the ion impacts by imaging light spots on the phosphor screen directly coupled to the MCP rather extracting them from the electron avalanches at the MCP output.

In our case the output electrons of the MCP are accelerated across a small gap (~ 1mm) and locally excites a phosphor screen; each output electron avalanches is converted to a blue light spot. An optical assembly, consisting of a 45° mirror (with a central hole) and a system of lenses, collects the photons from the luminous spots and extracts them outside the irradiation chamber where they are detected by a photon position-sensitive detector. This is a simple and relatively inexpensive (compared to the use of an expensive annular RAE), but the main drawback is that only a small fraction of the photons are collected (low optical efficiency). To regenerate the light signal, to allow for ease of detection, we use an external image intensifier, which amplifies the light signal by a factor 10^6. The light signal strength is now suitable to be revealed by the final position detector.

For position sensing applications the choice of sensors is very wide, but only few solutions have been investigated. The natural approach seems to be CCD or CMOS arrays as they offer up to mega-pixel level resolutions (our minimal requirement of 500 points on the image diameter is not an issue at all!) and the ability to work with very low light levels. The main drawback of these arrays is the need to readout the entire array to determine if and where the light-spot arrived and hence the difficulty of sustaining data throughputs useful for SEE applications. The proper sensor for IEEM applications must be searched for elsewhere.

The first solution we developed was an analog position sensitive device (PSD) working on the charge splitting principle [68]. Its performances were good respect to the capability of event rate handling, but the effective resolution was disappointing as it suffered from the high level of noise. Despite its limitations, this sensor was used for IEEM preliminary tests in non-axial configuration [69].

A completely new digital position sensitive detector system was then developed [70] [71] that provides the required high-rate and high-resolution performances. The system reduces the number of pixels to read and makes the digital approach feasible. It will be described in paragraph 6.3.4.

6.3.2 Photons production

A double stack MCP (40 mm large) with a central hole (8 mm diameter) has been chosen as the main electron detector. Working in saturation mode, this device ensures an amplification factor up to 1×10^7 e^-/e^-, with a dark count rate of ~ 0.5 counts /sec·cm^2, corresponding to less than 7 counts/sec on the entire area.

The 40 mm diameter phosphor screen, coupled to the MCP, converts the out-coming electron clouds into luminous spots. Among the available types of phosphors, the P47 (Y2SiO5:Ce,Tb) has been chosen, because its peak emission is at 400 nm, it has a fast decay time (from 90% to 10%) shorter than 100 ns with a tail decay time (from 10% to 1%) of 2.9 μs (table 6.2). The light signal is short enough to allow in the field of view of the IEEM ion impact rates well above those necessary for SEE applications. The

wavelength emission distribution of the chosen phosphor is roughly symmetric around 400 nm, hence, to estimate the maximum photon yield, we assume all the photons carry the same energy equal to:

$$(6.3)\quad E_{\gamma 400nm} = 3.1eV = 4.97 \cdot 10^{-19} J\ .$$

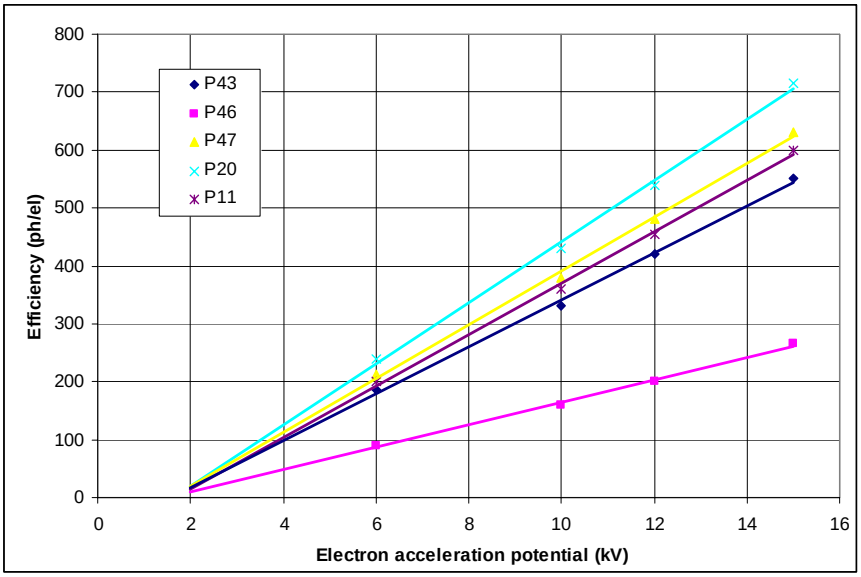

Fig. 6.10 Efficiency of phosphor screens expressed as the number of output photons for an incident electron.

Type	Composition	Light emission				Decay time	
		Range		Maximum	color	Decay of intensity	
		from	to	typically at		from 90% to 10% in	from 10% to 1% in
P 43	Gd_2O_2S:Tb	360 nm	680 nm	545 nm	green	1 ms	1.6 ms
P 46	$Y_3Al_5O_{12}$:Ce	490 nm	620 nm	530 nm	Yellow green	300 ns	90 µs
P 47	Y_2SiO_5:Ce,Tb	370 nm	480 nm	400 nm	Blue white	100 ns	2.9 µs
P 20	(Zn, Cd)S:Ag	470 nm	670 nm	550 nm	Yellow green	4 ms	55 ms
P 11	ZnS:Ag	400 nm	550 nm	450 nm	blue	3 ms	37 ms

Tab. 6.2 Spectral emission range and phosphor decay time.

The MCP focal plane detector we use ensures a resolution better than 25 lp/mm, equivalent to more than 2000 *lrp* over the 40 mm diameter. This is not degraded by the phosphor layer which, thanks to its micro-crystal structure, can give resolutions better than 100 lp/mm. A variable potential gap (0÷2kV) between the second plate of the MCP and the phosphor screen accelerates the electrons to increase the phosphor conversion efficiency (fig. 6.10). The corresponding conversion yield for 2keV electrons is ~50 γ/e^-. This value refers to a single electron impinging on the screen, but when a cloud of particles (up to 10^7 in a double stack MCP) reaches the phosphor, saturation phenomena may occur. Dedicated measurements were performed to get an indicative value of this parameter (γ_{sat}), as no specific data are present in literature [71]. Taking into account the area of the phosphor interested by the electron current (~ 200 μm diameter) and the duration of the current itself (2÷4 ns FWHM), the order of magnitude of the maximum outgoing number of photons for a single incoming electron can be expressed as:

$$(6.4)\quad \gamma_{yield} = \gamma_{sat} \cdot area \cdot time = \frac{100\gamma}{\mu m^2 ns}\left(\pi \cdot 100^2\right)\mu m^2 \cdot 3ns \approx 1 \cdot 10^7 \gamma \,.$$

6.3.3 Photons amplification

The light signal must be carried out of the vacuum chamber and focused onto the PSD system. A low-distortion system of lenses has been design to perform this task. Taking into account the transmission efficiency of this system (1%), the reflectance efficiency (95%) and the hole geometrical factor (6 mm diameter) of the 45° mirror to bend the photons, the final global optical transmission efficiency is reduced to:

$$(6.5)\quad \varepsilon_{opt} = 0.94\% \,.$$

Considering the phosphor screen photon yield (6.4) and the optical extraction efficiency (6.5), the signal outside the chamber available for the position measurement is reduced, for a single electron detected by the MCP, to:

$$(6.6)\quad 1\times10^{7}\gamma\times0.0094\approx1\times10^{5}\gamma\,.$$

A solid state detector works collecting the charge generated by the incident radiation. The conversion efficiency (sensitivity) of one sensor, i.e. the ratio between the incident radiation energy and the generated charge, remarkably varies across the spectrum (see fig. 6.11). A silicon device shows the conversion maximum for infrared radiation. For 400 nm photons, an indicative value of responsivity for a UV-enhanced device, especially designed to sense blue radiation, is about 0.15 pC/pJ (it can range from 0.12 pC/pJ up to 0.22 pC/pJ). The out-going photons from the optical system (6.6) can therefore generate in such a sensor a charge signal equal to:

$$(6.7)\quad 1\times10^{5}\gamma\cdot4.97\times10^{-19}J\cdot0.15\frac{pC}{pJ}\approx7\,fC\,.$$

This signal is of the same order of magnitude of Equivalent Noise Charge (ENC) of a charge splitting device such as the PSD, and it is one order of magnitude smaller than ENC of a typical pixel detector. Robust signal detection is nearly impossible for both kinds of devices (not considering here the speed problem for CCD systems). We solved this problem by adding an image intensifier, a device that amplifies the light signal to be detected by the final sensor.

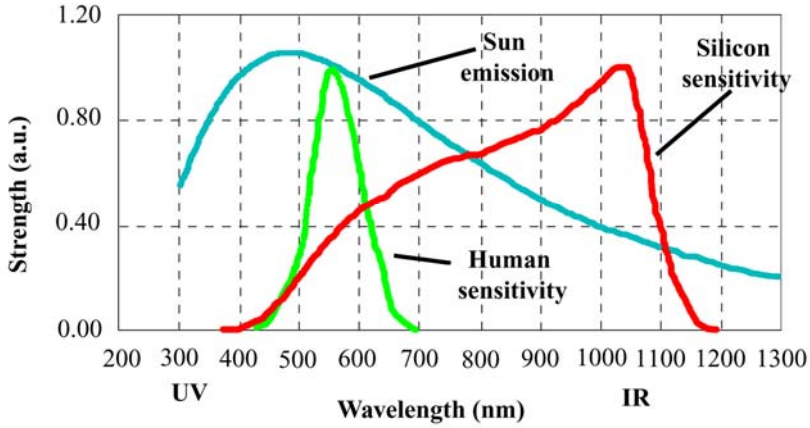

Fig. 6.11 Comparison between relative conversion efficiency for the human eye and for a silicon-based detector.

An image intensifier is *plug-and-play* device that is composed by a photocathode, an internal MCP and a phosphor screen, all items enclosed in an air-tight case. The image intensifier we use has a 2-stack MCP and a P47 phosphor screen [72]. However it has a 25 mm diameter and therefore the resolving power is 25 lp/mm × 25 mm = 625 lp = 1250 lrp. It meets the time and spatial resolution requirements for the whole system. Considering the number of photons arriving on the photocathode (6.7), the photocathode efficiency at 400nm (30%), the maximum gain (10^6 e^-/e^-), the acceptance factor (55%) and the phosphor yield (50 γ/e^- for the P47), the expected number of out-coming photons is naively expected to be

$$(6.8)\quad 1\times 10^5 \gamma \times 0.3\cdot 10^6 \times 0.55 \times 50 \approx 8\times 10^{11}\gamma\,.$$

The phosphors screen of the image intensifier also suffers from the saturation effect. Direct measurements were performed and indicate that the output of the image intensifier the photon yield can reach a value equal to:

$$(6.9)\quad \gamma_{II} \approx 10^{10}\gamma$$

This is to be considered the maximum photon yield that it is possible to obtain from a single electron impinging on the MCP placed at the focal plane of the PEEM.

To couple the image intensifier output with the final position sensor, additional optics is needed. The efficiency of this optics is of the order of few percent. Considering the maximum photon yield (6.9), the lenses efficiency (~ 2%) and the detector sensitivity (15%), the light level on the silicon sensor can be estimated to be

$$(6.10)\quad 10^{10}\gamma \cdot 4.97\times 10^{-7}\, pJ \cdot 0.02 \cdot 0.15 \approx 15\, pC\,.$$

6.3.4 Photon detection

The last step to get a working system is to provide a fast, efficient, high-resolution and low-noise position sensitive detector. As anticipated in paragraph 6.3.1, a tailored 2-D

detector has been developed to match IEEM requirements. In the present paragraph, I will give a brief review of the sensor adopted for SIRAD IEEM; for a deeper and detailed description, I refer the reader to Piero Giubilato's PhD thesis work [71].

As already stated, the adoption of a CCD based detector is strongly suggested by their working principle, which ensures resolution performances which does not depend on the strength of the input signal. Moreover, the adoption of a digital detector would greatly simplify the data manipulation. The disadvantage of the use of square CCD arrays is the huge amount of pixels to be read. If only one event is registered in one frame, most of the readout resources are employed to read empty pixels which do not provide any useful information. The reduction of the number of pixels to be readout, without losing information, would free a great quantity of read-out resources, making the use of CCD a feasible solution.

The approach we adopted projects the light spot onto two orthogonal linear arrays (as sketched in fig. 6.12). The number of pixels to be readout is N (the two linear arrays are read out in parallel) rather than to N^2 for a square array, while the spatial resolution remains unaffected. A position of the peak in one linear array will indicate the coordinate, along the direction of the linear array, of the light spot.

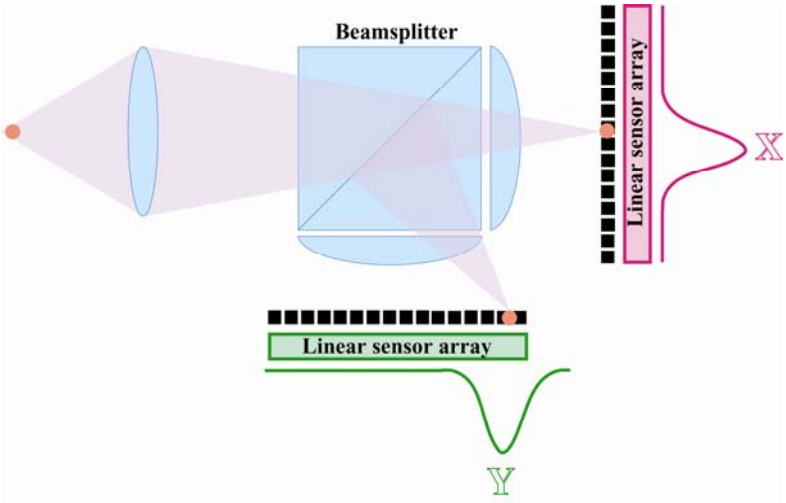

Fig. 6.12 Schematic drawing of the IEEM bilinear sensor.

The two projections of the light signal are obtained by an optical system that consisting a beamsplitter, that splits the original light spot into two copies, and cylindrical

lenses, placed along the two orthogonal optical paths, that squeeze each light spot into a blade shape (fig. 6.13). The two orthogonal light blades are then detected by an NMOS linear array [73], chosen for its ease of use and pixel shape (2.5mm × 50μm). The pixels are very wide and this maximizes the collection of the photons in the light blade, important when working in these low-light level conditions. The main drawback of the chosen sensor is its very low speed readout rate (2 MHz). In the present prototype, the device is overclocked to 3.125 MHz, resulting in a frame rate of $3.125\times10^6/256 \sim$ 12.2kframe/s.

Proprietary electronics has been developed to both drive and read the two linear sensors. Two fast (40MHz) 12 bits ADCs (one per axis) convert the analog signal read from the sensor into digital format. Digitized data incoming from the ADCs are processed in parallel by an FPGA-based system, loaded with proprietary firmware. The position of the light spot is detected and fitted. When an event has been identified, a packet of 8 bytes is sent to the control PC via a USB connection. The event reconstruction (i.e. the peaks matching) is implemented at software level. The analysis package also allows one to deal with multiple events per frame by watching the height of the registered peaks and matching peaks of equal eight.

Bench measurements for estimating the spatial performance shows that, everywhere in the useful area of the sensor, the resolution is better than 650 *lrp* (better than 1000 lrp over 70% of the useful area), with a distortion (a systematic error that can be corrected) under 1%. The sensor meets the time and spatial requirements for IEEM applications.

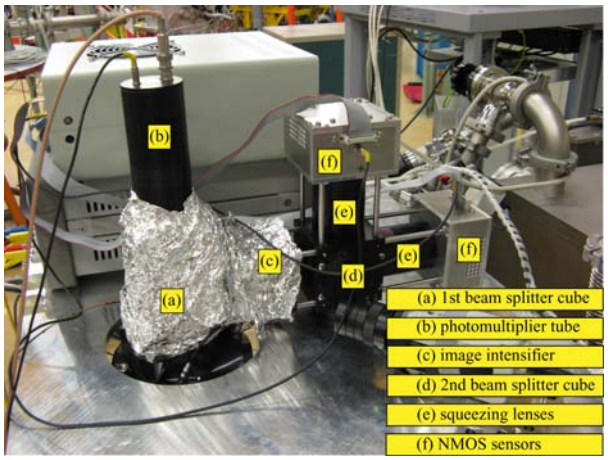

Fig. 6.13 The bilinear detector system. The optical signal is reflected upwards by a mirror and out a viewport into a first beam splitter (a). Part of the signal is detected by a PMT (b), the rest is reflected horizontally, regenerated by an image intensifier(c) and sent to a 2nd beam splitter (d). Each copy of the image is squeezed (e) and detected by a linear NMOS array (f).

7. IEEM imaging, targets and detection efficiency

7.1 IEEM Imaging in the axial configuration

7.1.1 Introduction

With the novel digital bilinear sensor and the new irradiation chamber we tried to get a straightforward secondary electron emission image of a target with the IEEM in axial configuration. Two simple objects were mounted on the sample holder: a 25 μm pitch copper calibration grid to obtain a recognizable image and a PIN diode to measure the ion impact rate on the target. The PIN diode was surmounted by a 100 μm thick Si_3N_4 membrane with a 40 nm layer of Au and imaged to measure the ion impact detection efficiency of the IEEM.

7.1.2 First IEEM image in axial configuration

First the ion beam (^{79}Br at 234 MeV) was focused onto a quartz scintillator ~ 2 meters upstream of the IEEM chamber. The beam was then defocused and sent to the IEEM chamber. The PIN diode was used to measure the rate and energy of ions passing through the IEEM. The alignment and beam quality proved to be good as we were immediately able to detect good ion signals with the diode. We then moved the copper grid in position and tried to get an image on the MCP phosphor.

Our first attempt to obtain an image was a failure: the MCP was completely flooded by spurious positive ions particles created by beam scraping a diaphragm inside the PEEM near the decel lens (fig. 7.1)[1].

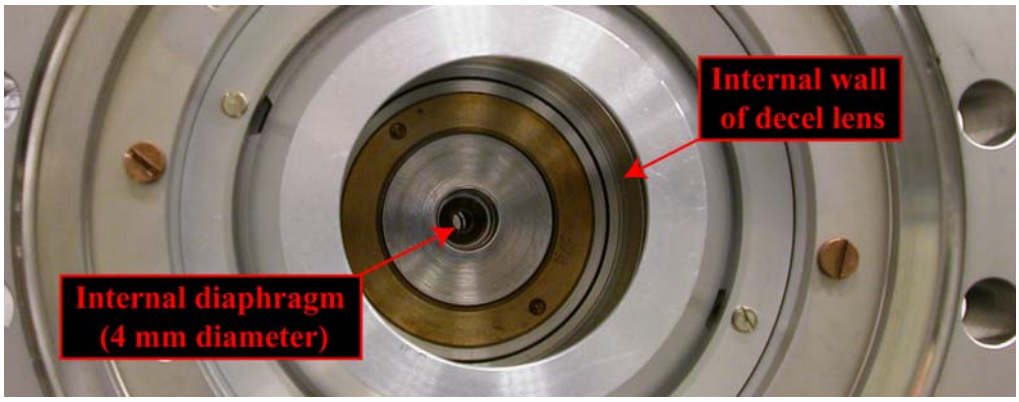

Fig. 7.1 Photo of the brass internal diaphragm near the decel lens.

To fix this we added two collimating diaphragms, one upstream of the MCP with a 1 mm aperture (fig. 7.7b), the second one, with a ~ 500 μm aperture inside a tube mounted inside the central hole of the MCP (fig. 7.7a). To avoid distortions in the electrostatic potential between the PEEM and the MCP a biasing wire was added to the tube of the second diaphragm to keep it at the entrance potential of the MCP. This wire is upstream of the MCP and intercepts part of the light emitted by the phosphor; i.e. it casts a small shadow with the consequent loss of a not negligible quantity of event, as we will show in the following chapter.

[1] Positive ions created by beam scraping the contrast diaphragm do not reach the MCP. Negative ions and electrons have the wrong polarity.

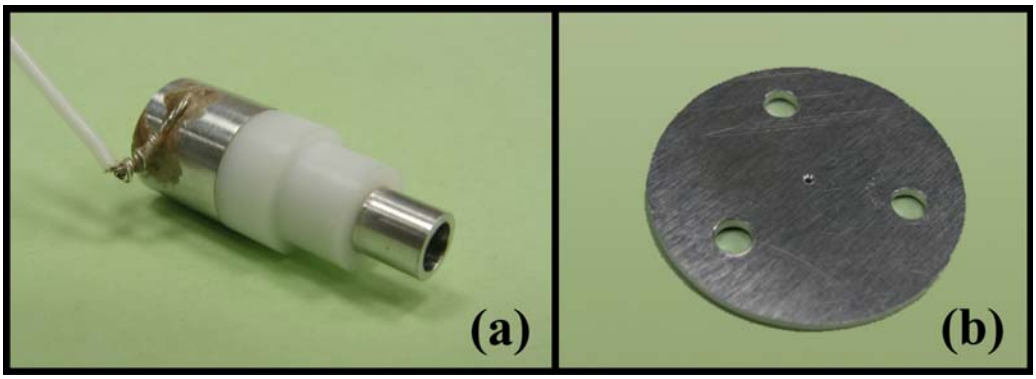

Fig. 7.2 (a): biased tube positioned through the MCP central hole; the diameter of diaphragm ~ 1mm. On the left it is also visible the biasing wire. (b): diaphragm preceding the MCP with a 500 µm diameter.

These collimating diaphragms make the alignment of the IEEM system slightly more delicate. The alignment is performed the following way: a laser beam (fig. 7.3) is sent back up through the contrast diaphragm, passing up through the IEEM and the MCP diaphragms, onto a quartz scintillator placed in a diagnostic chamber ~2 meters upstream.

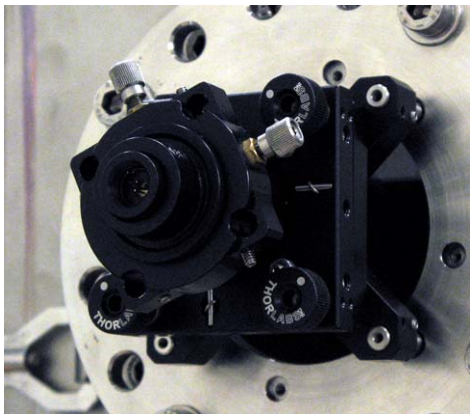

Fig. 7.3 Laser system for fine beam alignment.

This same quartz is used during ion beam setup: the image of the focused ion beam spot (few mm) is superposed with the recorded one of the laser spot. The aligned ion beam is then sent down the IEEM system. The beam intensity is lowered, first by closing accelerator and beam line slits, then by magnetic defocusing using the magnetic quadruple doublets of SIRAD. The flux of ions passing through the IEEM system is measured using a diode placed on the IEEM sample-holder and tuned by adjusting the

defocusing. This defocusing technique works very well if the beam is well aligned with the magnetic axis of the quadrupoles.

We show in fig. 7.4 a raw ion induced secondary electron emission image of a 25μm pitch copper grid exposed to 234 MeV Bromine ions. The IEEM magnification is 225×; the field of view (FOV) is 175 μm across. The image, obtained using the new sensor, is composed using the reconstructed spatial and temporal coordinates of the light spots created by individual ion impacts.

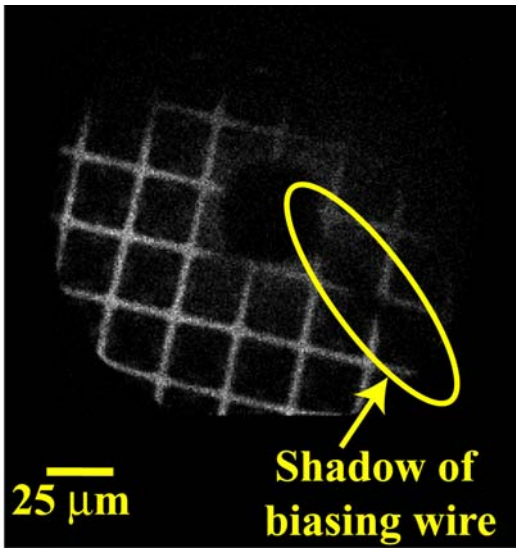

Fig. 7.4 Image of a copper grid irradiated with Bromine ions (234 MeV). This image is composed of single events, each with a time coordinate.

Several spurious signals are present in the resulting image. Some are dark counts of the MCP, but most of them (which are denser around the central hole region) are due to a residual component of the halo induced by charged particles hitting internal elements of the microscope column, which are not completely eliminated by the two inserted diaphragm. We plane to introduce new smaller apertures during a scheduled upgrade of the whole setup in spring 2008.

7.1.3 Considerations regards the image of the grid

The image of fig.7.4 is a preliminary one and no particular solutions were adopted to avoid mechanical vibrations. In addition the grid cannot be used to precisely measure the resolution of the IEEM as the complex shape introduces non-uniformities of the electric field near the surface that affect the electron trajectories.

The incompleteness of the picture is mainly due to the combination of the two effects:

- a non perfect parallelism between the target and the IEEM focal plane;
- the presence of terrestrial magnetic field, the effect of which is not negligible.

In the first case, if the surface normal is not parallel to the microscope axis, the lack of symmetry in the distribution of the accelerating field between the sample and the first electrode of the microscope causes the imaging of an area of the sample that is away from the optical axis of the microscope. In addition to achieve the nominal resolution the angle formed by the surface normal and the microscope axis should be small to avoid selecting trajectories with the wrong energy: to obtain a resolution in the 1 μm range the angle formed by the sample normal and the microscope axis should never exceed 4°. This request is not too severe and can be corrected for by adding the tilting motorized stage (which was not yet available when the present experiment was performed).

The sample is an integral part of the field forming lens electrodes: it has to be sufficiently conductive and should not disturb the rotational symmetry of the electrical field in the vicinity of the microscope axis. A flat sample with linear dimensions larger than at least 5 times the gap formed by sample and microscope would allow imaging of its central part of about 2 mm diameter by translation in X and Y direction without affecting the image quality. Ideally flat samples are not mandatory for imaging, but the resulting deviation from a homogeneous accelerating field causes loss in lateral resolution.

Regards magnetic fields, the emitted electrons are of very low energy at the sample surface and are extremely sensitive to them. Any magnetic field component orthogonal to the microscope axis will image an area of the sample away from the optical axis. An example can help understand this. Suppose that to image a target one sets a certain

magnification and focuses the microscope. Ideally if one wobbles the objective lens around the value of optimal focus the whole image will move except for one fixed point (the center of the image) that should be at the center of the screen. If the sample is perfectly parallel to the microscope head, a component of the magnetic field which is orthogonal to the microscope axis smaller than 10 milligauss is sufficient to move the fix point away from the center of the screen. The intensity of the magnetic field on the earth surface is ~ 500mG. Unfortunately, our beamline is oriented almost in east-west direction and we are hence working in the worst condition, with the earth field perpendicular to the transfer field. The only possible solutions are to shield the stray fields with a mu-metal shielding or to compensate them with external permanent magnets (see also paragraph 8.2.5).

7.1.4 Membrane images

We also tested the behavior of the ultrathin membrane under beam irradiation. Given its shape (fig. 7.5) we chose to deposit gold on the non-flat side to minimize the lever-arm to the DUT. But from the discussion in the paragraph 7.1.3 about the importance of target flatness we expected heavy induced distortions in the electrical field.

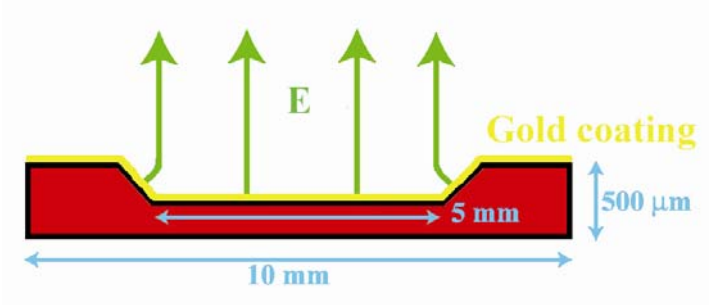

Fig. 7.5 Silicon nitride membrane section view reporting dimensions and electrical field lines.

It turns out that with this configuration only the central part of the membrane can be imaged (an area of ~ 1 × 1 mm^2). As expected, also the reconstructed image of the membrane is not complete, due to the not perfect sample alignment. However, it was noticed that by simply moving the target, the imaged part of the membrane changes shape

and orientation, and it becomes even larger and larger, until it is complete (see fig. 7.6). We interpreted this behavior as due to the presence of a slight bulge in the membrane, caused by the electrostatic attraction between the very thin gold membrane and the microscope column. The bulge introduces asymmetries in the transfer electric field: electrons emitted from the slope are not transferred properly and lost while those coming from the top of the membrane are successfully imaged. If you move the maximum of the bulge in axis and restore axial symmetry the image is complete

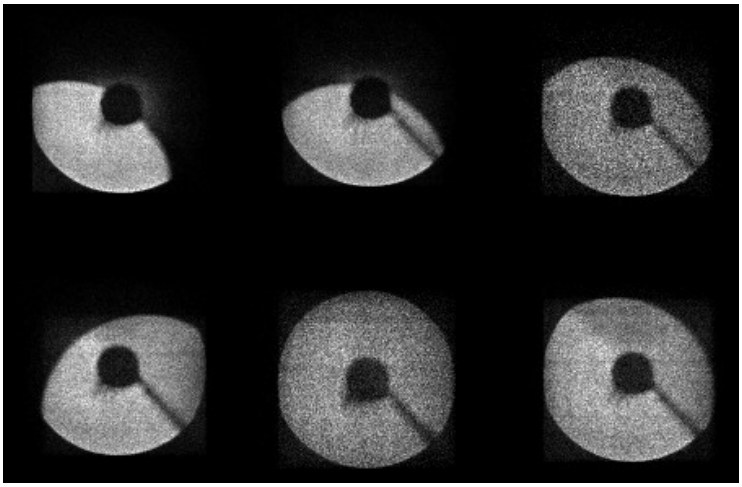

Fig. 7.6 IEEM reconstructed images of the golden membrane in different positions.

The copper grid is instead rigid and several tests moving it in different positions did not show the same behaviour of the membrane.

7.2 Target surfaces

7.2.1 Introduction

Secondary electron emission is at the basis of Ion Electron Emission Microscopy and the secondary electron (SE) yield is a key parameter in defining the IEEM performances. Metal surfaces impacted by swift ions generally emit secondary electrons. Instead the surfaces of microelectronic devices and circuits are likely to be very bad SE emitters; for protection purposes an oxide passivation layer is placed on the chip surface. To use an

IEEM it is hence mandatory to ensure adequate secondary electron emission from the surface of the Device Under Study (DUT) in a reproducible and reliable way.

7.2.2 Target preparations for IEEM

Two solutions to enhance SE emission from passivated chip surfaces have for the moment been considered for the SIRAD IEEM:

- the deposition of a thin (20÷40 nm) gold layer onto the chip surface. This is easily and reliably done if the device area to be irradiated is large and uniform. Of course one must carefully avoid short-circuiting conductive structures. It might be possible to avoid these problems by performing a two-layer deposition procedure: a thin non-conductive coating would first be deposited on the chip, followed by the gold deposition. This method requires a metal deposition laboratory and the knowhow to perform the R&D to prepare the many various types of devices that might be studied. At the target laboratory of LNL we successfully deposited 35 nm of gold on a Synchronous-DRAM and performed various compatibility tests (electrical and mechanical) with the IEEM.
- the introduction of a self-standing ultra-thin electron emitting membrane (20÷40 nm gold on 100 nm Silicon Nitride membrane [74] on a rigid Silicon Nitride window frame) between the IEEM head and the surface of the device under test (fig. 7.7).

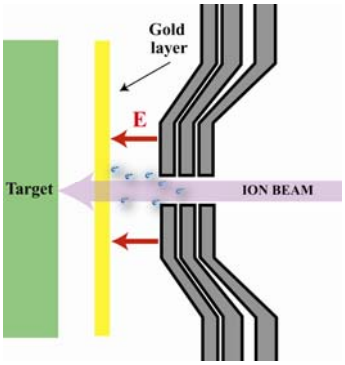

Fig. 7.7 Golden layer between target and PEEM to ensure an adequate secondary electron emission.

This solution gives the following advantages: near independence from the devices under test, hence no need for any sample preparations; reproducible standards of SE emission; complete separation of the IEEM high electrical transfer field from the surface of the device under test (DUT). However in traversing the membranes the ions suffer from energy degradation and angular scattering. The membranes hence must be very thin to minimize energy loss and angular scattering but then they become very delicate. All of this will be discussed quantitatively in this chapter.

7.2.3 Membranes: lateral resolution degradation

Self-standing gold/Si_3Ni_4 membranes are a quick way to ensure secondary electron emission from a device under test (DUT). They introduce both energy and resolution degradation and should therefore be very thin. In practice a gold thickness ~20 nm will ensure a copious and uniform electron emission [75]. As we will see in the next section, these membranes are so thin that they do not significantly degrade the energy of the ions.

The angular deflections due to multiple scattering are small too, but the membranes are so delicate that to avoid tearing them they cannot be directly put in contact with the DUT and must be kept at a distance (~200÷1000 μm) from the DUT. In this case the angular deflections projected over such large distance introduce significant degradations in lateral resolution. Of course gold membranes would be more affordable at higher energy ion accelerators.

For a given ion energy, three parameters contribute to the resolution degradation introduced by the introduction of the thin gold membrane: the gold deposition thickness, the Si_3N_4 membrane thickness and the lever arm between the membrane and the target surface (see fig 7.8).

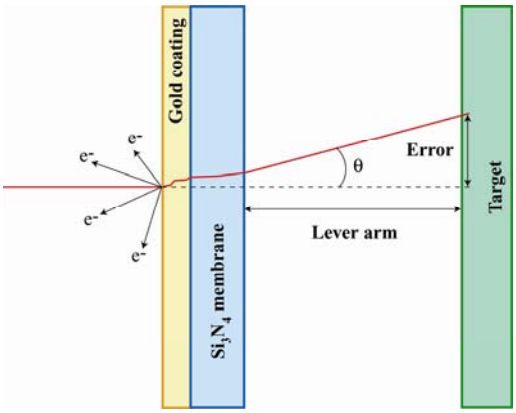

Fig. 7.8 Sketch of multiple scattering phenomenon degrading resolution.

The standard Silson silicon nitride membrane windows consists of square silicon nitride membranes in square silicon supporting frames. The one we use has a frame size of 10 mm and a membrane size of 5 mm, with a golden deposition of 40 nm over a Si_3N_4 thickness of 100 nm (fig. 7.9).[2]

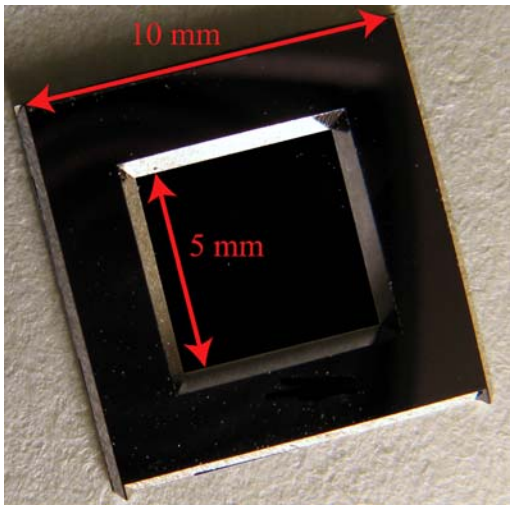

Fig. 7.9 Silson golden Si_3N_4 membrane 100 nm thick in a 10×10 mm frame.

[2] In practice we used a gold coating of 35 nm that was not deposited directly on the Si_3N_4 but on a chromium layer 10÷15 nm thick to ensure a better adherence. We verified that the total thickness of gold and chromium layers is equivalent to ~40 nm of gold.

The lever arm should be obviously kept as short as possible to minimize the lateral deflection, compatibly with mechanical constrains (the presence of bonding wires, for example).

To get a quantitative estimation of the error introduced, some SRIM [76] simulations has been performed. The output file of this simulations package provides the director cosines of the outgoing ion trajectory, as pictured in fig. 7.4.

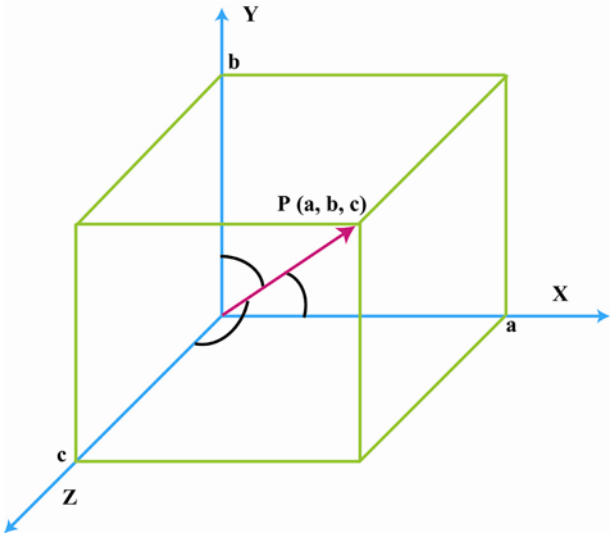

Fig. 7.10 View of coordinate system.

The relationships of the director cosines with Cartesian coordinate are given by the following formulas:

$$(7.1)\quad \cos(X) = \frac{a}{\sqrt{a^2 + b^2 + c^2}}$$

$$(7.2)\quad \cos(Y) = \frac{b}{\sqrt{a^2 + b^2 + c^2}}$$

$$(7.3)\quad \cos(Z) = \frac{c}{\sqrt{a^2 + b^2 + c^2}}$$

For these simulations:

$$\cos(X) \approx 1 \quad (7.4)$$

and therefore we can assume:

$$a \approx \sqrt{a^2 + b^2 + c^2} \quad (7.5)$$

$$b \approx \cos(Y) \cdot a \quad (7.6)$$

$$c \approx \cos(Z) \cdot a \quad (7.7)$$

In table 7.1 we report the results of simulations for lateral displacement for some ionic species at the energies available at SIRAD and for three different coating thicknesses (20 nm, 40 nm, 60 nm) at a lever arm of 200 μm.[3]

	Lateral displacement (in μm) at 200 μm							
Gold thickness (nm)	^{35}Cl (171 MeV)		^{58}NI (220 MeV)		^{79}Br (241 MeV)		^{127}I (276 MeV)	
	100 nm Si_3N_4	No Si_3N_4	100 nm Si_3N_4	No Si_3N_4	100 nm Si_3N_4	No Si_3N_4	100 nm Si_3N_4	No Si_3N_4
20	0.23	0.19	0.29	0.26	0.30	0.25	0.41	0.34
40	0.31	0.29	0.34	0.36	0.41	0.41	0.58	0.51
60	0.34	0.32	0.44	0.41	0.55	0.45	0.62	0.60

Tab. 7.1 Lateral displacement (RMS) for heavy ions passing through a golden layer.

The lateral displacement is here expressed as the RMS of the (Gaussian) distribution of position spread. We report in fig. 7.11 the example of one of the obtained histograms.

[3] These SRIM simulations are compatible (within few percent) with the simulations performed with GEANT 4 [77].

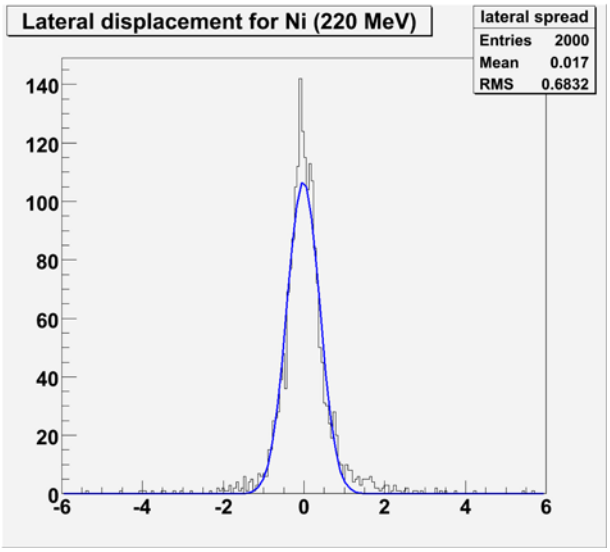

Fig. 7.11 Example of lateral displacement for ^{58}Ni (220 MeV) on 20 nm Au and 100 nm Si_3N_4.

As expected, the main contribution to position spread comes from the metal deposition, while the contribution of the silicon nitride membrane is in the order of ~ 10%.

From fig. 5.5, the theoretical IEEM resolution corresponding to a contrast diaphragm with an aperture of 200 μm diameter is ~ 400 nm. For the ionic species available at SIRAD and considered in our simulations, the effect of scattering introduced by a gold layer of 40 nm is smaller than or comparable to the IEEM resolution (except for the 276 MeV Iodine), provided that the distance between the membrane and the DUT (lever arm) is not larger than 200 μm. Clearly the main difficulty is to place the Au/S_3N_4 membrane and the DUT so close. This positioning is very challenging because it could easily be hampered by the presence of bonding wires or by some thick devices in the vicinity of the DUT.

The use of membranes to enhance secondary electron emission from a DUT is a handy and easy approach and it indeed allowed us to develop the IEEM quickly. It must be noted that the difficulty in using membranes I have just illustrated is just the first one. We will see more drawbacks in this and in the following chapter. Membranes may not be the definitive solution.

In concluding this section it is certainly worth pointing out that the degradation in resolution could also be kept small by using materials less dense than gold such as aluminium (oxidized). In tab. 7.2 we report the results of simulations of the lateral displacement for the same ionic species of tab. 7.1 for a 100 nm of Si_3N_4 membrane with a deposition of 40 nm of aluminum (not oxidized). Compared with the corresponding values for gold deposition the resolution is improved better than ~ 50%.[4]

	Lateral displacement (in μm) at 200 μm			
Membrane thickness	^{35}Cl (171 MeV)	^{58}NI (220 MeV)	^{79}Br (241 MeV)	^{127}I (276 MeV)
40 nm Al on 100 nm Si_3N_4	0.129	0.178	0.194	0.232

Tab. 7.2 Lateral displacement (RMS) for heavy ions passing through an Al_2O_3/Si_3N_4 membrane.

7.2.4 Membranes: energy degradation

Beside degrading the resolution degradation the scattering process in the membrane also produces an energy degradation for the incident ions. In table 7.3 we report the energy loss in traversing a gold/Si_3N_4 membranes of four typical SIRAD ions, expressed as fraction of the initial energy of the incident ion.

[4] For thin membranes the angular deflection scales like $\vartheta \propto \frac{Z}{E} \times \sqrt{\frac{x}{X_o}}$ were Z and E are the atomic number and energy of the impinging ion, x is the thickness of the membrane and X_0 is the radiation length of the membrane material. The radiation length is approximately given by the expression $X_0 = \frac{716 \cdot A}{Z(Z+1)\ln\frac{287}{\sqrt{Z}}}$ g·cm^{-2} where A and Z are the atomic weight and atomic number of the material.

	Energy degradation (%)							
Gold thickness (nm)	^{35}Cl (171 MeV)		^{58}NI (220 MeV)		^{79}Br (241 MeV)		^{127}I (276 MeV)	
	100 nm Si_3N_4	No Si_3N_4	100 nm Si_3N_4	No Si_3N_4	100 nm Si_3N_4	No Si_3N_4	100 nm Si_3N_4	No Si_3N_4
20	0.40	0.13	0.71	0.22	0.92	0.28	1.24	0.37
40	0.53	0.26	0.93	0.44	1.20	0.56	1.61	0.74
60	0.65	0.38	1.15	0.66	1.48	0.84	1.98	1.11

Tab. 7.3 Energy loss (%) of typical heavy ions passing through the membrane for different golden deposition thicknesses.

The most important physical parameter for SEE studies is LET_0, which weakly depends on energy. The energy loss after the Silicon Nitride membrane is so small (less than 1.6% using 40 nm of gold, the thickness we adopted) that it does not cause great dispersion in the LET_0 value. In fig. 7.12 we report the energy straggling due to a golden Si_3N_4 membrane (40 nm of gold) for 220 MeV Nickel ions.

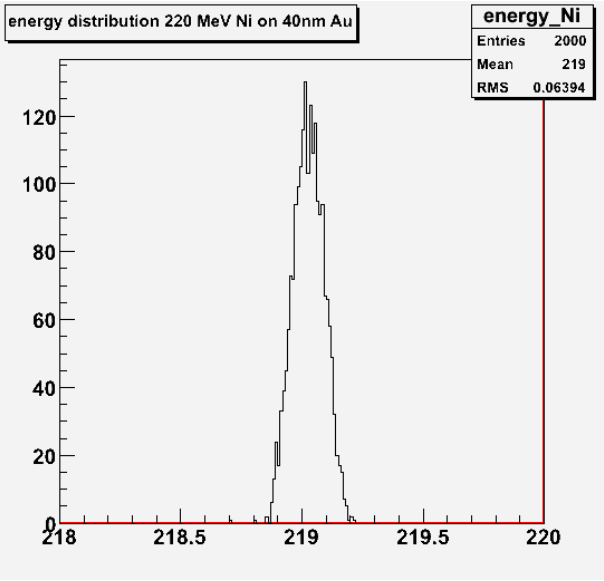

Fig. 7.12 Energy distribution of ^{58}Ni ions (220 MeV) after passing the golden membrane.

7.2.5 Membranes: secondary electron emission experiments

As no experimental data on the electron yield from gold surfaces from energetic heavy ions available at SIRAD was present in literature, specific measurements were performed at SIRAD using a wide selection of ions [78]. We used three Au targets (one bulk and two thin gold deposition, 70 μg/cm^2 and 200 μg/cm^2 on 2 μm thick mylar). Measurements were also made using an aluminum (oxidized) target.

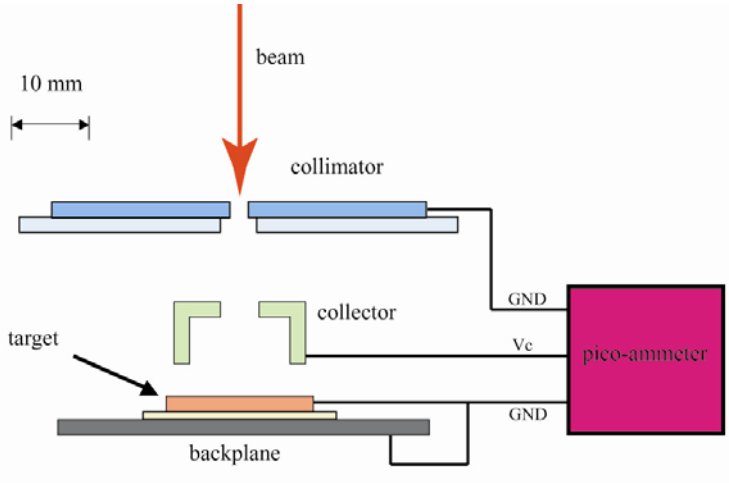

Fig. 7.13 Schematic drawing of the experimental setup

A simple Faraday cup system (fig. 7.13) was used to perform the yield measurements: the secondary electrons emitted by the target, electrically grounded, were suppressed or collected by an independent electrode, depending on the voltage polarity of the latter. During irradiation the collector voltage V_c was slowly ramped up from –100 V to 100 V in steps of 1 V/s. Currents on the target and collector were measured simultaneously as a function of the collector voltage V_c with a precision multi-source pico-ammeter. When V_c is large and negative enough ($V_c \leq -35$ V) the target current consists only of the incoming positive beam current and is recorded with a negative sign; when electron emission is not suppressed the pico-ammeter measures a larger negative current due to the contribution of the electron current. As the collector voltage is increased to more positive values electron collection becomes more efficient and for $V_c \geq 10$V it is complete (fig. 7.14).

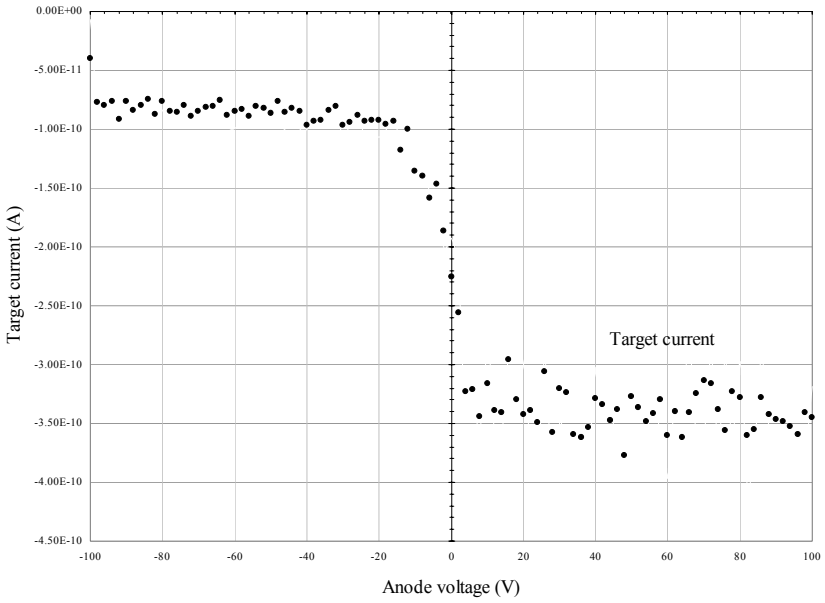

Fig. 7.14 Typical measurement of anode current of the faraday cup as a function of the collector voltage. Reported values refer to 158 MeV ^{28}Si beam on Au target. Similar results have been obtained by varying ion species and metal target.

Indicating with I_{beam} the target current with complete suppression and with I_c the collector current with complete collection, the electron yield per ion impact is given by the formula:

$$(7.1)\quad Y_c = Q \times \frac{I_c}{I_{beam}}.$$

Typical beam currents were in the range 10-25 nA but consistent results were obtained with beam currents as low as 1 nA; i.e. the secondary electron emission values reported in table 7.4 were not space-charge limited.

Ion	Q (e)	Energy (MeV/amu)	LET_{Au}(eV/A)	LET_{Al2O3}(eV/A)	Y_{Au}	Y_{Al2O3}
$^{12}C_6$	+6	7.92	145	66	10.9 ± 5%	8.2 ± 10%
$^{16}O_8$	+7	6.81	272	123	18.2 ± 5%	12.6 ± 10%
$^{19}F_9$	+8	6.47	348	163	22.3 ± 5%	15.5 ± 5%
$^{28}Si_{14}$	+11	5.64	796	357	40.0 ± 5%	24.0 ± 5%
$^{35}Cl_{17}$	+12	4.91	1139	527	56.7 ± 10%	33.9 ± 10%
$^{48}Ti_{22}$	+14	4.08	1744	872	85.2 ± 6%	48.2 ± 8%
$^{58}Ni_{28}$	+14	3.60	2448	1230	91.5 ± 10%	81.3 ± 12%
$^{79}Br_{35}$	+18	3.16	3231	1731	123 ± 10%	86.0 ± 12%
$^{107}Ag_{47}$	+20	2.54	4344	2427	129.8 ± 10%	119.5 ± 12%

Tab. 7.4 Ion species, surface LET values (SRIM2003) and measured average yields from Au and oxidized aluminum (Al_2O_3).

As a secondary result, from the smooth slope of the curve of induced target current as a function of the voltage of the collector (fig. 7.15), we could give a rough estimation of the energy spread of emitted secondary electrons at the metal surface. The FWHM of the change in the slope across V = 0V is ~ 5eV and is a rough measure of the energy spread of the secondary electrons. This value experimentally confirm what was assumed in [56] to estimate the spatial resolution and the transmission efficiency of the IEEM.

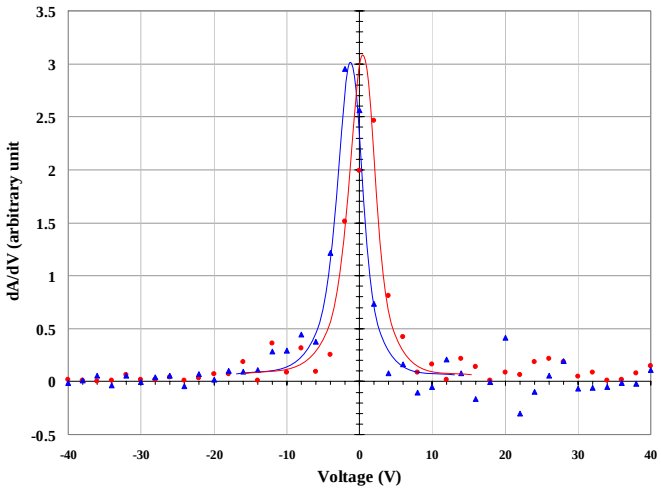

Fig. 7.15 **The average slope of the Au target anode current as a function of the anode voltage for typical measurements using Si and Br beams.**

In figure 7.16 we show the experimental yield data for the Au target of table 7.4 as a function of the atomic number Z. The figure also shows the expected values at SIRAD with the tandem at 14 MV and using the highest probability charge states. The thick black curve shows the expected yield if one naively assumes it to be proportional to the LET of the ion, while the red diamonds, joined by the red dashed curve, are the expected yields for the typical ions and energies available at SIRAD according to fit function:

$$(7.2)\quad Y = a \cdot Z^{b-2} \cdot LET_0\left(eV\Big/\mathring{\mathrm{A}}\right).$$

For Au targets the best fit parameters are a = 0.168 ± 0.015 Å/eV and b = 1.561 ± 0.035 using the LET_0 (eV/ Å) values of SRIM2003. The best fit function represents the average yields value, the effective secondary electron emission by ion impact on Au following Poisson statistics, as shown by Itoh et al. [79] for ions with Z ≥ 10. For Al_2O_3 the best fit parameter values we obtained are a = 0.268 ± 0.041 Å/eV and b = 1.51 ± 0.06.

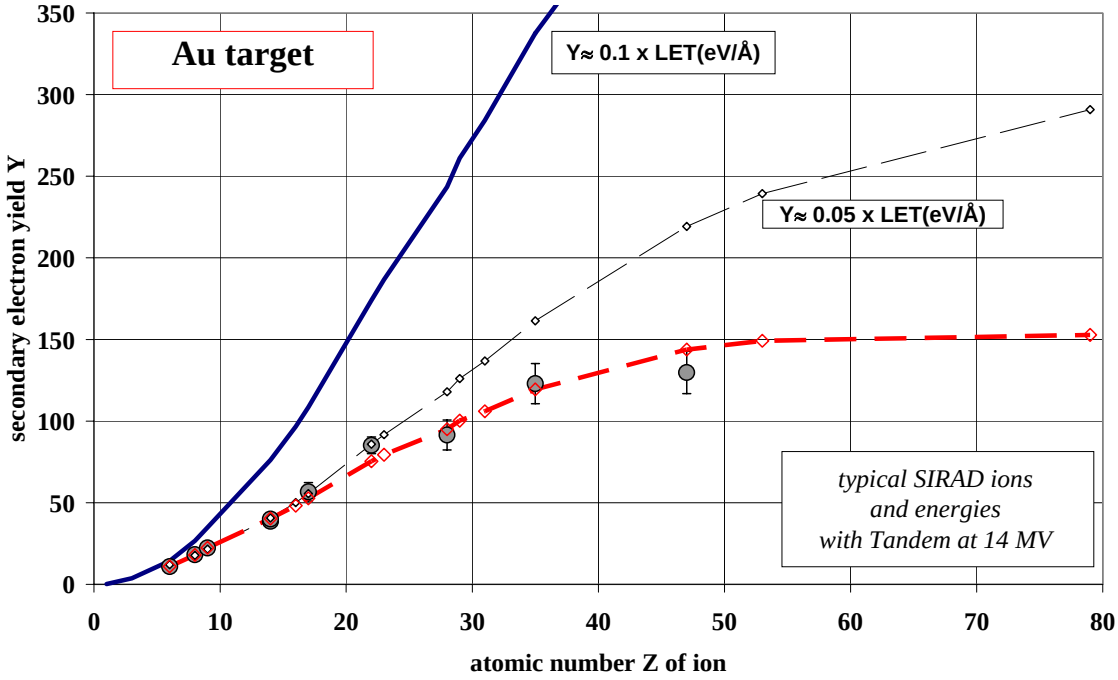

Fig. 7.16 **The mean number of secondary electrons Y emitted from a gold target expected at SIRAD as a function of the atomic number Z of impinging ions. The data points are the values obtained at SIRAD. The red diamonds, joined by the red dashed curve, are the expected values according to the fitting function 7.2. The black curves are the expectation assuming naively that Y be proportional to the LET.**

7.3 Detection efficiency

7.3.1 Introduction

The efficiency in detecting ion impacts is clearly an important issue in IEEM applications, in particular when small SEE cross section have to be measured. It is not desirable that an ion strike an electronic component and trigger a single event effect but go undetected by the IEEM. The final ion impact detection efficiency of an IEEM clearly depends on the yield of the secondary electron emission, but it also depends on the IEEM in several ways that include electron collection and transport efficiency of the PEEM and the detection efficiency of the detector ensemble.

7.3.2 Efficiency estimates

We estimated the global SIRAM IEEM ion detection efficiency off gold and oxidized aluminum surfaces as a function of the atomic number of the impinging ion for various size apertures in the contrast diaphragm (fig. 7.17). The estimates are based on several assumptions:

- the Tandem accelerator working at 14 MV and the most probable charge states after momentum analysis (Tab. 6.1);
- the average secondary electron yield Y given by equation 7.2, the best fit parameters a and b obtained measured at SIRAD, and SRIM2003 for calculating LET_0;
- the MCP detection efficiency to be $\varepsilon_{MCP} = 55\%$ for single electrons [5];
- the collection-transmission efficiencies ε_{trans} for different apertures in the contrast diaphragm of the IEEM. These have been calculated and measured by Doyle et al. [56]. For a 300 μm aperture contrast diaphragm they calculated 30% (fig. 5.5) and measured 10%. For an aperture of 300 μm we assumed $\varepsilon_{trans} = 10\%$ value; for a 200 μm aperture we assumed $\varepsilon_{trans} = 5\%$; for an aperture of 150 μm we assumed $\varepsilon_{trans} = 3\%$.
- the number of electron emitted follow Poisson statistics, a good assumption for gold for $Z \geq 10$;
- the efficiency of the IEEM is $\varepsilon = 1 - \exp(-Y \times \varepsilon_{MCP} \times \varepsilon_{trans})$

Using ultrathin Au/Si_3N_4 membranes superimposed to a microelectronic device under SEE testing or direct gold deposition on the device, and using a contrast diaphragm of 300 μm, we conclude conservatively that the detection efficiency of the IEEM at the

[5] This is a conservative value for detecting the secondary electron clouds from heavy ion impacts with the IEEM: given the finite spatial resolution of the IEEM, multiple secondary electrons emitted by a single heavy ion impact are focused not to a point but to a spot that can comprise many micro-channels, raising the effective MCP efficiency near 100%.

SIRAD facility will be better than 50% for ions with Z > 7÷8 with LET_0(Si) ~ 2 MeV-cm^2/mg and will reach full efficiency for Z > 23 with LET_0(Si) ~ 21 MeV-cm^2/mg. We are evaluating novel materials with average secondary electron yields higher than Au: for a factor two increase in yield, the SIRAD IEEM would be fully efficient with Z > 14 and LET_0(Si) ~ 9 MeV-cm^2/mg.

It is important to note that for a small aperture of 100 µm the ion impact efficiency of the SIRAD IEEM does not reach 100% even for the heaviest ions. This occurs because the secondary electron yield Y does not continue to grow as one would naively expect if Y were proportional to LET_0 but, in the case of gold, it saturates at a value of ~ 150 electrons (fig. 7.16).

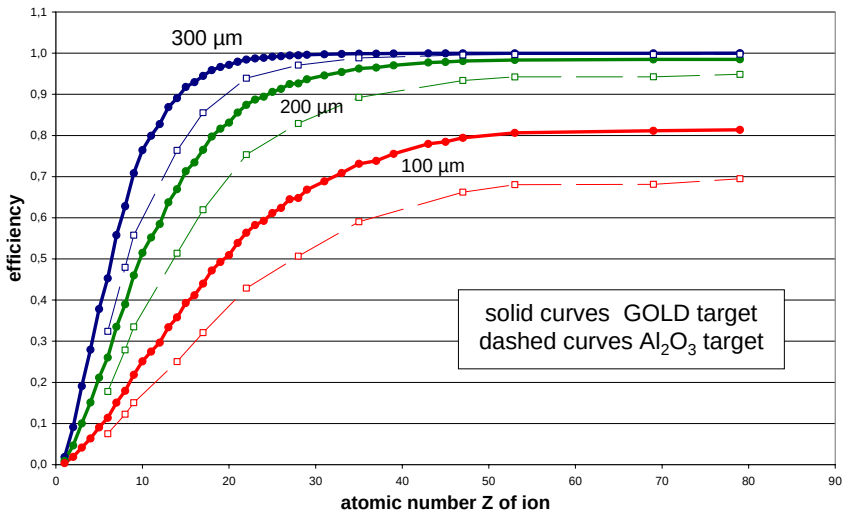

Fig. 7.17 Conservative estimation of the ion detection efficiency of the SIRAD IEEM off a gold and oxidized aluminium target for different diameter apertures in the contrast diaphragm as a function of ion atomic number.

The secondary electron yields of an oxidized aluminium target are lower than those obtained using a gold target and indeed the ion detection efficiency dashed curves in fig. 7.17 are lower than the solid ones for gold. It should be noted that if one uses the 200 µm aperture the IEEM efficiency is still quite good for the heaviest ions, those that suffer greater angular deflections. For this reason and for the reduced degradation in resolution,

aluminium/Si_3N_4 free-standing membranes could be an attractive solution for SEE studies using the heaviest ions.

7.3.3 Ion counter

To perform a direct measurement of the ion detection efficiency of the IEEM, a target is needed which both counts the number of impacting ions and emits secondary electrons to be revealed by the IEEM.

For this purpose a PIN diode surmounted by an ultrathin Au/Si_3N_4 membrane is used (see fig. 7.18).

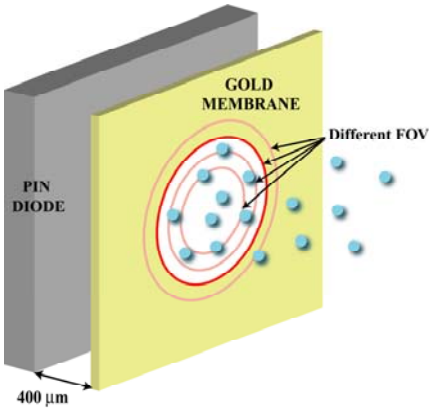

Fig. 7.18 Schematic drawing of the target for efficiency measured.

For each ionic impact, a proprietary electronic system amplifies and shapes the signals from the diode, and provides a TTL signal.

The gold layer provides the secondary electrons; for this efficiency measurement the distance between the diode and the membrane is not a concern and the two were kept at a distance of ~ 1mm.

7.3.4 Fast triggers

A fast physical signal from the IEEM, in correspondence with the detection of the ion impact, is needed.

The natural choice was to obtain an electronic signal from the output of the MCP. The MCP is mounted on a support and is surrounded by a voltage divider that provides the correct voltage for the two plates and for the phosphor screen (fig. 7.19). When an electron avalanche is generated, either as a consequence of a true ion strike or generated internally (dark noise), it induces a spike signal in the biasing circuit of MCP plates. This signal is brought outside the chamber to be amplified and digitized. The external amplification (performed by a proprietary electronics) is a handy solution, allowing for the easy optimization of the signal, and, in case of destructive discharge, the components can be easily replaced. A filter was been added at the output to reduce the noise (voltage spikes and ripples) induced by the MCP power supply.

However, this approach is not completely satisfactory. The pre-amplifier is distant from the detector itself: the noise level is high and the discriminator level has to be kept high with a loss of too many signals from real ion impacts.

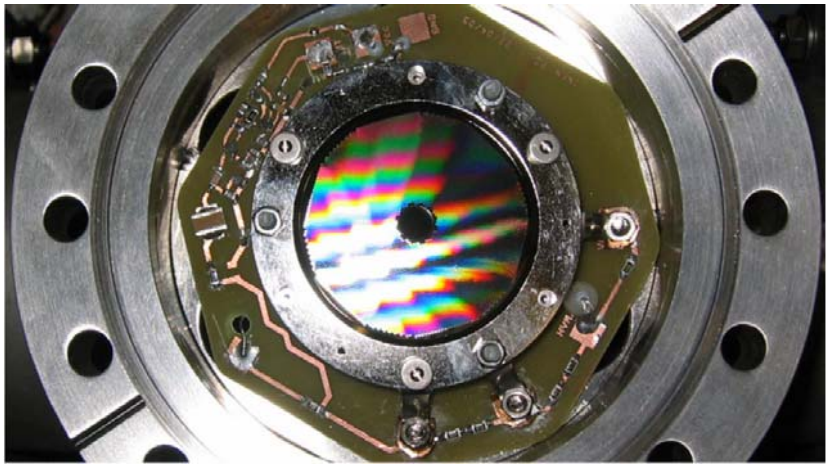

Fig. 7.19 MCP assembly viewed form the side facing the PEEM output with its power supply lines.

An alternative robust trigger system was developed that makes use of the light signals from the phosphor screen. It is robust and low-noise and completely decoupled from the power supply of the MCP and the IEEM.

The electronic avalanche generated by the MCP excite the phosphor to create photons that are extracted from the irradiation chamber through a viewport. The photons enter a beam-splitter: half proceed towards the image intensifier and the NMOS position sensor,

the rest are reflected towards a photomultiplier tube (PMT) from Hamamatsu (fig. 7.20) that generates a fast trigger signal. It should be noted that there are optical elements *before* the beamsplitter that focus the photons onto the input photocathode screen of the image intensifier. The PMT we chose can be placed in the working position, *after* the beamsplitter, without the need of any additional optics as its diameter is larger than that of the input of the image intensifer. This is a nice "plug-and-play" feature.

For focusing the IEEM and general debugging the PMT tube can be easily replaced by a conventional CCD camera.

Fig. 7.20 Hamamatsu R3886 photomultiplier tube proving a fast trigger.

The signal from the PMT is amplified and shaped by a standard NIM electronics.[6] The shaped signal duration time is ~ 1 μs, but this is fast enough to allow rates up to hundreds of kHz, far beyond the real working conditions rate.

7.3.5 Efficiency measure setup

The purpose of the experiment is to measure the number of impacting ions successfully detected by the IEEM fast trigger. We do not here consider the reconstruction efficiency of the ion impact point which depends on the efficiency of the optics, the efficiency of the final NMOS detector, and the ability software to detect and to match the reconstructed peaks.

[6] The photon signal from the phosphor generated pulse is fast (< 5ns) and so large, compared to the noise level, that there was no need to design an "ad-hoc" low-noise circuit.

A specific target has been prepared (fig. 7.21) that comprises: a copper grid with 25 μm pitch to image for focusing the IEEM; a PIN diode surmounted by the gold membrane for the efficiency measurement.

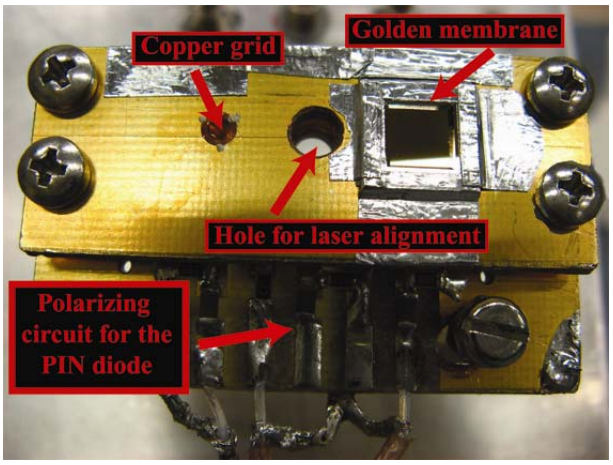

Fig. 7.21 Target for efficiency measure.

The PIN diode is moved into position and the gold layer is viewed by the IEEM. An ion will pass through the gold membrane and generate a signal in the diode; on the other hand the very same ion will extract secondary electrons from the gold and these should be detected by the PMT (fig. 7.22). We counted the number of fast signals from the PMT in coincidence with the electronic pulses from the diode for different field of views (FOV).

As the membrane is a uniform surface without any reference point, it cannot be used to set the PEEM field of view and to correctly focus the microscope. Preliminary calibration images have been performed with UV photons illuminating the copper grid to find the correct settings for PEEM lenses and to determine the correspondence between the FOV of the microscope and the value of the intermediate lens (i.e. the zoom lens) to be used to vary it.

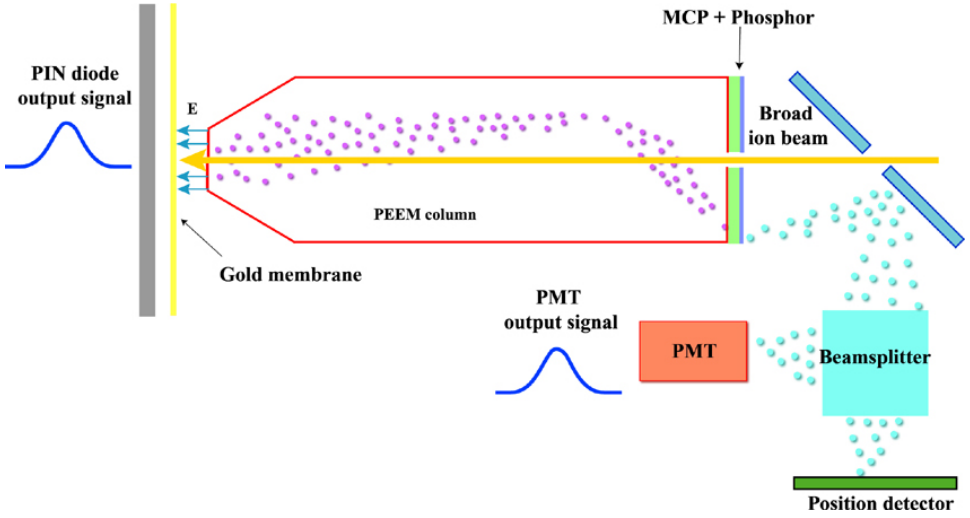

Fig. 7.22 Schematic drawing of the efficiency measure setup.

The experiment was performed with ^{58}Ni beam with an energy of 220 MeV. We started by finding a position of the gold membrane that maximized the emitting area. The two output signals, the one from the diode and the one from the PMT, are discriminated and sent to a NIM counting module. The discriminated signals are also sent to a NIM coincidence circuit that generates a coincidence signal that is also counted. The threshold of the discriminator circuit of the PMT signal is chosen so that no PMT dark counts are selected. Similarly for the diode: the threshold is raised so that no noise signals are counted.

The detection efficiency of the IEEM is the ratio between the coincidence counts and the diode counts:

$$efficiency = \frac{PMT \wedge diode}{diode} \tag{7.8}$$

We performed this measurement for different FOVs (varying the potential of the zoom lens while keeping the others constant) and for different MCP voltages.

7.3.6 Efficiency measure experimental results

For a field of view of ~170 µm diameter, we plot in fig. 7.23 the experimental efficiency as a function of the working voltage of the MCP in steps of 50V, from 4500 V up to the maximum voltage (5000 V) provided by the high voltage power supply:

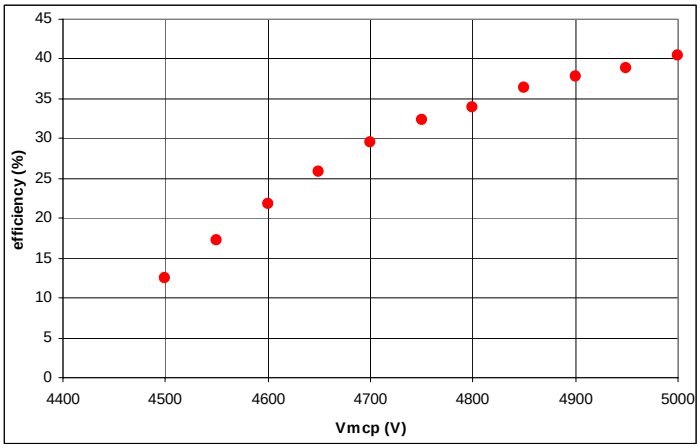

Fig. 7.23 Efficiency as a function of the MCP bias for a FOV of 170 µm.

The MCP manufacturer suggests the effective voltage to be 5kV and, if the MCP were correctly biased, a plateau in the efficiency curve would be expected. Instead we observed that at the highest voltages the efficiency is still rising and not fully efficient with the power supply set at 5kV. Indeed because of the filtering circuit added to the power supply output, the effective voltage on the MCP is lower than the voltage set by the power supply. To correctly supply the device, a power supply able to provide a higher voltage than 5kV is needed.

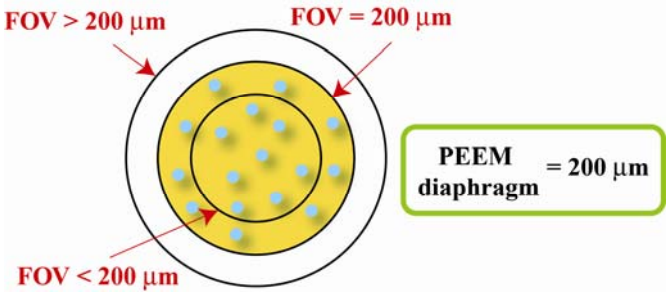

Fig. 7.24 The yellow area represents the region really hit by ions (diameter = 200 µm); the black circles are the possible FOVs: equal, larger or smaller than the contrast aperture.

Fixing the MCP bias at 5 kV, the highest value achievable with our power supply, we measured the efficiency for different diameter FOV, both smaller and larger than the diameter aperture of the contrast diaphragm (fig. 7.24). In fig. 7.25 we plot the obtained experimental values:

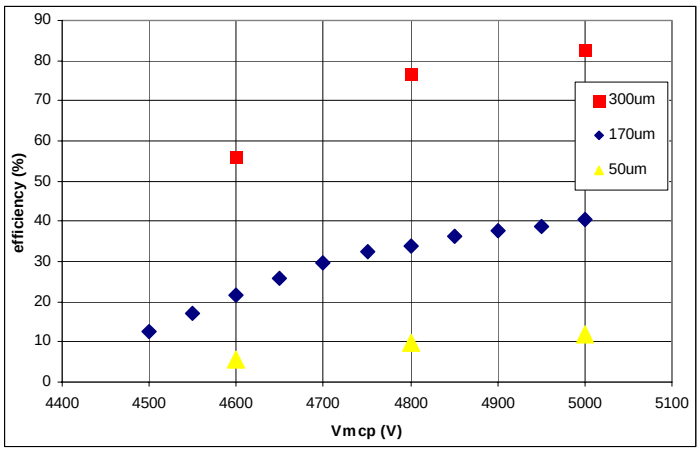

Fig. 7.25 Efficiency values for FOV of 300 µm, 170 µm and 50 µm.

The results obtained with the largest FOV are the significant ones as they ensure that all of the area that is impacted by the ions is viewed by the IEEM (fig. 7.24). The value of the efficiency obtained (83%) is the best experimental estimate of the maximum detection efficiency and is the one to be compared with the theoretical estimate one. We expect, for a ^{58}Ni (220 MeV) beam impacting a gold target, with a diaphragm aperture diameter of 200 µm and assuming the MCP fully efficiency at 55%, an ion detection efficiency of ~ 93% (fig. 7.17).

Several factors account for the 10% inefficiency. The 8 mm hole in the center of the MCP and the shadow of the biasing wire contribute to the inefficiency of an axial IEEM in detecting ion impacts contribute respectively 4% and ~2%. In addition the working voltage of the MCP was below the correct one: we estimate this to accounting for ~2% of the deficit. The residual ~2 % deficit is most-likely due to the incompleteness of the

image of the target (see section 7.1.4, in particular fig. 7.6).[7] This will be investigated in the future with a tilting stage.

The efficiency measurements I described are clearly preliminary ones.

The gold membrane we adopted is not the ideal choice. The gold coating on the receding side (fig. 7.26a) does allow us to keep the DUT target close to the membrane, reducing the lateral deviation of the ions, but the irregular surface exposed to the PEEM introduces distortions in the extraction electrical field which are not well understood. We could deposit the gold layer on the flat side of the membrane (fig. 7.26b) in order to get a uniform surface that does not distort the electrical field, but the thickness of the window (greater than 100÷200 μm to be robust enough to be manipulated) limits the minimum distance from the target to the emitting surface. In both cases the bulge effect introduces distortions.

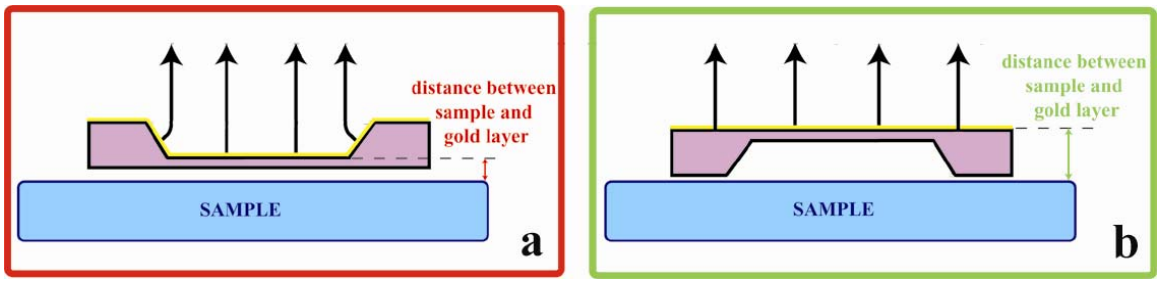

Fig. 7.26 Two possible scenarios for golden deposition: on the receding side (a) or on the flat one (b).

7.3.7 PMT signal as a fast trigger

A fast event trigger is useful in situations where the SEE in the DUT are immediately detectable, e.g. single event gate ruptures or burnouts (SEGR, SEB), single event latchups (SEL) in CMOS devices or IBIC experiments. It is important to investigate the goodness

[7] In section 7.1.4 we showed how the image of a membrane might be incomplete (fig. 7.6). If an image is incomplete, i.e. a significant number of ion impacts were not imaged by the IEEM, then the ion detection efficiency will be underestimated.

of PMT as a fast event trigger. A trigger signal is good if it is not only efficient but also clean: spurious trigger signals, not due to true ion impacts, are undesirable.

The shaped PMT signals are sent to a Multichannel Spectra Analyzer (MCA) [80] and acquired by a PC via serial interface. In fig. 7.27 we show the PMT signal spectrum of MCP dark counts (beam off) and the spectrum when the beam is on, both with the MCP voltage at 4.8 kV.

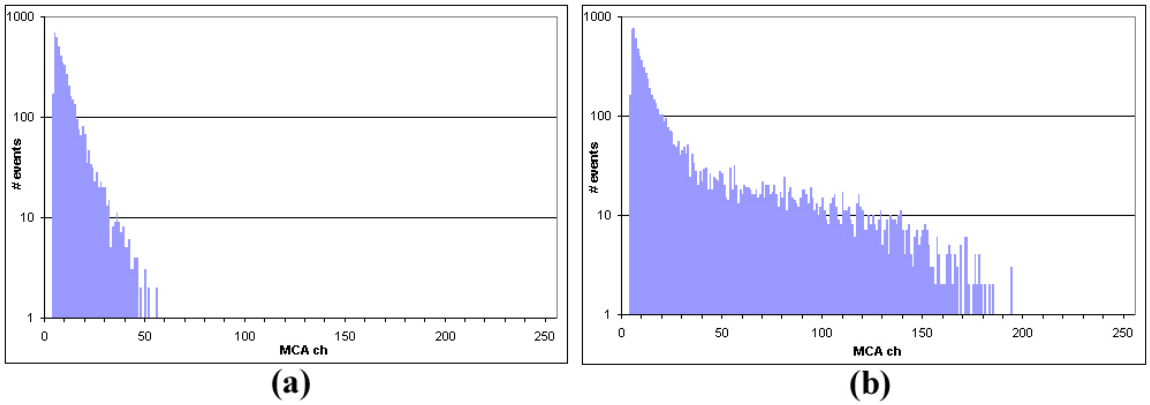

Fig. 7.27 Acquired PMT spectra with beam off (a) and beam on (b); V_{MCP} = 4.8 kV.

The MCA can be gated with the signal from the diode to obtain PMT spectra of only signals that are induced by a real ion strike. In fig. 7.28 we show the diode-gated PMT signal spectrum and the normalized beam-off PMT spectrum (dark MCP counts).

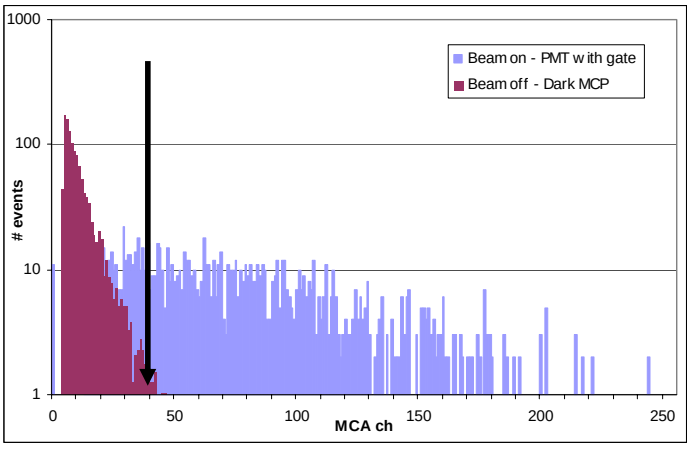

Fig. 7.28 Acquired spectra with beam off (violet) and with beam on and PMT signal gated by the diode (blue); V_{MCP} = 4.8 kV.

With a cut in the pulse height corresponding at channel 40 of the MCA (the black arrow in the plot of fig. 7.28), the fraction of dark counts above the cut is ~ 1%, but the fraction of ion counts lost is not small (~ 24%).

In fig. 7.29 we again show the PMT spectrum with beam off and with beam on gated with the diode but the MCP voltage is now at 5 kV. With the same cut in the pulse height (ch. 40), the fraction of MCP dark counts above this threshold is ~ 6%, while the fraction of real impact events lost is only ~ 2%.

With a proper calibration, we would be able to set the NIM discrimination threshold to correspond to the above cut in the pulse height spectrum.

The dark counts of the large MCP can be effectively discriminated against, while retaining a high efficiency for heavy ion signals.

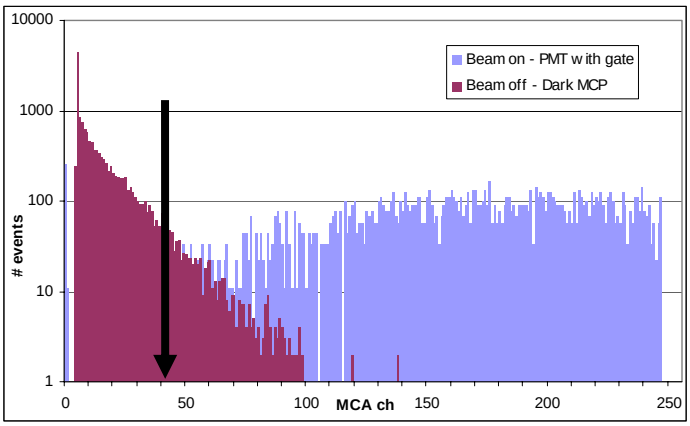

Fig. 7.29 Acquired spectra with beam off (violet) and with beam on and PMT signal diode-gated (blue); V_{MCP} = 5 kV.

We also performed a study of the light pulses on the final position sensor, analyzing possible differences between pulses from MCP dark signals and heavy ion events. Each luminous spot in the linear sensor has a Gaussian shape, characterized by the amplitude (height) and the area (weight). The software interface allows one to select the minimum amplitude and area of the peaks.

In fig. 7.30 we show the distributions of height and weight of signals for MCP dark counts (beam-off) and for heavy ion induced signals (beam-on). The two distributions are not normalized and the acquisitions have different thresholds: the dark counts were

acquired if height and weight were both greater than 8 arbitrary units (a.u.); the beam-on acquisition required height > 14 a.u. and weight > 16 a.u.. The dark counts present in beam-on acquisition are not numerous. Indeed the beam-off acquisition was taken with the intention of populating the distribution. It is clear that a very clean separation between dark count events and ion events can be obtained by applying an oblique cut.

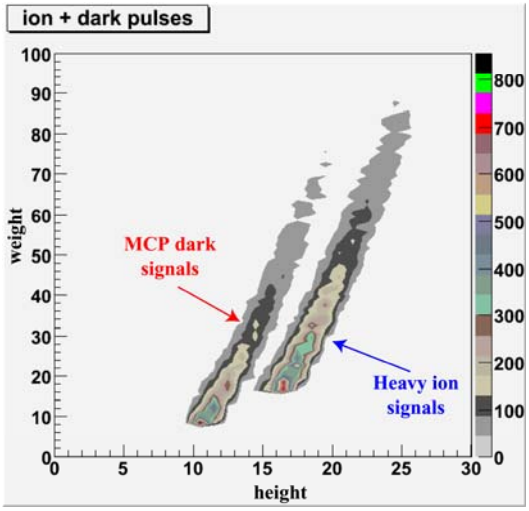

Fig. 7.30 Distributions of height and weight of tracked peaks onto the linear sensor.

8. SEU studies with the SIRAD IEEM

8.1 The SDRAM system

8.1.1 Introduction

In the previous chapters I described the SIRAD Ion Electron Emission Microscope and some of the first experiments we performed the in axial configuration: the time-resolved images of grids and a preliminary efficiency measurement.

More recently we also performed a true Single Event Upset experiment with IEEM technique using a Commercial Off The Shelf (COTS) Synchronous-DRAM (SDRAM). This important and complex work was carried out in collaboration with colleagues of the Department of Electronic Engineering of the University of Rome "Tor Vergata".

This work will be discussed in this chapter. After reviewing the SDRAM-based test system, I will describe the experiment we performed and discuss the results.

8.1.2 A calibration tool for the IEEM

Last generation SDRAM devices contain a large regular array of small cells with sub micrometric feature size (cell area ~ 10μm^2, feature size ~ 0.1μm). The low LET threshold (LET_{th} ~ 1 MeV·cm^2/mg), a relatively high value of the plateau cross section (CS_P ~ 10^{-9} cm^2/bit) and the short access time to verify SEU make these devices good candidates for our first true IEEM experiment.

The database of the ion impacts reconstructed by the IEEM can be compared with the knowledge of the SDRAM layout structure information to verify the IEEM performance. The small feature size of the memory cell and the high regularity of the array allows one

to extract the lateral resolution of the IEEM. In addition we can evaluate the ion impact reconstruction efficiency of the IEEM.

The tests have been performed on a Micron 256 Mb MT48LC64M4A2Y96A SDRAM. Devices were not enclosed in their package, but directly bounded onto suitable carriers as shown in fig. 8.1.

In the physical implementation of the SEU experiment the restriction due to the vacuum environment was considered. In particular dissipation of heat and out-gassing problems have been addressed with an appropriate methodology.

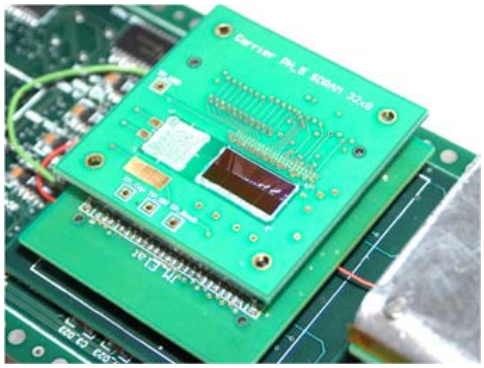

Fig. 8.1 Micron 256 Mb SDRAM device.

8.1.3 SDRAM system description

The 256Mb SDRAM is a high-speed CMOS dynamic random-access memory that contains 268,435,456 bits. It is internally configured as a quad-bank DRAM with a synchronous interface. Each of the 4 banks is organized into 8,192 rows by 1,024 columns of 8 bits. The SDRAM is designed to operate in 3.3V memory systems and all inputs and outputs are LVTTL-compatible.

In order that the SDRAM based test system match the mechanical constraints imposed by the IEEM environment, a custom Test Board (TB) has been implemented. To obtain maximum readout speed using the advanced input-output features of the SDRAM (burst mode, self refresh, etc.), the TB is based on a high performance 40 MHz Field Programmable Gate Array (FPGA) (see fig. 8.2). The system core mapped in the FPGA is able to:

- address each cell;
- perform read and write operations;
- refresh the cells (normally every 50 ms) .

Beside these basic operations, the FPGA-based system performs complex test procedures as:

- write an internally generated pattern on blocks of cells;
- read a block of cells;
- compare a block of cells.

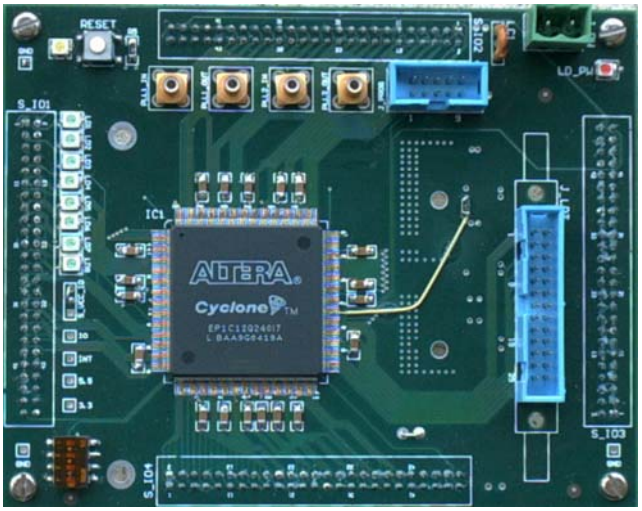

Fig. 8.2 Altera Cyclone EP1C12Q24017N FPGA.

The SEU-test system consists of two identical memories: a device exposed to radiation (Hot DUT) and an unexposed reference device (Cold DUT). At the beginning of test procedures, a common pattern is written in both the DUTs. After the writing operation, some errors are randomly written in the Hot DUT and the device undergoes a preliminary test routine to verify the write operation and to count the number of errors at the beginning of the test. After irradiation, the contents of the two memories are read and the cell status of the Hot DUT is then compared with the corresponding contents of the Cold DUT. If a difference (i.e. an Upset in the cell memory) is detected, the results of the compare operation (row, column and flipped bit) are stored in a FIFO. This procedure is

repeated until the whole memory has been read; the SDRAM is then loaded with the correct pattern and the comparison procedure starts again (fig. 8.3).

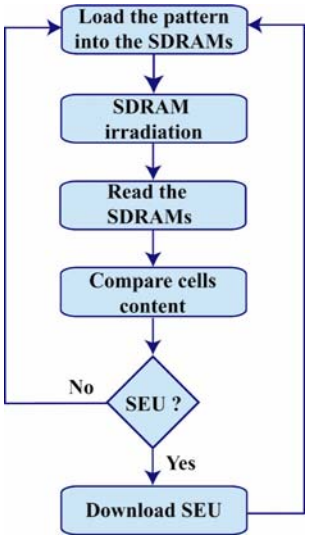

Fig. 8.3 SDRAM SEU experiment flow chart.

A compression procedure is then performed in order to minimize the amount of data to be transmitted to the Test Control PC (TCPC). The communication between the TB and TCPC is obtained by a TCP-IP Client-Server scheme (which allows TCPC to remotely drive the test). Test supervisor and TCP-IP data communication are handled by a microprocessor on the TB. Using this configuration the time required to read the whole memory is:

$$(8.1)\quad t_{SDRAM} = 64 \cdot 10^6 byte \cdot 25ns \cong 1.6\,\text{sec}$$

Two things should be noticed as they will be discussed at the end of this chapter:

- the readout time could be drastically reduced if we were able to read only the cells in the IEEM exposed area (which is ~1/4000 of the entire SDRAM surface); in this case the irradiated area could be scanned in:

$$(8.2)\quad t_{FOV} = 1.6\,\text{sec}/\,4000 \cong 0.4ms\,;$$

- an extra overhead time, proportional to the number of detected SEU, is needed to transmit results to the TCPC and this time may not be negligible.

Preliminary measurements of the SEU cross section with broad beam have been performed at SIRAD [81]. In order to prevent pileup of SEU and to monitor Single Event Functional Interrupt (SEFI) [82], [83] the DUT irradiation was split into several steps in order to have few hundred of SEU for each scan of the whole memory array. The results are reported in the table 8.1:

Ion species	LET	Fluence	CS
220 MeV ^{58}Ni	27.9 MeV·cm^2·mg^{-1}	156000	$(4.0 \pm 2.0)\cdot10^{-9}$ cm^2/bit
158 MeV ^{28}Si	8.6 MeV·cm^2·mg^{-1}	584630	$(1.8 \pm 0.4)\cdot10^{-9}$ cm^2/bit

Tab. 8.1 SEU cross section measurements for Micron 256 Mb MT48LC64M4A2Y96A SDRAM .

8.1.4 Mapping SDRAM with a laser

One of the aims of the IEEM experiment with SDRAM was to get a quantitative measure of the effective resolution of the IEEM. For this purpose, we needed to compare the distribution of SEU in the memory cells of the Hot DUT with the map of the ion hits reconstructed by the IEEM. The logical addresses of the SDRAM should be converted into the physical positions of the cells. Unfortunately, the manufacturer did not provide the physical layout of the SDRAM. To obtain the physical map of logical addresses, we implemented a mapping system based on a laser (fig. 8.4). Using the laser we induce the creation of electron-hole pairs in the cells and charge is collected until the status of the bit flips, simulating a SEU.

Our laser test bench was based on an infrared (1060 nm) laser for which the absorption coefficient is small enough to allow the laser to cross the whole device. The SDRAM was fixed on a 2-axis micrometric translation stage and illuminated by the laser via fiber optics. In order to illuminate a very small spot on the memory, we used the smallest fiber

optic output available (~ 5 μm). We did not focus the laser beam but moved the fiber optic output as close as possible to the device surface.

Laser irradiations from the frontside are difficult due to the opacity of the metal layers present on the device. Normally laser backside irradiation is used as it gives access to the whole device, but this approach requires a backside opening through the package. Our SDRAM is bare but backside irradiation was not performed due to difficulties in realizing an opening through the carrier board.

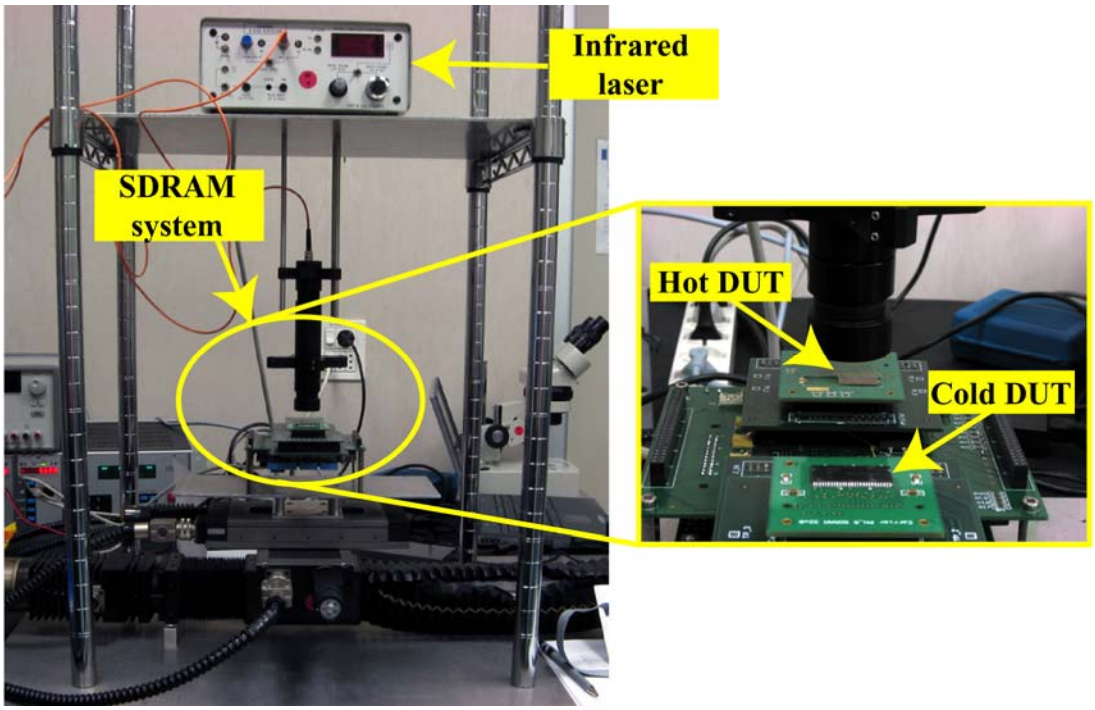

Fig. 8.4 Setup for laser-based system for SDRAM mapping.

As already mentioned, the content of the cells is normally refreshed every 50 ms. As we are irradiating through the metallization layers of the front-side, the laser is *not* able to generate enough charge to change the logic condition of the memory cells in such a short time interval. However the refresh time value can be set, and even completely suppressed, via software. The experiment was based on the Bit Retention Time (BRT), the time the information is retained in the memory cell without refresh. This approach is based on the observation that on a given device there is dispersion of the BRT among the cells. We inhibit cell refresh and as the laser irradiation progresses there is a gradual

increase of the number of memory cells that do not maintain their initialization value mimicking a SEU (the laser induced degradation of the information written in the cells will appear first in those having worst electrical characteristics).

After precisely positioning SDRAM using a micrometric translation stage, we started the mapping procedure by writing the common pattern (0000 0000) on the two memories. The reason why I specify this initial written pattern will be clarified in the following part of this paragraph.

With the refresh time suppressed, the Hot DUT is irradiated by laser for some seconds; after the memory reading and the errors download, the SDRAM is moved to another position and the mapping procedure is repeated. The SDRAM is systematically scanned until we obtain the correspondence between the logical addresses of the flipped cells and the physical positions of the same cells in the memory.

After reconstructing the SDRAM physical layout, we noticed the lack of some bit lines. A memory cell consists of a capacitor; when the capacitor is charged (obviously it is a threshold phenomenon), the corresponding logic state of the cell is “1”; when the capacitor is discharged, the logic state of the cell is “0”. This is the reason why the initially chosen pattern to be written was “0000 0000”: before irradiation every cell is discharged and the collection of laser-induced charge makes the cell flip from the logic state “0” to the logic state “1”. In a memory layout it is common to implement some cells with a “negative logic”: if the logic state to be written is “0”, an inverter preceding the cell causes the capacitor to be charged. In this case, the memory cell is already charged before irradiation and a further charge collection does not change its logical condition. To verify this hypothesis, we wrote the pattern “1111 1111” into the Hot DUT and proceeded to the laser irradiation. As expected, the previously lacking bit lines were now those which flipped.

8.1.5 SDRAM physical layout

From a logic point of view, the SDRAM has four banks, each of which organized as 8,192 rows by 1,024 columns by 8 bits. From the physical point of view, the SDRAM is microscopically divided into eight quadrants (fig. 8.5):

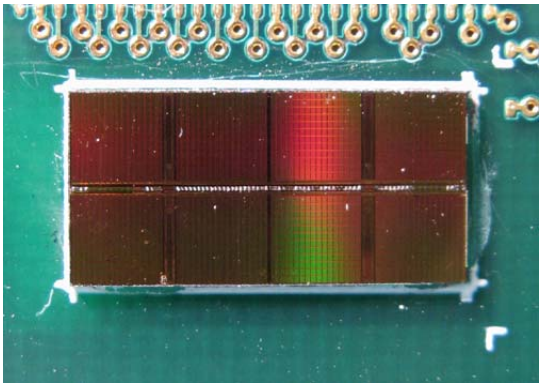

Fig. 8.5 Bare SDRAM (no bonding wires in the photo).

Fig. 8.6 shows where the four banks are positioned and how the eight bits are distributed inside every bank.

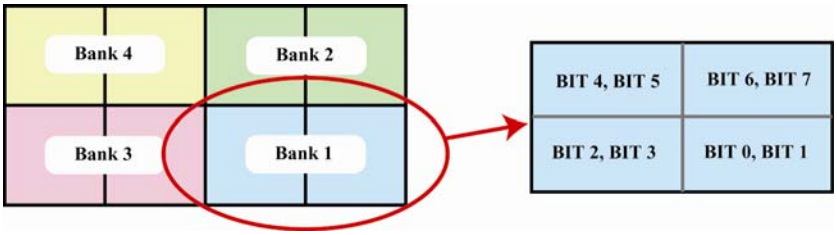

Fig. 8.6 Arrangement of the four banks in the SDRAM and of the eight bits inside every bank.

Every quadrant in turn consists of an array of 16 × 12 little sectors (fig. 8.7), as pictured in fig. 8.8

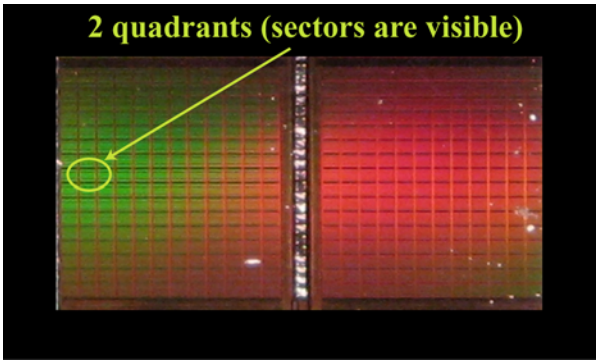

Fig. 8.7 **The picture shows two macroscopic quadrants and the array of 192 (16 × 12) sectors.**

which also shows the row and column addresses disposition:

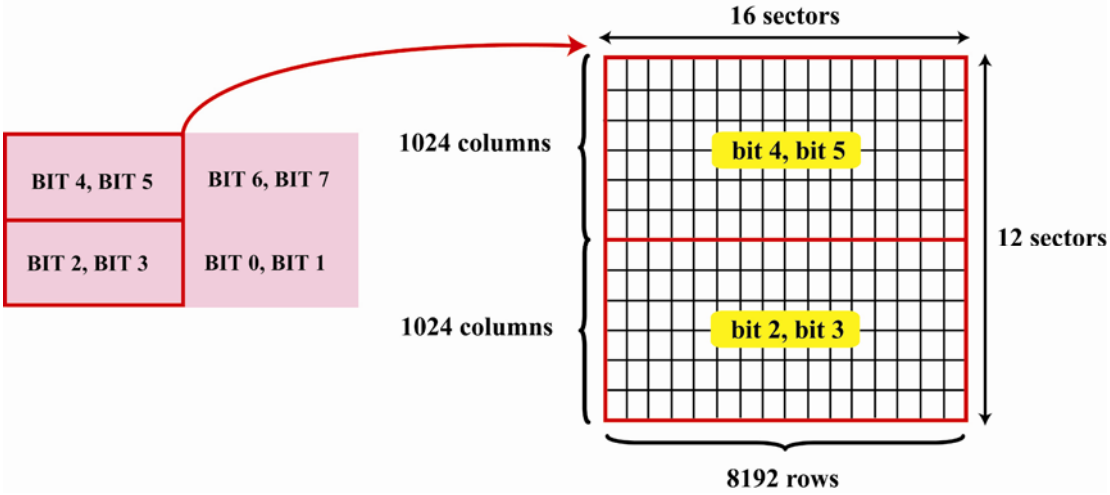

Fig. 8.8 **Global arrangement of column and row lines inside every macroscopic quadrant.**

In every quadrant, the *rows* are distributed in 16 blocks (one for each sector) of 512 addresses (16·512 = 8192); inside each sector the addresses are consecutive, as schematically drawn in fig. 8.9.

16 sectors **512 addresses for sector**

0	*1*	*2*	*3*	*4*	*5*	*6*	*7*	*8*	*9*	*10*	*11*	*12*	*13*	*14*	*15*
7680 ÷ 8191	5632 ÷ 6143	6656 ÷ 7167	4608 ÷ 5119	7168 ÷ 7679	5120 ÷ 5631	6144 ÷ 6655	4096 ÷ 4607	3584 ÷ 4095	1536 ÷ 2047	2560 ÷ 3071	1023 ÷ 512	3072 ÷ 3583	1024 ÷ 1535	2048 ÷ 2559	0 ÷ 511

TOTAL: 8192 row addresses

Fig. 8.9 **Row addresses distribution.**

On the contrary, the number of *column* addresses inside each sector is not always the same, but can assume two values: 168 or 176 (in particular, 4·168 + 2·176 = 1024 column addresses, see fig 8.8). The 168 (176) column addresses in every sector are not exactly in sequence. I report in fig. 8.10 the column address lines of a couple of sectors, as examples.

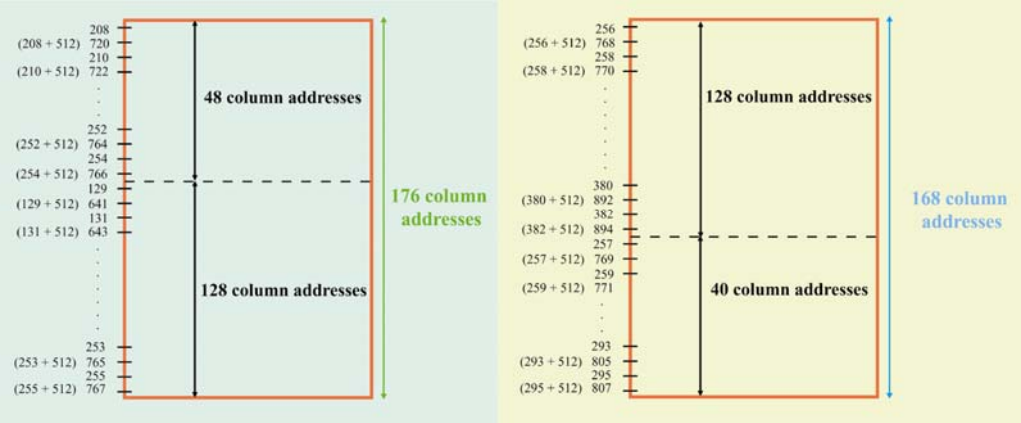

Fig. 8.10 Example of column addresses distributions for two sectors.

We also need to know the physical dimensions of the sectors and quadrants composing the SDRAM. We performed careful measurements (fig. 8.11). With the knowledge of the spatial dimensions of the sectors and the number of contained cells, we estimated the pitch between cells: ~0.667 µm between adjacent columns and ~0.170 µm between adjacent rows.

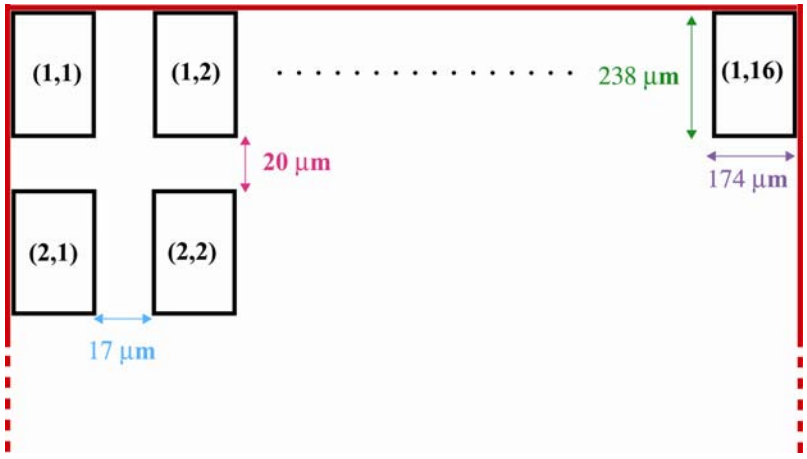

Fig. 8.11 Physical dimensions of SDRAM.

This gives us the knowledge of the exact positions of memory cells, once the logical address (bank, row, column, data) is provided.

Some uncertainties still remain. For example, we do not know where the first row (column) is exactly positioned inside the sector; in our model, we assumed no gap (see fig. 8.12) between the edge of the sector and the first memory cell.

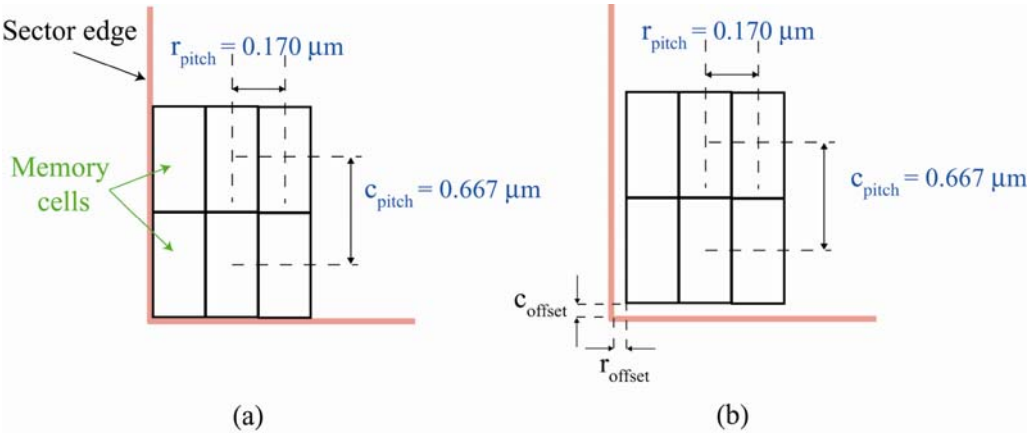

Fig. 8.12 Two possible configurations for cells positioning inside a sector. In (a), we assume no gaps between the sector edges and the cells; in (b) the gaps ($c_{offeset}$ and r_{offset}) are present.

This assumption obviously introduces an error, whose entity is (in general) not negligible; in our applications, however, more relevant causes of error will be present and this one can be ignored.

8.2 SEU experiment

8.2.1 Experimental challenges

Once the physical layout of the SDRAM is known the SEU experiment with IEEM can be performed. Both the IEEM and the SDRAM-based SEU test systems are complex and making them working together was not straightforward.

Inside the experimental chamber, the environmental conditions for the SDRAM were harsh. Due to mechanical constraints only the board carrying the SDRAM itself and the diode for dosimetry could be kept on the sample holder. All the remaining part of the

DAQ electronics had to be fixed on the support for the linear stages 10 centimeters away from the DUT board. The electrical connections between the two parts have been carefully designed and implemented, to avoid degrading the fast signals from the FPGA board to the SDRAM due to the long transmission distance.

The device had also to work and to survive at a distance of only few (4-5) millimeters from a very intense high voltage. Any irregularity on the surface exposed to the IEEM electrical field could cause disruptive discharges with the consequent loss not only of the DUT itself, but, more seriously, of the whole DAQ system. The target surface should also be as flat as possible to prevent distortions of the electrical field of the microscope.

Before ion beam irradiation, IEEM setup is always performed with UV photons on a copper grid. For the moment this procedure is the only one available to position the target and to focus the IEEM and set the desired FOV. In these preliminary phases of IEEM experiments we image the calibration targets with a conventional CCD camera. Once the IEEM is set, the vacuum chamber should not be opened anymore. As the sample holder lies on the drawer, once the chamber is opened and closed again the sample holder will not return to the exact same position as before and the IEEM settings are no longer suitable. For this reason the calibration grid must hence lie on the same sample holder as the device under test. During the calibration procedure we had to protect the SDRAM and the whole DAQ system inside the chamber from direct exposure to UV to avoid fatal charging.

8.2.2 Sample preparation

In the light of the discussion of the last paragraph, it should be clear how the careful preparation of the sample is a critical issue. For the experiment, we need a complex target which should contain the SDRAM with the superimposed gold/Si_3N_4 membrane, at least one copper grid for setting the IEEM and a PIN diode for dosimetry (adjusting ion flux). The diode and the SDRAM are on the same carrier board. A further support (to be superimposed to the SDRAM carrier) for the golden membrane and for the grid is then required. As this support will be directly exposed to the IEEM extraction voltage (10÷15

kV), its surface must be very smooth to avoid discharges. To minimize PEEM extraction field distortion, maximum flatness should be granted. A cavity was milled to lodge the copper grid and minimize protrusions. We also added a large hole to allow a laser beam to pass through (in case there was a need to realign the IEEM chamber).

As already mentioned in par. 7.1.3, the area of the thin membrane that emits is only the central region of 1×1 mm^2. To aim at this zone with the IEEM we measured the relative position respect to an easily recognized reference point in the target. For this purpose we took advantage of a four-quadrant mixed-pitch copper grid (fig. 8.13): the central point of this grid is easily recognized by a visual inspection with a conventional CCD camera.

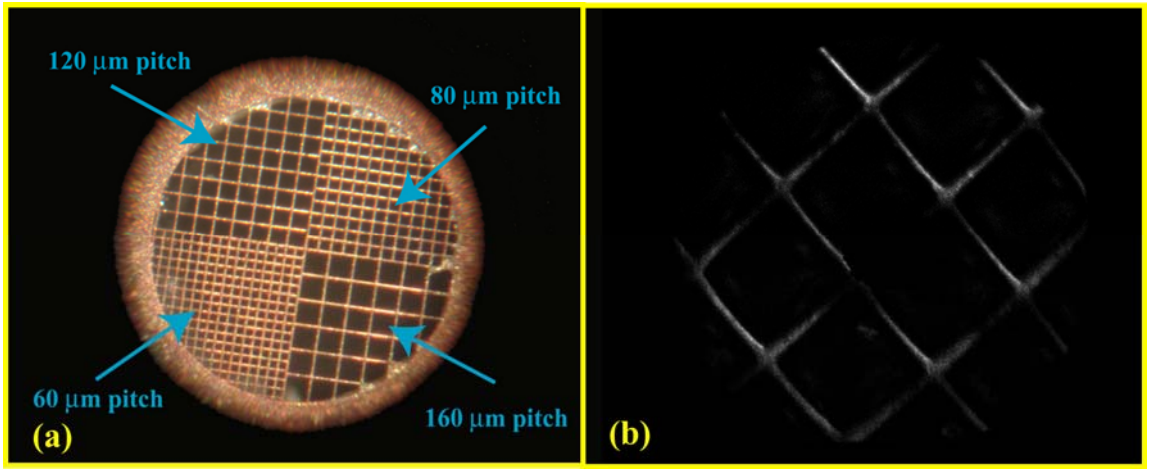

Fig. 8.13 Optical microscope picture of the mixed-pitch grid with dimensions (a) and UV induced image of the grid (the framed FOV is ~ 200 µm) reconstructed by IEEM sensor (b).

We used two mixed-pitched copper grids, on opposite sides of the gold membrane. Before target installation, the relative positions of the two center points of the grids and the central area of the window have been carefully measured. During IEEM setup with UV, we obtained the absolute positions of the two grids and hence the exact position of the central part of the membrane. We chose to use two grids instead of only one because, after installation inside the chamber, the target might be slightly rotated. The positioning will be easier with two grids because the rotation angle is immediately apparent and can be compensated for.

From previous tests, we learned that the best quality images of copper grids are obtained when nothing is behind them; i.e. when they do not lie on a substrate. For this reason, the SDRAM carrier was modified to include two small apertures in correspondence to the locations of the two grids. A larger hole for the laser beam was also added (fig. 8.14).

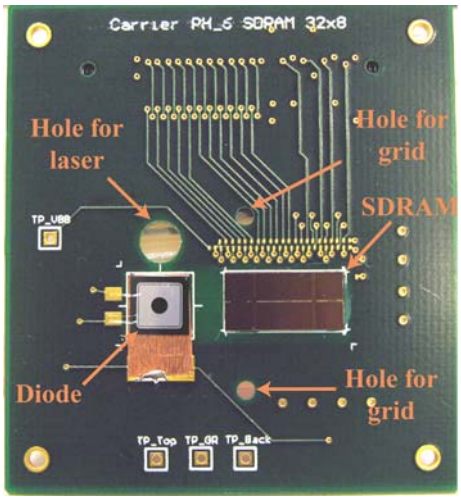

Fig. 8.14 Novel SDRAM carrier board.

The distance from the SDRAM surface and the gold membrane should be kept as short as possible to minimize the projection lever arm of multiple scattering. To reduce the distance, the bonding wires from the memory onto the carrier was made as flat as possible.

To protect the SDRAM from the direct UV exposure, a remote-controlled motorized sliding window system has been implemented. When the UV lamp is on the window must be shut. During the calibration phase, the shut window protects the DUT against any possible discharge.

In fig. 8.15 a photo of the developed target is shown:

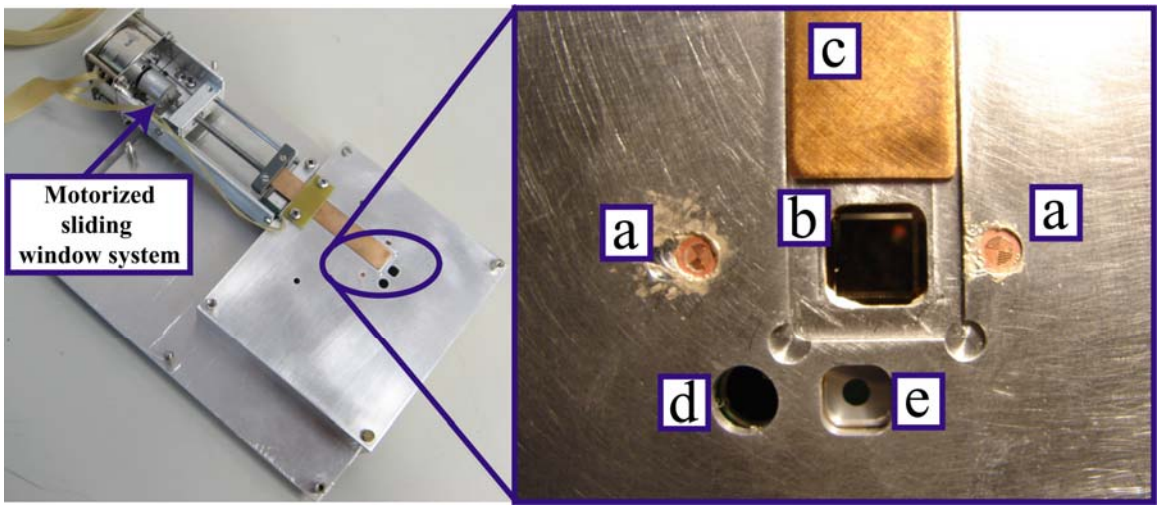

Fig. 8.15 Prepared target for the SEU experiment on the left, with a zoomed view on the right, showing: (a) grids; (b) golden membrane; (c) sliding window; (d) hole for laser; (e) PIN diode.

8.2.3 Synchronization with IEEM

To associate the events reconstructed by the IEEM with the upsets in the SDRAM, we need a synchronization procedure.

The trigger from PMT described in the previous chapter may be used in those situations where the SEE in the DUT are immediately detectable, e.g. single event gate ruptures or burnouts (SEGR, SEB); single event latchups (SEL) in CMOS devices. In our case the SDRAM must be read-out before ascertaining the occurrence of a SEU.

In the IEEM, data sent from the detector firmware arrives as a series of properties of the detected peaks; i.e. the corresponding axis (X or Y), height, width, weight, position, etc. Thanks to the time stamp system, every peak is uniquely labeled with a number that corresponds to the progressive position of the pixel where the peak has been found to start. The first pixel of first frame has timestamp 0, the first pixel of second frame has timestamp 256, and so on. Thus, the timestamp indicates both pixel acquisition time and the spatial position; i.e. the spatial position is obtained univocally by the pixel timestamp modulus the sensor frame size (256 pixels in our case), while the acquisition time (which the information we need for synchronization with an external DUT) is the integer part of the ratio of the timestamp with the sensor frame size. Every event is therefore temporally

identified by the progressive number of scanned frame and the frame counter is reset at the beginning of every new acquisition. A signal with a rising edge in correspondence of each frame is sent to the external user and used as a common clock (master clock) to time-stamp both IEEM events and DUT operations. Together with the frame-counter signal, two more signals are sent to the SDRAM system: the “START” command (corresponding to the beginning of a new IEEM acquisition) and a “RESET” command (corresponding to the end of a IEEM acquisition). When the START command arrives, the SDRAD DAQ starts its internal counter on the frame-clock, which is incremented at every clock (frame) signal; every SDRAM acquisition is labeled by the value assumed by the counter at the beginning of the acquisition itself. The counter is reset in correspondence of the RESET command. The time-stamped SEU events are then compared with the data base of the detected IEEM events and the correlation is done.

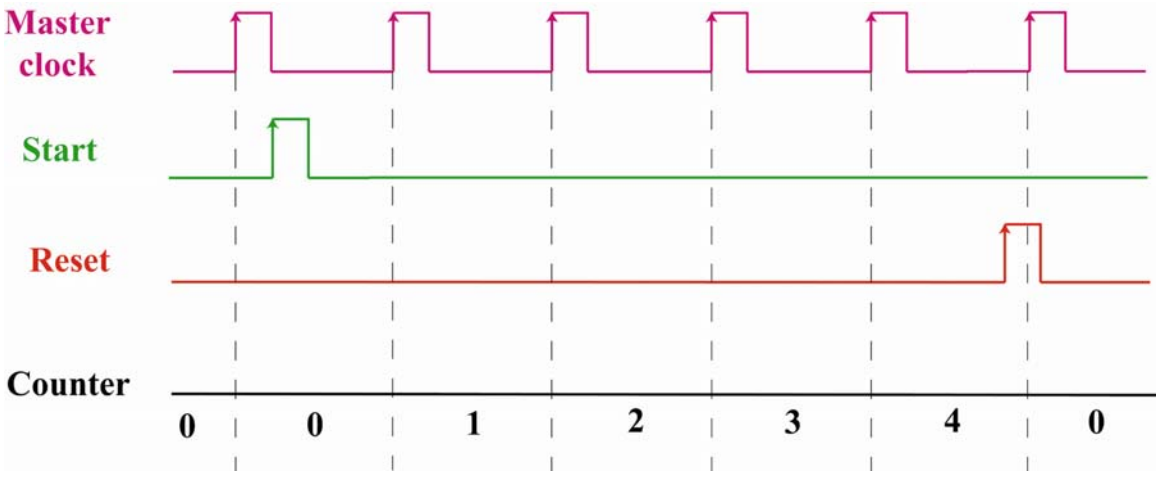

Fig. 8.16 Synchronization signals.

8.2.4 Ion beam shutter

Before describing the experiment, it is necessary to recall briefly how the SEU test is performed. At the beginning of the procedure, a chosen pattern is written into the memory and the device is ready for irradiation. After the exposure to the beam, the SDRAM is readout and compared to the Cold DUT; the start time for reading and comparing tasks can be set via software and depends on the duration of the irradiation.

During this interval of time, the SDRAM remains in a “waiting” status and no tasks are performed. The last step is the download to the control PC of the detected SEU events on the memory cells. To avoid fake SEU detection, the SDRAM should be irradiated only when it is in the “waiting” status.

We developed a way to protect the memory array from irradiation when it is in reading, writing and downloading phase. To select the proper time for irradiation, we implemented a fast beam-shutter installed in the irradiation chamber 2 meters before IEEM (fig. 8.17). The rising step of a TTL signal opens the shutter; this signal is driven by the SDRAM itself and corresponds (almost) to the start of the “waiting” status of the DUT. The duration of the signal sets the interval of time during which the shutter remains open to allow the ions to hit the target. The length of this interval is tuned depending on the ion flux on the target and on the number of expected SEU in the Hot DUT.

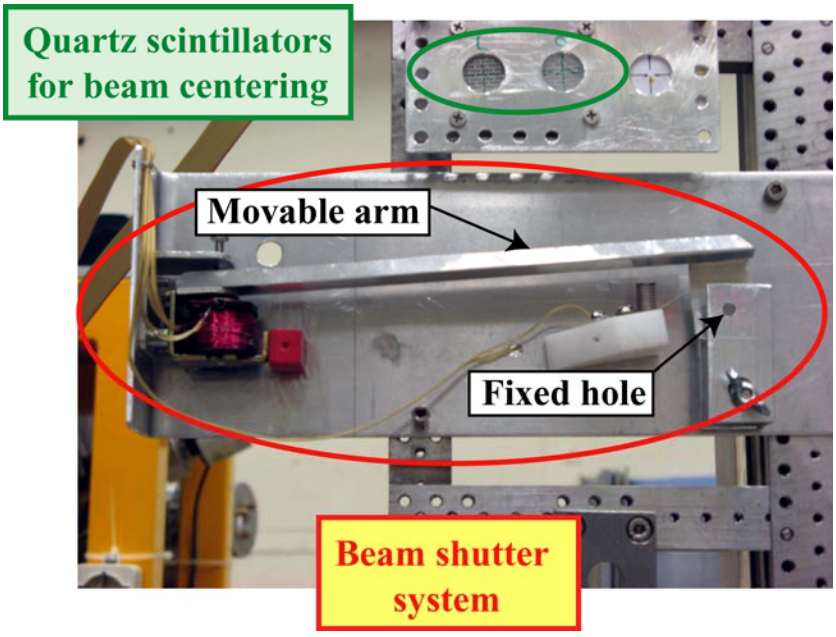

Fig. 8.17 Fast beam-shutter system. On the right the fixed hole for the beam is visible; another hole in the movable arm is put in correspondence of the fixed one for the desired time length, according to the “waiting” status of SDRAM. On the upper part of the picture, two quartz scintillators (a polished one and a dull one) for beam detections placed on the same sample holder.

8.2.5 SEU experiment

The experiment was performed with a beam of ^{79}Br at the energy of 214 MeV, the energy of the most probable charge state with the Tandem voltage of 13 MV. The focused beam was first detected on the extractable faraday cup and then sent onto the polished quartz scintillator of fig. 8.17.

On the IEEM sample holder one of the two grids was positioned in front of the IEEM and the beam was sent with the fast shutter off-beam (so that the ions were not blocked) and the ion-induced image of the copper grid was reconstructed. As expected, the image was not complete. Most of the incompleteness was due to the presence of the earth magnetic field which we compensated with the aid of an external permanent magnet (fig. 8.18). We could never succeeded in filling the whole FOV with the copper image and the one shown in fig. 8.18 is the best result we obtained.[1]

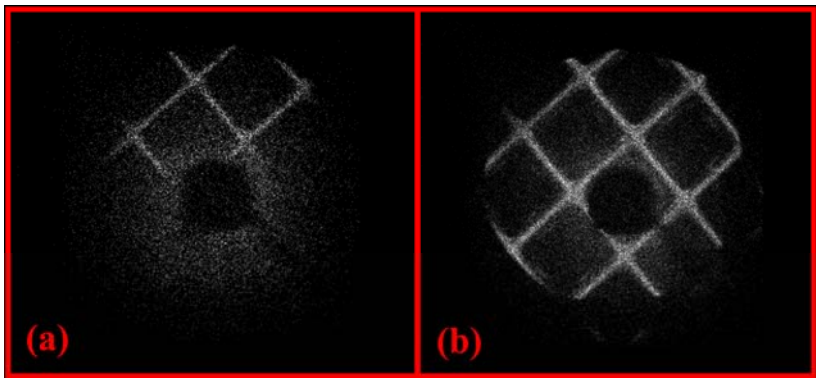

Fig. 8.18 Ion induced image of the copper grid before (a) and after (b) the earth magnetic field compensation.

After defocusing the beam, PIN diode was positioned in front of the IEEM and the ion flux was adjusted to ~50 ions/s in through the aperture of the IEEM (~ 1.6×10^5 ions/sec·cm^2). The SDRAM with the gold membrane and the beam shutter were then taken to the respective irradiation positions.

[1] The residual incompleteness was probably due to tilt. At the moment the tip-tilt stages were not working.

When the software of both the SDRAM SEU-detection and the IEEM DAQ were started, the master clock and the START signal were sent to the SDRAM DAQ. After the initial test routines, the SDRAM DAQ records the counter value (which identifies each "shot") and is then ready for irradiation; it sends the "open" command to the shutter and irradiation starts. We decided to keep the shutter opened for ~ 500ms in order to have only a few (~10) ions hitting the SDRAM for each shutter opening (shot). After irradiation, the memory array was readout and compared to the reference COLD DUT. Detected SEU were downloaded and the procedure started from the beginning.

The operation flow chart for the SEU experiment is slightly more complex (some more actions should be performed) than the one of fig. 8.3 and the updated block diagram is shown in fig. 8.19:

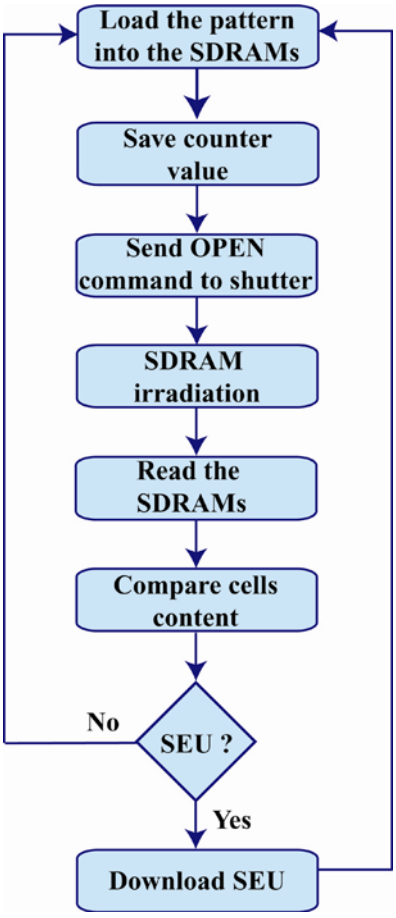

Fig. 8.19 Flow chart of operations performed by the SDRAM system during a SEU experiment.

8.3 Experimental data

8.3.1 SDRAM data

A typical log-data file for SDRAM system is shown in fig. 8.20. Every shot (corresponding to the opening of the fast beam shutter) is identified by the timestamp; i.e. by the value assumed in that moment by the frame counter (the counter based on the master clock). In the time the shutter remains opened, more than one ion hits the SDRAM. As the SEUs are not detected in real time, but only after the entire array is readout, we cannot associate a temporal coordinate to each upset.

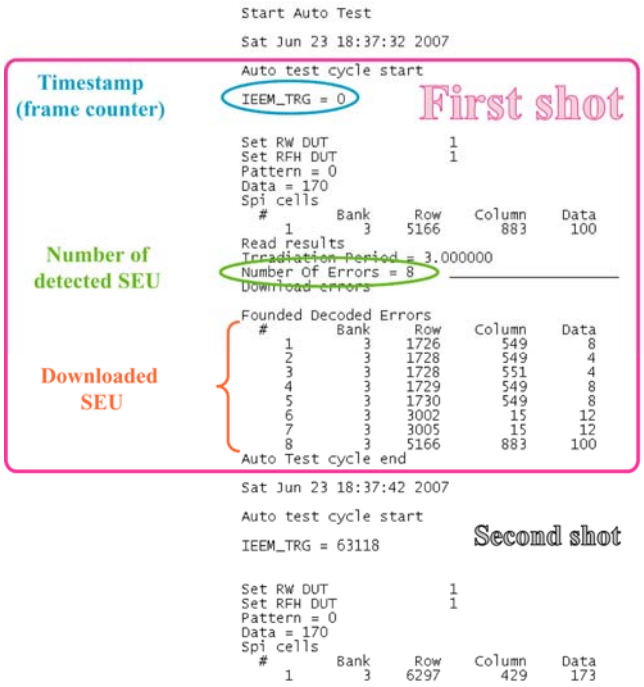

Fig. 8.20 Example of SDRAM logdata output file.

The irradiated SDRAM has a high SEU sensitivity, i.e. there is a high probability that an ion striking the array cells cause an upset. Taking into account the number of bits in the FOV of 200 μm:

$$(8.3)\quad bit_{FOV} = 1.2 \cdot 10^5$$

and the previously measured cross section:

$$(8.4)\quad \sigma_{SEU} = 1 \cdot 10^{-9}\ cm^2/bit,$$

the number of expected SEU for each ion is:

$$(8.5)\quad n \approx 1\ SEU/ion.$$

For the experiment the ion flux was set to a compromise value: to allow the collection of a large amount of data in a reasonable time it could not be too low, and to allow an easy data-analysis it could not be too high. We worked with an ion rate of ~40 impacts per second and set the opening time for the shutter at 500 ms: the estimated ion rate of ~20 impacts on the DUT per shot.

The number of detected SEU was systematically a factor 4 higher than the number of expected ions on the DUT; in fact, we realized that each striking ion causes multiple errors in the memory array ("clusters" of SEU). The ionized track created by the impinging particle is too narrow (< 100 nm) to explain this phenomenon. Instead this could be due to the diffusion of the electron-holes which are collected by the electrical fields of the nearby memory cells. It must be stressed that if we simply count the number of SEU, without taking into account their addresses, we could not recognize this clustering and this would introduce an error, for example in the calculation of the cross section. In fig. 8.21 we report the reconstructed physical map of flipped memory cells in one shot (identified by the trigger value) with a zoomed view of three ion impacts which caused SEU in several adjacent cells.

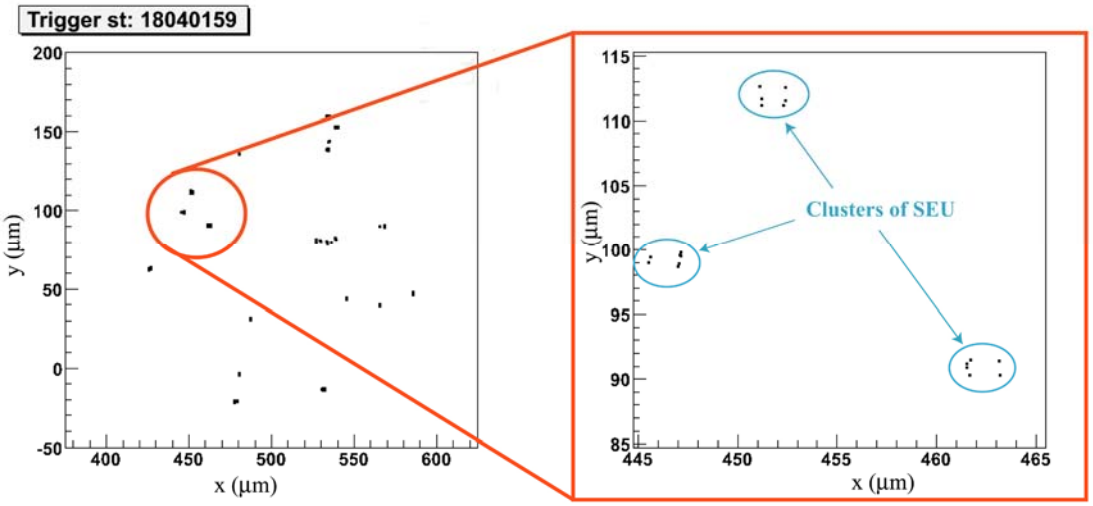

Fig. 8.21 Example of mapped SEU events on the SDRAM. On the right, a zoomed view shows clearly the existence of clusters of SEU in correspondence of a single ion hit.

Before the experiment, we set the proper values for the PEEM lenses by imaging the copper grids on the target. The gold/Si_3N_4 membrane is not at the same distance from the IEEM head as the grids, but ~ 1.1 mm deeper (more distant). This value is only an estimation based on the (known) membrane thickness and on the mechanical dimensions of the sample holder itself. To be sure the focalization is correct, we performed irradiations not only at the nominal distance but also with the target closer to the IEEM and farther away, up to ±300 µm, in steps of 150 µm. The step value was chosen considering that a longitudinal displacement of 100 µm in depth is sufficient to defocus a previously focused image. This was ascertained by visual inspection using the conventional CCD camera. The correct position is the one that maximizes the correlation between SDRAM and IEEM events. For each irradiation we collected ~ 5000 events with the IEEM DAQ. In fig. 8.21 we report all the SEU detected in one longitudinal position.

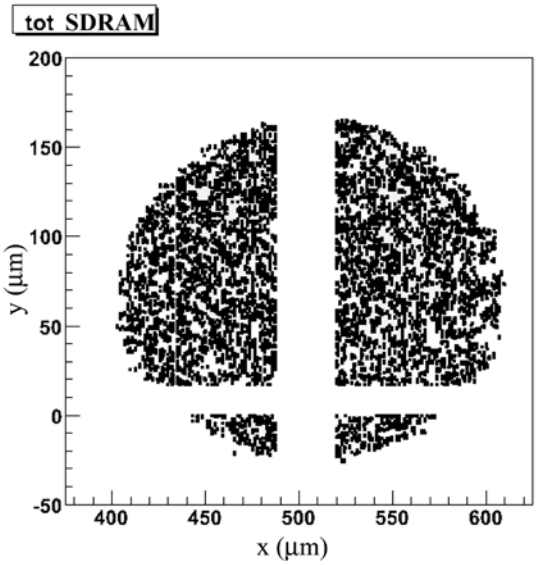

Fig. 8.22 Map of integrated SEU events for one irradiation.

The exposed area is, as expected, a circle of 200 m diameter and partially covers four sectors.

8.3.2 IEEM data

In the IEEM system the events are saved in a log-file that provides the following values:

- count (the progressive number of the event);
- timestamp;
- frame number;
- x position, y position;
- the height of the peaks;
- and two flags (one for each peak) that provide eventual warning conditions (out of range peak, peak acquired at the border of frame, too fat peak).

Figure 8.23 shows the image of all the IEEM events of the same irradiation session that produced the SDRAM events of fig. 8.22:

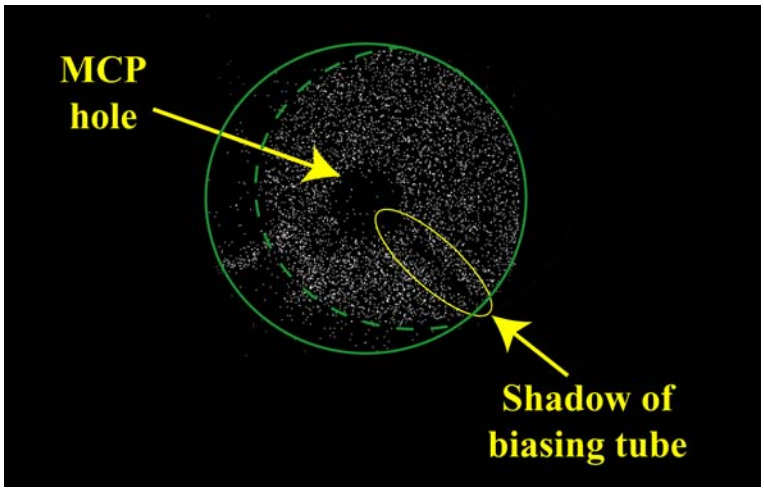

Fig. 8.23 Ion induced image of the golden membrane.

The image is not complete, despite of the external compensation of the magnetic field. Indeed the lost portion is larger than the one observed with the grid (for a comparison, see fig. 8.18) and its different position (left side instead of bottom-right side). The incompleteness might be due to a non-zero tilt angle and by the bulge on the membrane, both of which could not, at the time, be corrected for due to the lack of the angular motorized stage.

8.3.3 Data analysis

During each irradiation, the two systems collected the data separately; the comparison between the two events databases could be performed only at the end of the session. A special software was developed to be a semi-online analysis tool allowing us to verify the goodness of the collected data at the end of each irradiation session.

The first task to perform is the reconstruction of the “shots framework” of the two systems. While with the SDRAM system, the SDRAM data is acquired when the shutter is open and is hence immediately associated with a shot, the same is not true for the IEEM data. In fact the IEEM is free running; i.e. all the IEEM events are saved in one single list of data, without any distinction between shots. To correctly associate the two event databases, the procedure is to use the value of the frame-counter. Every series of data from the SDRAM system is labeled by the value of the frame counter at the

beginning of the "waiting" status of the DUT. For each shot, the corresponding events from the IEEM are those with a counter value between the value registered by the SDRAM system (the shutter is opened just afterwards) and a value which depends on the length of time the shutter remains open. The linear sensor is clocked at a rate of 3.125 MHz; this means that an entire frame (256 pixels) is read every ~ 82 μs. In 500 ms (the duration of shot during which the SDRAM is irradiated), we read ~ 6100 frames. For each shot, identified by the SDRAM recorded frame-counter value, the SEU events detected by the memory array are put in correspondence with the first 10,000 frames from IEEM system (see fig. 8.24). We chose to work with 10,000 > 6,100 frames to have a safety margin, as the duration of the shutter opening (shot) was not precisely measured. A few IEEM events are found outside the selected interval and are mainly MCP dark counts or ions hitting the target when the SDRAM is still in "write" mode.

A huge array is built by the analysis tool which stores, frame by frame, the incoming data from the two systems. The logical addresses of the detected SEU are then converted into the corresponding physical coordinates (expressed in microns). As every impinging ion causes multiple upsets, a weighting algorithm calculates the barycenter of the cluster that is taken as the position of the SDRAM-detected ion and is associated with the impact position reconstructed by the IEEM. In the calculation, we assume that all the upsets detected within a diameter of 3 μm are caused by the same ion. The probability that, in a single shot, two or more atoms hit the target at a distance < 3μm is very low (~ 0.2‰).

The x and y coordinates of an ion hit reconstructed by the IEEM have their own units, and the coordinates of ionic impacts must be scaled and shifted to match the impact map detected by the memory array.

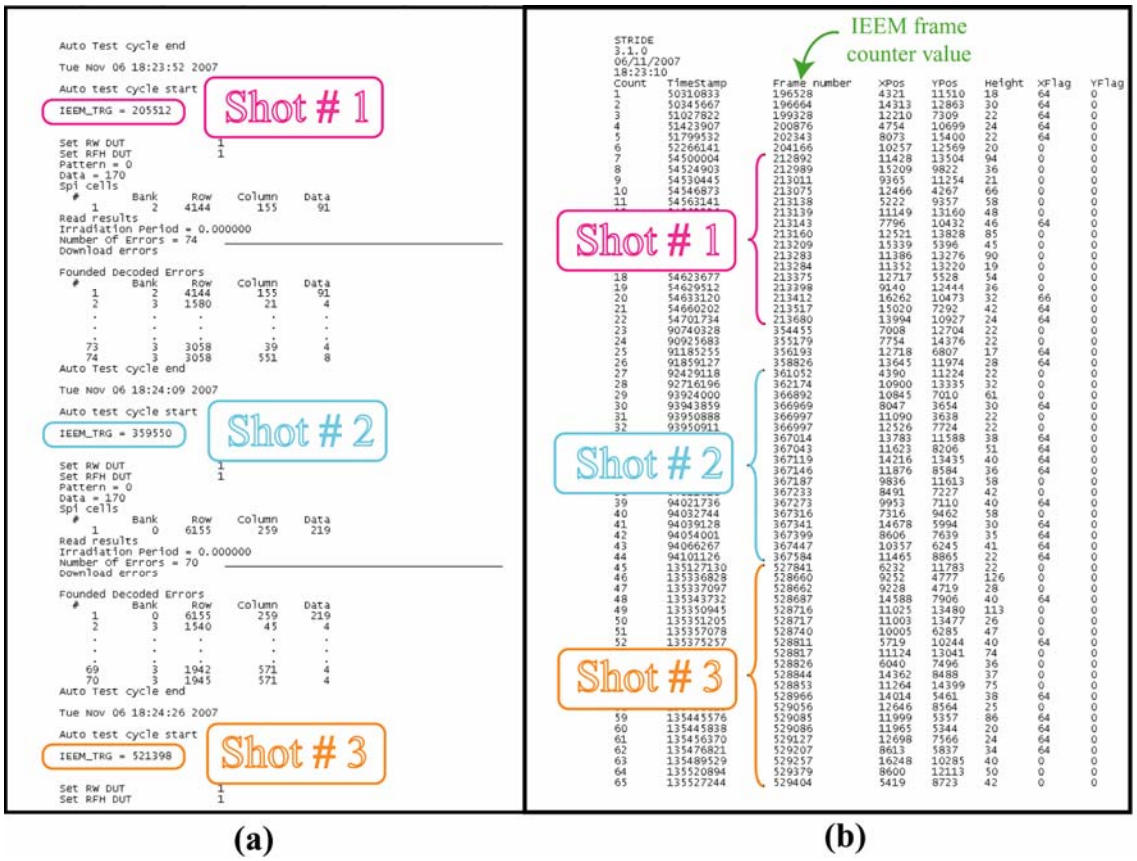

Fig. 8.24 Logdata of SDRAM (a) and of IEEM (b), with the association of events in shots.

This procedure was performed in steps, beginning with a rough superimposition based on the visual inspection of the spatial disposition of the two collections of events for each single shot. This allows one to set a preliminary value both for the scale factor and for the translation one. To verify the existence of correlation between the two groups of data, for each IEEM event we calculated the difference between its x (y) coordinate and the x (y) coordinate of all the SDRAM events. If there is no correlation, the obtained distribution would be smooth, roughly a very broad Gaussian. On the contrary, in presence of correlations, a sharp peak appears in the distribution (fig. 8.25):

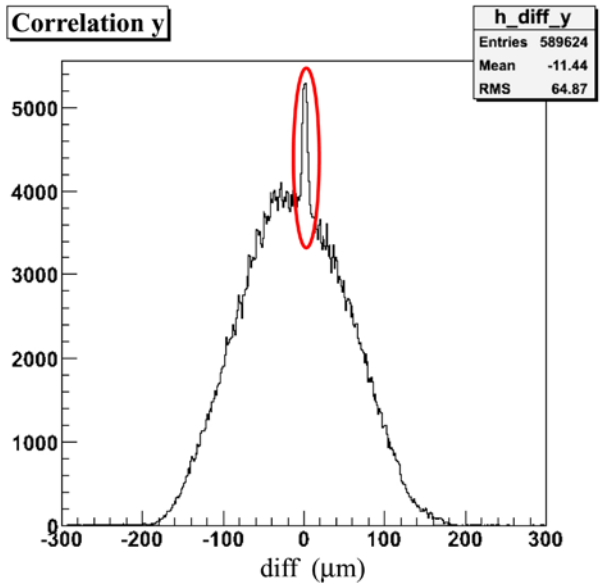

Fig. 8.25 Distribution of differences between each IEEM event and all the SDRAM ones. The red circle shows the peak due to the presence of correlated events.

A fine superimposition procedure is then performed that searches the values of the parameters (scale factor in x(y); shift in x (y); rotation) which minimize the width of the correlation peak and place it close to the zero position.

The fig. 8.26 shows the superimposition of the two maps of detected events, where the red points are the IEEM reconstructed impact points and the black squares indicate the flipped bits. Due to the presence of the MCP central hole, the shadow of the biasing tube and the incompleteness of the IEEM image for the tilt effect, a substantial part of the SDRAM exposed area is not covered by the IEEM. The SDRAM too has some “dead” regions (the gap between two adjacent sectors). In this case ion impact positions are detected by the microscope, but no information on the strike is provided by the memory array.

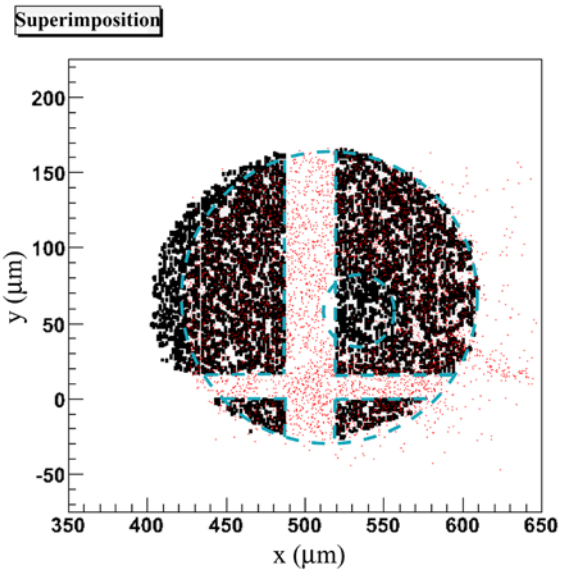

Fig. 8.26 Superimposed integrated maps: in red the ion impact positions reconstructed by the microscope, in black the memory cells where SEU errors were detected; the dotted blue lines mark the limits of the common sensitive areas .

The fig. 8.27 visualizes two maps of detected events referring to two shots. The black squares are the flipped memory cells and the red circles the events detected by the IEEM. The correspondence between some of the events is clearly evident.

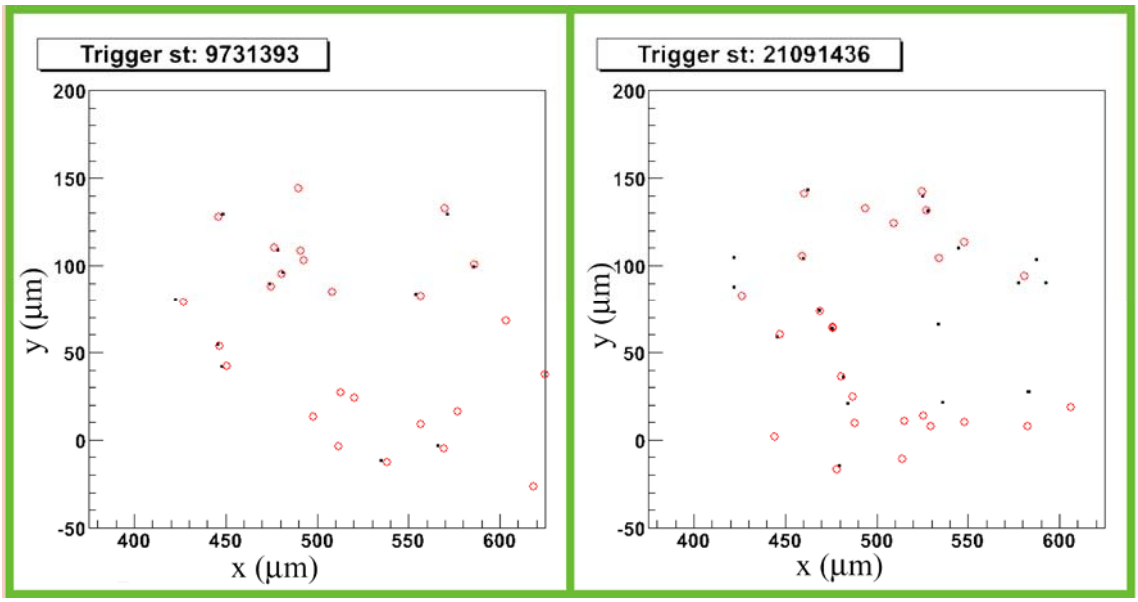

Fig. 8.27 Examples of shots showing both events from IEEM and by SDRAM.

8.3.4 Considerations on resolution

The histogram of fig. 8.25 represents the differences between y coordinates of IEEM events and SDRAM events. We report the same histogram in fig. 8.28, with a closer view of the emerging peak. As the peak represents only those events which are correlated, its spread gives a resolution estimation.

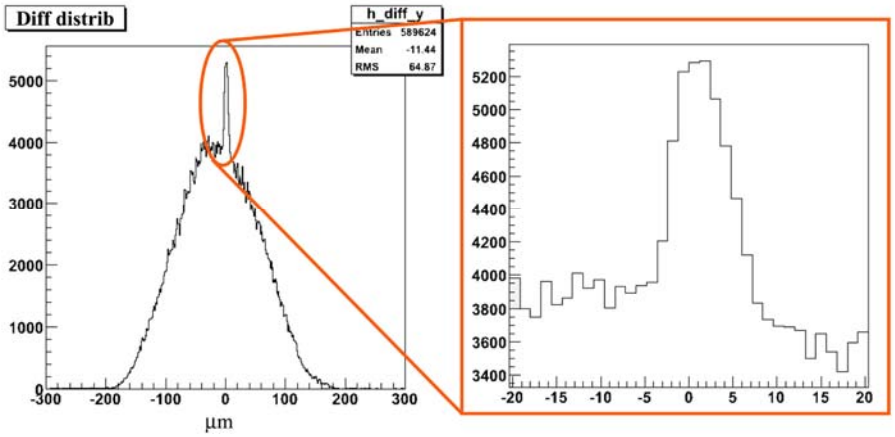

Fig. 8.28 Correlation peak emerging from the analysis of the differences of y coordinate of the two groups of data.

The peak, which is our "signal", is buried in a huge background, as the histogram includes all the events of the data sample. If we could select the correlated ones we would obtain a sharp Gaussian distribution. A selection was performed by considering only the IEEM events which are within a certain distance from the SDRAM ones. Fig. 8.28 reports the distribution of y-differences that result after cutting in the x-differences; the peak is now more evident. The FWHM of the signal peak is ~7 µm.

We know that the membrane induces distortions in the electrical field that extracts the secondary electrons, and that these distortions degrade the image and the lateral resolution of the IEEM. A quantitative evaluation of these distortions has not yet been made. As the gold membrane is uniform and has no recognizable features, no information about the spatial distortion of the can be obtained by simple imaging. Instead the SDRAM system provides a direct tool to localize with high precision the impact positions of impinging ions by comparing the two events databases: the one from the SDRAM,

giving the real impact positions, and the one from the IEEM. If we had a large amount of data, we could divide the irradiated area into a fine grid, calculate for each sector the deviations of IEEM positions from the real ones, and correct for them over the whole field of view. With the available data, even with a very rough grid (40 × 40), we have too few events (~ 2-3) for each element of the grid for an effective correction. To be able obtain a more statistics in a reasonable quantity of time an important upgrade of the SDRAM DAQ is required (see paragraph 8.4.2).

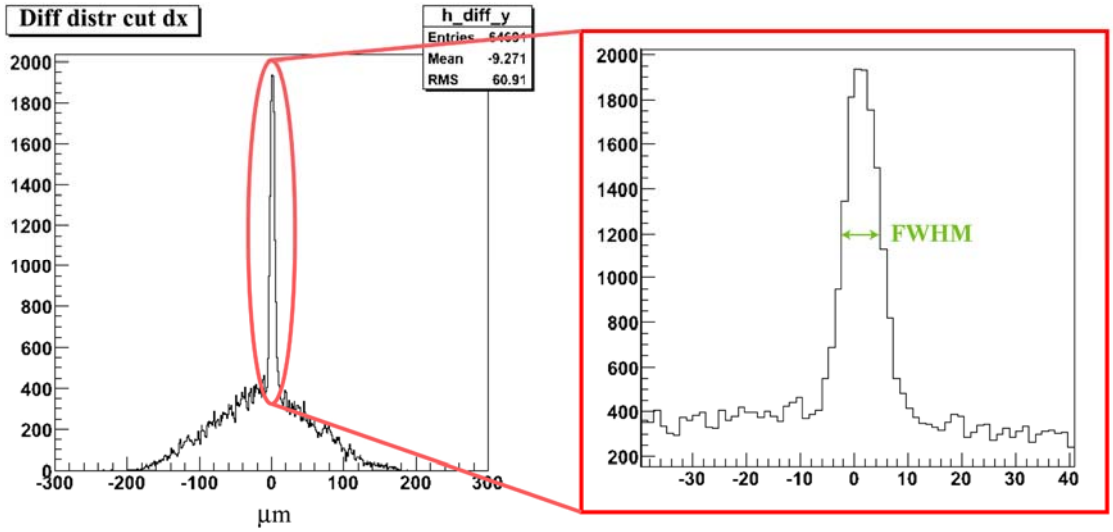

Fig. 8.29 Correlation peak from the differences of y coordinate with a cut in x-coordinate differences.

We noticed that the distortion is bigger in some regions compared to others. An estimate of the resolution in a low-distortion region has been obtained (fig. 8.30). The dispersion of the IEEM coordinates is σ = 2.3 µm; the FWHM = 2.35σ ~ 5 µm. This is an encouraging result as we have not yet faced the problem of vibrations and as we have still the residual degrading effect of the membrane.

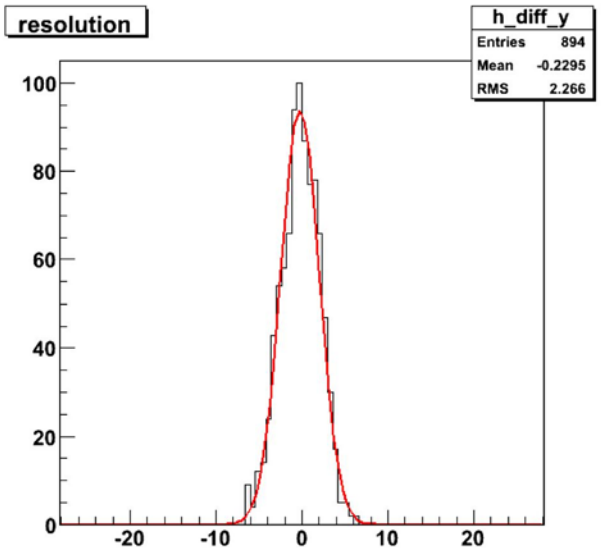

Fig. 8.30 Histogram of less distorted regions.

8.3.5 Linear sensor reconstruction efficiency

It is now possible to give an estimation reconstruction efficiency the NMOS sensor system; with this term we refer to the number of true ion events which are:

1. detected by the MCP of the IEEM and generate a light spot;
2. detected by the NMOS linear array sensor;
3. successfully reconstructed by the algorithm.

The final NMOS position detector has been chosen with the largest available pixel area in order to be very sensitive to faint light signals. As the calculation of the chapter 6 demonstrated, ion-induced luminous spot are expected to be strong enough to be detected by the sensor and the main contribution to the inefficiency of the final reconstruction comes from the analysis. One of the two sensors presents a sensibly higher noise level. The necessity to cut this noise forces us to set a high value on the amplitude threshold for incoming signals and the weakest ion-induced signals might be lost. Furthermore, the presence of more than one peak on the same frame may confuse the matching algorithm and preventing it from finding the correct associations. Unmatched peaks are discarded and more events are lost. We hence expect that the SDRAM detects some events that the

IEEM does not. On the other hand some fake ion impact indications are introduced by the IEEM system (MCP dark counts; wrong associations).

Both the SDRAM and the IEEM have some insensitive regions (marked in blue in fig. 8.26), where associations are impossible. For the estimation of the reconstruction efficiency, one must consider only those events that belong to the common active areas. The ion impact reconstruction efficiency of the sensor system is given by:

$$(8.6)\quad efficiency_{sensor} = \frac{events_{IEEM}}{events_{SDRAM}} \times \frac{1}{\varepsilon}$$

where ε is the fraction of ion impacts that are detected by the MCP.[2]

We assume, for the ions used (^{79}Br 214 MeV), the theoretical ion impact efficiency to be ε ~ 96% (fig. 7.17).[3] Requiring the euclidean distance[4] between $events_{IEEM}$ and $events_{SDRAM}$ to be less than 7μm, we estimate the ion impact reconstruction efficiency of the sensor to be 88%. The distance request of 7 μm was chosen as we are confident to include only correlated events.

The *global* reconstruction efficiency of the IEEM must take into account the geometrical inefficiencies due to the hole in the MCP and the shadow of the biasing wire (4% + 2%). The maximum efficiency we obtain is

$$(8.7)\quad efficiency_{global} = efficiency_{geometrical} \cdot efficiency_{sensor} \approx 80\% .$$

This expression is for optimal conditions when the image fills the field of view (no tilt or magnetic field problems) and in the hypothesis the MCP is correctly biased.

---

[2] To measure the sensor efficiency in reconstructing the positions of light spots we would normalize to the number of good PMT signals.

[3] In fig. 7.17 the Bromine energy was 241 MeV. The LET of Bromine in this energy range is almost constant and the expected yield Y, hence the IEEM efficiency, is practically the same.

[4] $dist^2 = (\Delta x)^2 + (\Delta y)^2$

8.4 Future plans

A lot of work remains to be done, as I mentioned repeatedly throughout this thesis. First of all a new MCP must be installed to replace the existing one that shows a degradation in performances due to wear after years of work. This will offer the occasion for a series of upgrades, such as the introduction of smaller apertures through the MCP to further reduce the residual effect (section 7.1.1). In this section we discuss other two important upgrades.

8.4.1 Target (membrane) upgrades

Self-standing metallic membranes (Au, Aluminum) are a quick way to ensure secondary electron emission from a DUT. On the negative side they bring significant degradations in lateral resolution as the angular deflection from scattering is projected over large distances that must be kept to avoid tearing the membrane. Another problem is the deformation of the reconstructed image for the induced distortions of the electrical field and the presence of a bulge due to the electrostatic pressure. We could deposit gold on the flat side of the membrane, but the bulge will remain unless we use smaller windows. Presently the membrane is mounted on top of the DUT. The membranes are without recognizable features and to focus the IEEM one must allow for precious space on the target for a copper grid. In addition there is no certainty that the lens settings found with the grid be the optimal ones for the gold.

Rather than mount the membranes directly on top of the DUT we are planning to mount them in a fixed position in front of the PEEM head. The PEEM lenses would then be adjusted once and for all. The window can be small (~ 0.5 mm), hence the amount of bulge (non planarity) will be smaller than what we have with the 5 mm wide windows we use now. In any case the deformations introduced would be measured with the aid of a SDRAM and the obtained information can be used to introduce the proper corrections once and for all. The drawback of this setup is that no optical alignment is possible. The solution is to place on the target, besides the DUT, a device that gives the exact coordinates of ion impacts and to measure carefully (before the experiment) the relative

distances between this object and the DUT. The SDRAM is an ideal tool for this task. At the beginning of the experiment, the alignment procedure is performed by sending the beam onto the memory array, until SEU are detected. During this process, no imaging task is required and the PEEM could be kept off. As the memory array gives only the position of the flipped cells but no information about their location in the FOV of the microscope (fig. 8.32), the SDRAM is exposed until a large number of SEU are induced and a recognizable pattern (the edge of one little sector, for instance) is reconstructed from the upset cells. If instead the IEEM were used to image the impacts, only few events would be sufficient to localize which part of the memory is exposed and its position in the FOV. Once known which part of the memory is being irradiated and the position in the FOV, the target is moved until the DUT is brought in front the PEEM head according to measures taken before the experiment.

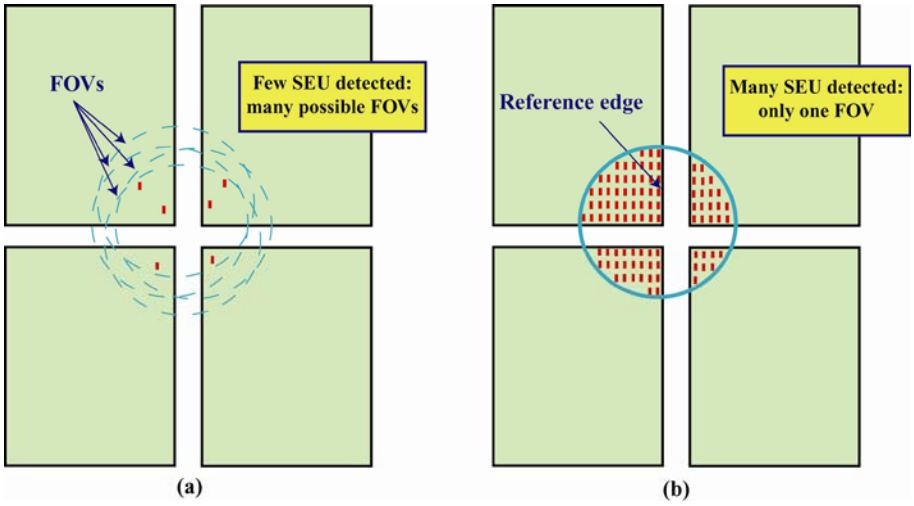

Fig. 8.31 **If no imaging is performed, few detected SEU events are not enough to ascertain where they are located in the FOV (a); this ambiguity can be solved by collecting a quantity of events sufficient to (almost) fill the FOV, so that a recognizable pattern is manifest (b).**

8.4.2 Electronic upgrade

A general upgrade planned for the spring 2008 is the introduction of a new DAQ system for the linear sensor. At present, the linear sensor reconstruction suffers from by a noisy channel. Our group is developing a 4-channel analog readout board showing

excellent performances both in noise and in speed. This board will replace the existing one and will exploit a more performing FPGA which, in the perspective of using the SDRAM-based SEU monitor for target alignment, will allow to integrate the SDRAM DAQ with the new IEEM one. The new DAQ system should greatly improve the noise performances of the readout electronic, offering the possibility to perform the experiment with lower threshold; this should increase the sensor efficiency.

As no equivalent (huge pixel) faster sensors are commercially available, the multiple-peak problem can be addressed only via software, improving the matching algorithm.

We will the use of PMT fast trigger to flag the NMOS signals; this will allow to cut MCP dark counts and noise pulses.

Other upgrades planned for 2008 involve the SDRAM DAQ. Two improvements should be added to the SDRAM DAQ to reduce the time to process incoming data. They address:

1. the capability to read only the logical address of the cells which are effectively irradiated. At the moment the whole memory is readout and compared to the COLD DUT and this is obviously a waste of time;
2. reduction of the download time for SEU, which is now very slow and is indeed a real “bottle neck”.

Conclusions

The SIRAD axial IEEM is now working. Preliminary measurements of efficiency and resolution are encouraging. Further tests are planned for 2008, after the necessary upgrades described in the last chapter. From these experiments we expect significant improvements on IEEM performances.

Since the inception of the axial IEEM project, the decision to take an original opto-electronic path and develop original sensors, rather than follow the footsteps of the SANDIA group, cost considerable R&D and effort, but it did pay back in terms of scientific and technical production.

Progress over the years has been slow, but this was due less to wrong turns and mistakes than to inadequate funding, particularly in the startup years. Significant progress was made once the axial IEEM project was finally funded in 2004 by the *Italian National Institute for Nuclear Physics (INFN).* The IEEM was installed in the axial configuration in the new irradiation chamber and the novel linear array sensor was commissioned late 2005. More recently we have been very severely plagued by a lack of significant beam time for effective development and debugging. The first successful images were obtained in the fall of 2006 after the installation of collimators to cure the halo effect; efficiency measurements and SEE tests were respectfully done in the spring and fall of 2007.

In retrospect we are comfortable in claiming that it is relatively straightforward to implement an axial IEEM at a pre-existing beam line. We believe that the IEEM resolution will be ~1μm, possibly better, certainly competitive and only slightly worse than that of the very best heavy ion microbeams.

It is important to keep in mind that the IEEM technique is not *perfectly* equivalent to traditional microprobes. The possibility to aim with micrometric precision at the target is a prerogative of microbeams and this is an extremely useful feature when one has a reason to test a very specific spot of the device under test. The IEEM instead furnishes

only the precise coordinates of random ion impacts in an area of hundreds of square microns. A systematic scan with a microbeam or the random IEEM technique are used when the user does not know “a priori” which spots of the device are more critical.

The traditional microbeam approach is arguably the preferred one, as one can decide where the next ion is going to strike, but it needs by far greater development. It is very challenging to focus to micron size a wide variety of energetic heavy ion beams. A competitive SEE heavy ion microbeam facility for modern microelectronic devices is invasive and requires great technical, human and economic resources to develop and implement. On the other hand an IEEM is relatively simple, not too expensive and compact; i.e. it can be easily installed and used by a relatively small group of people at high energy heavy ion accelerators, such as cyclotrons and post-accelerators that deliver ions with great range and are more suitable to test the latest microelectronic devices.

Bibliography

[1] S. M. Sze, Physics of Semiconductor Devices (Wiley, New York, 1981).

[2] E. L. Petersen, "Single Event Analysis and Prediction", 1997 IEEE NSREC Short Course, Snowmass, CO.

[3] J. Barak J. Levinson, M. Victoria, and W. Hajdas, "Direct processes in the energy deposition of protons in silicon," IEEE Trans. Nucl. Sci., vol. 43, no. 6, pp. 2820-2826, 1996.

[4] S. Duzelier, R. Ecoffet, D. Falguère, T. Nuns, L. Guibert, W. Hajdas, M. C. Calvet, "Low energy proton induced SEE in memories," IEEE Trans. Nucl. Sci., vol. 44, no. 6, pp. 2306-2310, 1997.

[5] G. R. Hopkinson, C. J. Dale, and P. W. Marshall, "Proton effects in charge-coupled devices," IEEE Trans.Nucl. Sci., vol. 43, no. 2, pp. 614-627, 1996.

[6] M. W. Savage, P. J. McNulty, D. R. Roth, and . C. Foster, "Possible role for secondary particles in proton-induced single event upsets of modern devices," IEEE Trans. Nucl. Sci., vol 45, no 6, pp. 2745-2751, 1998.

[7] C. M. Hsieh, P. C. Murley, and R. R. O'Brien, "A field-funneling effect on the collection of alpha-particle generated carriers in silicon devices," IEEE Electron Device Lett., vol. 2, no 4, pp 103-105, 1981.

[8] P. E. Dodd, "Device simulation of charge collection and single-event upset," IEEE Trans. Nucl. Sci., vol. 43, no. 2, pp. 561-575, 1996.

[9] H. Schöne, D. S. Walsh, F. W. Sexton, B. L. Doyle, P. E. Dodd, J. F. Aurand, R. S. Flores, N. Wing, "Time-resolved ion beam induced charge collection (TRIBICC) in microelectronics," IEEE Trans. Nucl. Sci., vol. 45, no. 6, pp. 2544-2549, 1998.

[10] P. E. Dodd and F. Sexton, "Critical charge concepts for CMOS SRAMs," IEEE Tran. Nucl. Sci., vol. 42, no. 6, pp. 1764-1771, 1995.

[11] J. R. Srour, C. J. Marshall, P. W. Marshall, "Review of displacement damage effects in silicon devices," IEEE Trans. Nucl. Sci., vol. 50, no. 3, 2003.

[12] D. Binder, E. C. Smith, and A. B. Holman, "Satellite anomalies from galactic cosmic rays," IEEE Trans. Nucl. Sci., vol. 22, pp. 2675–2680, Dec. 1975.

[13] T. C. May and M. H. Woods, "Alpha-particle-induced soft errors in dynamic memories," IEEE Trans. Electron. Devices, vol. 26, pp. 2–9, Feb. 1979.

[14] J. C. Pickel and J. T. Blandford, Jr., "Cosmic ray induced errors in MOS memory cells," IEEE Trans. Nucl. Sci., vol. 25, pp. 1166–1171, Dec. 1978

[15] R. C. Wyatt, P. J. McNulty, P. Toumbas, P. L. Rothwell, and R. C. Filz, "Soft errors induced by energetic protons," IEEE Trans. Nucl. Sci., vol. 26, pp. 4905–4910, Dec. 1979.

[16] C. S. Guenzer, E. A. Wolicki, and R. G. Allas, "Single event upset of dynamic RAM's by neutrons and protons," IEEE Trans. Nucl. Sci., vol. 26, pp. 5048–5053, Dec. 1979.

[17] J. L. Andrews, J. E. Schroeder, B. L. Gingerich, W. A. Kolasinski, R. Koga, and S. E. Diehl, "Single event error immune CMOS RAM," IEEE Trans. Nucl. Sci., vol. 29, pp. 2040–2043, Dec. 1982.

[18] A. E. Giddings, F.W. Hewlett, R. K. Treece, D. K. Nichols, L. S. Smith, and J. A. Zoutendyk, "Single event upset immune integrated circuits for Project Galileo," IEEE Trans. Nucl. Sci., vol. 32, pp. 4159–4163, Dec. 1985.

[19] F. Faccio, K. Kloukinas, A. Marchioro, T. Calin, J. Cosculluela, M. Nicolaidis, and R. Velazco, "Single event effects in static and dynamic registers in an a 0.25 μm CMOS technology," IEEE Trans. Nucl. Sci., vol. 46, pp. 1434–1439, Dec. 1999.

[20] M. P. Baze, S. P. Buchner, and D. McMorrow, "A digital CMOS design technique for SEU hardening," IEEE Trans. Nucl. Sci., vol. 47, pp. 2603–2608, Dec. 2000.

[21] A. W. Waskiewicz, J. W. Groninger, V. H. Strahan, and D. M. Long, "Burnout of power MOS transistors with heavy ions of Californium-252," IEEE Trans. Nucl. Sci., vol. 33, no. 6, pp. 1710-1713, 1986.

[22] J. L. Titus, C. F. Wheatley, K. M. Van Tyne, J. F. Krieg, D. I. Burton, and A. B. Campbell, "Effect of ion energy upon dielectric breakdown of the capacitor response in vertical power MOSFETs," IEEE Trans. Nucl. Sci., vol. 45, no. 6, pp. 2492-2499, 1998.

[23] J. L. Titus and C. F. Wheatley, "Experimental studies of single-event gate rupture and burnout in vertical power MOSFETs," IEEE Trans. Nucl. Sci., vol. 43, no. 2, pp. 533-545, 1996.

[24] T. C. May and M. H. Woods, "A new physical mechanism for soft errors in dynamic memories," Proc. IEEE Int. Reliability Phys. Symp., pp. 33-40, 1978.

[25] L. W. Massengill, "Cosmic and terrestrial single-event radiation effects in dynamic random access memories," IEEE Trans. Nucl. Sci., vol. 43, no. 2, pp. 576-593, 1996.

[26] T. V. Rajeevakumar, N. C. Liu, W. H. Henkels, W. Hwang, and R. Franch, "A new failure mode of radiation-induced soft errors in dynamic memories," IEEE Electron Dev. Lett., vol. 9, no. 12, pp. 644-646, 1988.

[27] C. L. Axness, H. T. Weaver, J. S. Fu, R. Koga, and W. A. Kolasinski, "Mechanisms leading to single event upset," IEEE Trans. Nucl. Sci., vol. 33, no. 6, pp. 1577-1580, 1986.

[28] H. T. Weaver, C. L. Axness, J. S. Fu, J. S. Binkley, and J. Mansfield, "RAM cell recovery mechanisms following high-energy ion strikes," IEEE Electron Device Lett., vol. 8, no. 1, pp. 7-9, 1987.

[29] J. R. Schwank, P. E. Dodd, M. R. Shaneyfelt, G.Vizkelethy, B. L. Draper, T. A. Hill, D. S. Walsh, G. L. Hash, B. L. Doyle, and F. D. McDaniel, "Charge collection in SOI capacitors and circuits and its effect on SEU hardness," IEEE Trans. Nucl. Sci., vol. 49, pp. 2937–2947, 2002.

[30] W. J. Shaptor, J. P. Meyers, J. B. Langworthy, E. L. Peterson, "Two parameter Bendel model calculations for predicting proton induced upset", IEEE Trans. Nucl. Sci., vol. 37, pp. 1966, 1990.

[31] J. L. Barth, "Modeling Space Radiation Environments," 1997 IEEE NSREC Short Course, Snowmass, CO.

[32] C. S. Dyer, "Space Radiation Environment Dosimetry," 1998 IEEE NSREC Short Course, Newport Beach, CA.

[33] J. L. Barth, "Modeling Space Radiation Environments," 1997 IEEE NSREC Short Course, Snowmass, CO.

[34] E. G. Stassinopoulos, G. J. Brucker, D. W. Nakamura, C. A. Stauffer, G. B. Gee, and J. L. Barth, "Solarflare proton evaluation at geostationary orbits for engineering applications," IEEE Trans. Nucl. Sci., vol.43, no. 2, pp. 369-382, 1996

[35] A. J. Tylka, W. F. Dietrich, and P. R. Boberg, "Probability distributions of high-energy solar-heavy-ion fluxes from IMP-8: 1973-1996," IEEE Trans. Nucl. Sci., vol. 44, no. 6, pp. 2140-2149, 1997.

[36] F. W. Sexton, "Measurement of single event phenomena in devices and ICs," 1992 IEEE NSREC Short Course, New Orleans, LA.

[37] J. Mazur, "The radiation environment outside and inside a spacecraft," 2002 IEEE NSREC Short Course, Phoenix, Arizona.

[38] C. H. Tsao, R. Silberberg, and J. R. Letaw, "Cosmic Ray Heavy Ions At and Above 40,000 Feet," IEEE Trans. on Nucl. Science, Vol. 31, No. 6, pp. 1066-1068, December 1984.

[39] R. Silberberg, C. H. Tsao, J. R. Letaw, "Neutron Generated Single Event Upsets," IEEE Trans. on Nucl. Science, Vol. 31, No. 6, pp. 1183-1185, December 1984.

[40] A. H. Tabor and E. Normand, "Single Upset in Avionics," IEEE Trans. on Nucl. Science, Vol. 40, p 120, December 1993.

[41] J. L. Barth, C. S. Dyer, E. G. Stassinopoulos, "Space, Atmospheric, and terrestrial radiation environments", IEEE Trans. Nucl. Sci., vol. 50, no. 3, pp. 466−482, 2003.

[42] J. F. Dicello, M. Wasiolek, M. Zaider, "Measured microdosimetric spectra of energetic ion beams of Fe, Ar, Ne, and C: limitations of LET distributions and quality factors in space research and radiation effects", IEEE Trans. Nucl. Sci., vol. 38, no. 1, pp. 1203-1209, 1991.

[43] J. F. Ziegler, "Terrestrial cosmic rays," IBM J. Res. Development, vol.40, no. 1, pp. 19–39, Jan. 1996.

[44] J. C. Pickel and T. J. Blandford Jr., "Cosmic ray induced errors in MOS memory cells", IEEE Trans. Nucl. Sci., vol. NS−25, pp. 1166, 1978.

[45] E. L. Petersen, J. B. Langworthy and S. E. Diehl, "Suggested single event upset figure of merit", IEEE Trans. Nucl. Sci., vol. NS−30, pp. 4533, 1983.

[46] W. L. Bendel, E. L. Petersen, "Proton upset in orbit", IEEE Trans. Nucl. Sci., vol. NS−30, pp. 4481, 1983.

[47] W. J. Stapor, J. P. Meyers, J. B. Langworthy, and E. L. Petersen, "Two parameter bendel model calculations for predicting proton induced upset," IEEE Trans. Nucl. Sci., vol. NS-37, p. 1966, 1990.

[48] Y. Shimano, T. Goka, S. Kuboyama, K. Kawachi, T. Kanai, and Y. Takami, "The measurement and prediction of proton upset," ZEEE Trans. Nucl. Sei., vol. 36, p. 2344, 1989.

[49] E. Noah, T. Bauer, D. Bisello, F. Faccio, M. Friedl, J.R. Fulcher, G. Hall, M. Huhtinen, A. Kaminsky, M. pernicka, M. Raymond, J. Wyss, "Single event upset studies on the CMP tracker APV25 readout chip", Nucl. Instr. Meth. A, 492 (2002) 434.

[50] P. E. Dodd, M. R. Shaneyfelt, K. M. Horn, D. S. Walsh, G. L. Hash, T. A. Hill, B. L. Draper, J. R. Schwank, F. W. Sexton, and P. S. Winokur, "SEU−sensitive volumes in

bulk and SOI SRAM's from first−principles calculations and experiments", IEEE Trans. Nucl. Sci., vol. 48, pp.1893–1903, 2001.

[51] B.E. Fischer, "The scanning heavy ion microscope at GSI", Nucl. Intrum. Methods Phys. Res. B 10-11, (1985) 693.

[52] G. Dollinger, G. Datzmann, A. Hauptner, R. Hertenberger, H. Körner, P. Reichart and B. Volckaerts, "The Munich ion microprobe: Characteristics and prospect", Nucl. Instrum. Meth. B, 210 (2003) 6.

[53] S. Kurashima, N. Miyawaki, S. Okumura, M. Oikawa, K. Yoshida, T. Kamiya, M. Fukuda, T. Satoh, T. Nara, T. Agematsu, I. Ishibori, W. Yokota and Y. Nakamura, "Improvement in beam quality of the JAEA AVF cyclotron for focusing heavy-ion beams with energies of hundreds of MeV", Nucl. Instrum. Meth. B 260 (2007) 65.

[54] F. Watt, J. A. van Kan, I. Rajta, A. A. Bettiol, T. F. Choo, M. B. H. Breese, T.Osipowicz, "The National University of Singapore high energy ion nano-probe facility: Performance tests", Nucl. Instr. and Meths. B, vol. 210, pp. 14−20, 2003.

[55] G. Datzmann, G. Dollinger, C. Goeden, A. Hauptner, H. J. Korner, P. Reichart, O. Schmelmer, "The Munich Microprobe SNAKE: First results using 20 MeV protons and 90 MeV sulfur ions", Nucl. Instr. And Meth. B, vol. 181, pp. 20−26, 2001.

[56] B. L. Doyle, G. Vizkelethy, D. S. Walsh, B. Senftinger and M. Mellon., "A new approach to nuclear microscopy: the ion–electron emission microscope" Nucl. Instr. Meth. B 158 (1999) 6.

[57] 350 PEEM from Staib Instrumente GmgH Lagenbach, Germany.

[58] E. J. Sternglass, "Theory of Secondary Electron Emission by High-Speed Ions", Phys. Rev. 108 (1957) 1.

[59] J. E. Borovsky, D. M. Suszcynsky, "Experimental investigation of the z^2 scaling law of fast-ion-produced secondary-electron emission", Phys. Rev. A, vol. 43, pp. 1416−1432, 1991.

[60] J. Schou, Scanning Microscopy 2 (1988) 607.

[61] D. Hasselkamp, K.G. Lang, A. Scharmann, N. Stiller, "Ion induced electron emission from metal surfaces" Nucl. Instr. Meth. 180 (1981) 349.

[62] Griffith and Engel, Ultramicroscopy 36, 1 (1991).

[63] Quantar technology Inc., Santa Cruz, Calif.

[64] D. Bisello, A. Kaminsky, A. Magalini, M. Nigro, D. Pantano, S. Sedykh and J. Wyss, "Ion electron emission microscopy at the SIRAD single event effect facility", Nucl. Inst. Meth. B, 181 (2001) 254.

[65] J. Wyss, D. Bisello and D. Pantano, "SIRAD: an irradiation facility at the LNL Tandem accelerator for radiation damage studies on semiconductor detectors and electronic devices and systems" Nucl. Instr. Meth. A 462 (2001) 426.

[66] BURLE instruments QS 11983-2: APD 3040PS 12/10/8 I 60:1 6.4CH P47 two stacks, 40 mm diameter with 8 mm central hole diameter MCP coupled to a P47 phosphor layer.

[67] Physik Instrumente (PI) Gmbh & Co. KG, Auf der Romerstrasse 1, D-76228 Karlsruhe/Palmbach Germany; www.physikinstrumente.de. M-126 Series (linear positioning stages), M-0.42 (Tip/Tilt stages).

[68] SiTek 2L20SP UV-enhanced PSD; www.sitek.se.

[69] D. Bisello, A. Candelori, P. Giubilato, A. Kaminsky, S. Mattiazzo, M. Nigro, D. Pantano, R. Rando, M. Tessaro and J. Wyss, "Position sensitive detectors for Ion Electron Emission Microscopy", Nucl. Instr. Meth.

[70] D. Bisello, M. Dal Maschio, P. Giubilato, A. Kaminsky, M. Nigro, D. Pantano, R. Rando, M. Tessaro and J. Wyss, "A novel sensor for ion electron emission microscopy", Nucl. Instr. Meth. B, 219 (2004) 1000.

[71] "The novel Ion Electron Emission Microscope at SIRAD", Piero Giubilato's PhD Thesis.

[72] PROXITRONIC BV25-82BY-V, 25 mm diameter Image Intensifier with quartz input window, Bialkali photocathode, v-stack MCP, P47 phosphor layer and output fiber optic plate.

[73] Hamamatsu S3901/3904 NMOS linear image sensor.

[74] Silson Ltd, Northampton, England, www.silson.com.

[75] B.E. Fischer, M. Cholewa, H.Noguchi, "Some experiences on the way to biological single ion experiments", NIM B181 (2001) 60-65.

[76] SRIM (Stopping and Range of Ions in Matter) and TRIM by James Ziegler. www.srim.org.

[77] GEANT4: a toolkit for the simulation of the passage of particles through matter, http://geant4.web.cern.ch/geant4/

[78] D. Bisello, A. Candelori, P. Giubilato, A. Kaminsky, S. Mattiazzo, M. Nigro, D. Pantano, R. Rando, L. Silvestrin, M. Tessaro and J. Wyss, "Secondary electron yield of Au and Al2O3 surfaces from swift heavy ion impact in the 2.5–7.9 MeV/amu energy range" Nucl. Instr. Meth. B, 266 (2008) 173.

[79] A. Itoh, T. Majima, F. Obata, Y. Hamamoto and A. Yogo, "Secondary electron emission from Au by medium energy atomic and molecular ions", Nucl. Instr. Meth. B 193 (2002) 626.

[80] Amptek MCA8000A Multichannel Analyzer.

[81] S. Bertazzoni, D. Di Giovenale, L. Mongiardo, M. Salmeri, A. Mencattini, A. Salsano, D. Bisello, A. Candelori, P. Giubilato, A. Kaminski, M. Nigro, R. Rando, J. Wyss, S. Lora, "TID and SEE characterization and damaging analysis of 256 Mbit COTS SDRAM for IEEM application"

[82] S. Bertazzoni, G. C. Cardarilli, G. C. Grande, D. Piergentili, M. Salmeri, S. Sperandei, S. Bartalucci, G. Mazenga, M. Ricci, V. Bidoli, D. De Francesco, E. Reali, and A. Rovelli, "Tests of 64 Mb SDRAM for space applications," in European Conference on Circuit Theory and Design, Stresa, Italy, August 1999.

[83] S. Bertazzoni, , G. C. Cardarilli, D. Di Giovenale, G. C. Grande, P. Marinucci, D. Piergentili, M. Salmeri, A. Salsano, S. Sperandei, S. Bartalucci, G. Mazenga, M. Ricci, V. Bidoli, D. De Francesco, P. G. Picozza, and A. Rovelli, "Failure tests on 64 Mb SDRAM in radiation environments," in IEEE International Symposium on Defect and Fault Tolerance in VLSI Systems, Albuquerque, New Mexico, USA, November 1999.

Index